2013

# Large Eddy Simulation and Analysis of Shear Flows in Complex Geometries

Prasad Mohanrao Kalghatgi
*Louisiana State University and Agricultural and Mechanical College*

# LARGE EDDY SIMULATION AND ANALYSIS OF SHEAR FLOWS IN COMPLEX GEOMETRIES

A Dissertation

Submitted to the Graduate Faculty of the
Louisiana State University and
Agricultural and Mechanical College
in partial fulfillment of the
requirements for the degree of
Doctor of Philosophy

in

The Department of Mechanical Engineering

by
Prasad M. Kalghatgi
Bachelor of Engineering, Visvesvaraiah Technological University, 2003
December 2013

# Acknowledgments

First and foremost I would like to thank Professor Sumanta Acharya for providing me with the opportunity and financial support to pursue higher education and valuable guidance throughout this tenure. He has been very patient throughout the course of this work. His critical remarks have helped in a meaningful completion of this work.

I would also like to thank Professor Harris Wong, Dr. Ingmar Schoegl and Dr. Robert Hynes for serving on my committee. I specially thank Professor Wong for his remarkable teachings of theory of hydrodynamic stability. I would like to extend my gratitude to Professor Paul Strykowski (University of Minnesota) for his insightful technical discussions, which was of significant help in my work on countercurrent shear flows.

None of this would have been possible without the support of my parents (Meera and Mohanrao Kalghatgi), my aunt (Vijaya Deshpande) and my late uncle (Ajay Deshpande). They always believed in me and encouraged me in all my endeavors. They always led me on the path of righteousness and I hope to become a better person with their blessings. Dedicating this dissertation to them is a small way of saying thank you!

I am very thankful to my cousin Raghavendra Jorapur and uncle Krishnarao Deshpande for their invaluable guidance in making career choices that put me on this path of pursuing higher education. I am also thankful to my undergraduate friends group always-thinking and their families who have made me believe in the best in people.

My former and current lab-mates and friends at LSU have always been a wonderful company. I would like to thank each one of them for being part of my journey at LSU. I would especially like to thank Pranjali for being supportive and encouraging.

# Table of Contents

# List of Tables

# List of Figures

# Abstract

In the present work, large eddy simulation is used to numerically investigate two types of shear flows in complex geometries, ($i$) a novel momentum driven countercurrent shear flow in dump geometry and ($ii$) a film cooling flow (inclined jet in crossflow). Verification of subgrid scale model is done through comparisons with measurements for a turbulent flow over back step, present cases of counter current shear and film cooling flow. In the first part, a three dimensional stability analysis is conducted for countercurrent shear flow using Dynamic mode decomposition and spectral analysis. Kelvin-Helmholtz is identified as primary instability mechanism and observed as global mode at a specific parameter. Mechanism of global mode synchronization over distinct spatial location is studied.

In the second part, the flow physics of film cooling flows is analysed. The origin, evolution of various coherent flow structures and their role in film cooling heat transfer is studied based on detailed flow visualization. Further, the contribution of coherent structures in film cooling heat transfer and mixing is studied through modal analysis. Low frequency modes are found to have large contribution in cooling surface adiabatic temperature fluctuation while high frequency modes play larger role in bulk mixing. Finally, a new contoured crater shape is developed and shown to have improved performance at shallow depth compared to earlier designs.

# Chapter 1
# Introduction

## 1.1 Motivation

Turbulent shear flows played a major role in technological developments over last century. Shear layers in a variety of forms (jets, wakes, mixing layers) find application in rocket, aircraft, ship and turbo-machinery technology, such as bluff body flame/swirl stabilized combustors; co-flowing parallel jets and jets in crossflow for air-fuel mixing in gas turbines and rocket engines; inclined jets in crossflow for gas turbine blade cooling; jet formation, noise control and thrust vectoring in aircraft and rocket propulsion. Over all turbulent shear layers are at the center of transportation, aviation and power generation. Performance improvement of such fluid systems is typically achieved by improvisation/controlling the mixing/stability characteristics of shear layer typically through fluidic control and/or geometric design changes. Efficiency and reliability of fluid systems such as land based and aviation turbine engines has serious economic, environmental implications and therefore understanding characteristics of new and existing turbulent shear layers are of importance.

The present study focuses on two kinds of shear flow configuration, ($i$) A novel configuration of counter-current shear layer - with intended application for high performance combustion and fuel-air premixers and ($ii$)An inclined jet in crossflow applied to film cooling of turbine blades. Both applications complement each other in the framework of gas turbine engine performance improvement.

In the work done by Strykowski and Wilcoxon (1993), the advantage of applying counter-

current shear to main stream flow (jets), was realized in terms of higher turbulence levels, large scale coherent structures and controllability. These features can potentially be used for developing compact and high power combustors. A momentum driven counter-current shear flow would has an advantage of mitigating difficulties of a suction based technique described in aforementioned study. Therefore, in the first part of this study, characteristics of a novel momentum driven counter-current shear layer in a dump geometry are numerically investigated.

In the second part of this study, a shear layer flow formed by inclined jet in crossflow for film cooling applications is numerically investigated. Film cooling flows constitute an important means to achieve higher thermodynamic efficiency of gas turbine engines, by allowing higher turbine inlet temperatures. Although studied extensively, there are few previous studies that shed light on both qualitative and quantitative nature of thermal and flow field at Reynolds numbers comparable to engine conditions. A specific film cooling flow configuration is numerically investigated using large eddy simulation. Further a simple and robust geometric modification to the film cooling hole geometry is shown to perform over previous attempts.

## 1.2 Background

Shear flows are ubiquitous in nature and routinely found in blood flow in vascular systems, rivers, atmospheric and oceanic flows, planetary and galactic flows. Figure 1.1 shows some natural occurrences of shear layers. Figure 1.1a shows the roll-up of Kelvin Helmholtz structures in the shear layer formed by cloud layers at different velocities. Jupiter is well known for layered atmospheric bands that flow in opposite direction forming gigantic shear layers. Figure 1.1b shows the great red spot (quasi-stationary vortex) hosted in one of the shear layers in Jupiter's atmosphere is larger than the size of earth. The shear layers are also observed in the galactic flows. Figure 1.1c shows M-51 slip streams believed to be formed due to differential velocities of rotation of inner and outer galactic bands.

(a) Kelvin Helmholtz Instability - Visualized by clouds

(b) Shear bands in Jupiter's Atmosphere

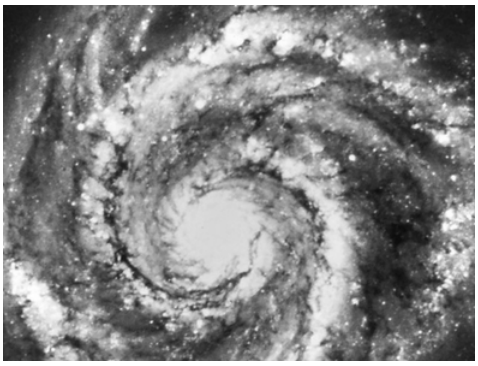

(c) Shear layer in galactic bands

Figure 1.1: Shear layers in nature

Engineered fluid systems typically contains mixing of fluid streams at differential velocities, separated flows in complex geometries giving rise to shear layers. Shear layers are typically formed due to jets exiting in quiescent surroundings 1.2a, wakes behind bluff bodies 1.2b and mixing of two jet streams at differential velocities 1.2c. A generic shear layer can have gradients of physical properties such as temperature, density, viscosity, chemical composition besides the velocity gradient. The thickness of the shear layer $\delta$ based on velocity is the distance normal to the shearing direction where the velocities reach $0.995U_i$ where the $U_i$ is the respective jet velocity. The shear layers are classified as thin shear layers if $\delta \gg L$ where $L$ is the length of shear layer development.

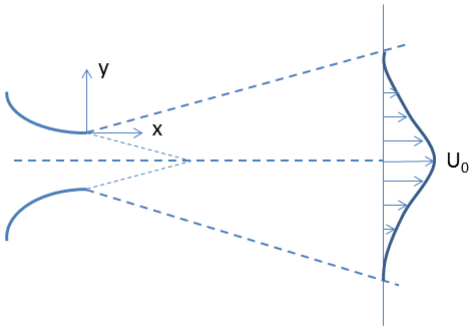


(a) Shear layer due to jets

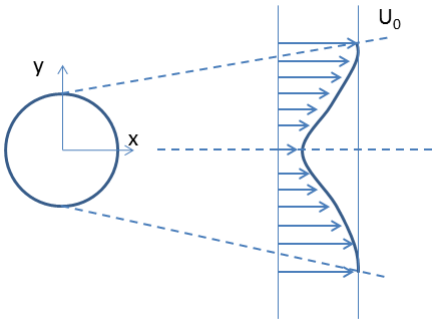


(b) Shear layer due to wakes

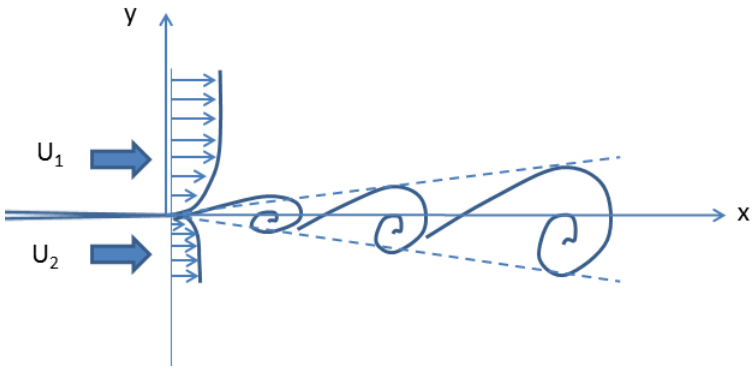


(c) Co-flowing shear layer

Figure 1.2: Shear layers

Two parameters $(i)$ velocity ratio $r = \frac{U_2}{U_1}$ and $(ii)$ Normalized velocity ratio $\lambda = \frac{U_1 - U_2}{U_1 + U_2}$ describe the shear flows. $U_1$ and $U2$ are the velocities of the two streams forming the shear layer. The convective velocity for the shear layer is defined as $U_c = \frac{U_1 + U_2}{2}$and the magnitude of total shear is given as $\Delta = U_1 - U_2$. Therefore, normalized velocity ratio physically means the relative magnitude of total shear with respect to convective velocity. Vorticity thickness is another parameter used to quantify the shear layer thickness $\delta_w = \frac{U_1 - U_2}{\left(\frac{\partial u}{\partial y}\right)_{max}}$. When $U_1 > 0$ and $U_2 > 0$ the resulting shear layer is called co-flowing shear layer. When $U_1 > 0$ and $U_2 < 0$ the resulting shear layer is called counter flowing shear layers, shown in Figure 1.3

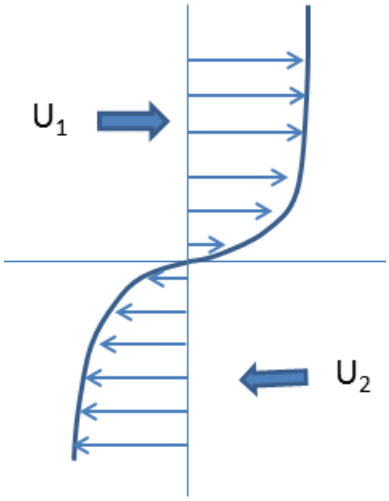


Figure 1.3: Counter current shear layer

### 1.2.1 Historical perspective - shear layers

Although equation of fluid motions were formulated in early $19^{th}$ century between 1823 to 1845 and the work on hydrodynamic stability of inviscid fluid layers at differential velocities was done as early as Helmholtz 1868 and Kelvin 1871, from a historical perspective, the theoretical developments in viscous shear layers took place after the development of boundary layer theory. The formal boundary layer theory was first proposed by Prandtl in 1904. It took a failed diffuser design to get Prandtl's attention to the phenomenon of flow separation at certain condition. His observation of vorticity induced by the solid boundary in a small region is ejected in the bulk flow under certain conditions, was the first explanation of separating boundary layer and shear layer formation due to separated flow. A number of studies were conducted through 1940s and 1950s by Liepmann's research group. The specifically noted is (Liepmann and Laufer, 1947), which provided first detailed study of turbulent free shear layers that showed the self-similar nature of shear layers. Their study was based on flow velocity measurements using thermal anemometry and concluded that the mixing length theory (Prandtl, 1928) was inadequate for free shear layers. Bradshaw (1966) showed that initial conditions have a profound effect on the development of shear layers and potentially be influenced to loss of self-similarity and exhibit a variety of characteristics. The understanding

of turbulence in shear layer took a leap with experimental observations of Brown and Roshko (1974) and Winant and Browand (1974). They observed large scale coherent structures in shear layers that was not of stochastic nature. The dynamics and various stages of evolution of these coherent structures was elucidated by Winant and Browand (1974). The conclusion of their study was that, the nature of turbulence in shear layers is not purely of stochastic nature. This was in support of structural approach in turbulence that began with Tollmien in 1930s, Tollmien-Schlichting waves arising in instability of boundary layer over flat plate. Corrsin (1943) and Townsend (1947) had observed periodically turbulent outer regions shear layers; characteristic signatures of large scale coherent structures.Townsend also developed double structure description of turbulent flows containing large eddies and small scale turbulence and large scale structures dominated the development of shear layer. This work may be regarded as the transition from purely stochastic treatment of turbulence towards deterministic approach began with Poincaré in 1899 and developed by Ruelle and Takens (1971). Ruelle and Takens (1971) discussed the evolution of flow field from orderly steady state to turbulence through a set of bifurcations as Reynolds number is increased. They also hypothesized that the description of fluid flow can be explained by a finite dimensional deterministic system of ordinary equation. However, this approach is highly conditional and so far few studies concerning application of strange attractors to describe shear flows (Bradstater and Swinney, 1987; Xie et al., 2003).

### 1.2.2 Stability of shear layers

Linear stability analysis through normal modes shows that the inviscid parallel flow subjected to external perturbation is always unstable and the two dimensional vortices evolve exponentially via Kelvin-Helmholtz instability mechanism. Before proceeding further it is important to note that the above mentioned formulation is symmetric to the Galilean transformation. The convective and absolute instability can be defined only by breaking Galilean symmetry with respect to a uniform translation of coordinate system. With this condition

the stationary frame of reference can be uniquely defined typically to that of laboratory frame of reference. This is generally achieved by the no-slip condition on the wall / splitter plate that is stationary with respect to laboratory. The spatial development of the shear layer then can be defined with respect to a stationary point such as a tip of the splitter plate in a fixed reference frame.

The co-flowing shear layers have been investigated by many researchers (Brown and Roshko, 1974; Winant and Browand, 1974; Jimenez, 1983; Lasheras and Choi, 1988). In a typical spatial development of planar co-flowing shear layers the two dimensional spanwise structure are evolved (Kelvin-Helmholtz instability) followed by the transition to three dimensional instability and development of spanwise structures (elliptic instability). The spatial development of shear layer is divided in three regions, (i) initial development  development of spanwise 2D vortices, (ii) transition region  transition to 3D flow and development of streamwise vortices, (iii) fully developed region - the shear layer is said to be fully developed when profile of mean and RMS quantities collapse upon normalized by relevant local variables. The initial development of such shear layers is observed to be sensitive to low level external perturbations and susceptible for early transition but the fully developed shear layer is not sensitive to the external perturbation. A temporally developing shear layers can be thought of as spatially periodic shear layers where the Galilean transformation is symmetric with respect to translation and a unique frame of reference may not be defined. K-H instability uniform initial condition with periodic boundaries is one such example. Such flows are of academic interest and seldom seen in practical application. It is appropriate to discuss the stability of the spatially developing shear layers in the context of absolute and convective instability. Ho and Huerre (1984); Huerre and Monkewitz (1990) provide in-depth review of the stability aspects spatially developing flows. Understanding the stability of such flows is vital for the development of an engineering application. Few spatially developing shear layer like co-flowing parallel shear flows as discussed before, are very sensitive to the external perturbations. The spatial movements of vortical structures created in the shear layers due

to fundamental instability can be seen as spatially growing instability waves of various frequencies. The concept of local and global, absolute and convective instability for such flows can be distinguished. Instability if the local velocity profile is termed as local instability and the instability of velocity profile of entire flow field is referred as global. In the same context if the perturbation locally introduced at a spatial location in the flow field grows as it is convected away and the perturbations at corresponding location die down, the flow is considered to be convectively unstable. If the perturbations die down everywhere then the flow is convectively stable. Convectively unstable flows are referred as noise amplifiers. In contrast to this nature if the locally introduced perturbation spreads in upstream and downstream direction then the instability of the local velocity profile is termed as locally absolutely unstable. Absolutely unstable flows behaves as oscillators and insensitive to the low level external perturbation. In Figure 4 the schematic of impulse responses are shown. The flow stability of flow with a locally introduced perturbation is indicated as, (a) stable, (b) convectively unstable, (c) absolutely unstable, (d) stable, (e) absolutely unstable, (f) stable, (g) convectively unstable and (h) absolutely unstable.

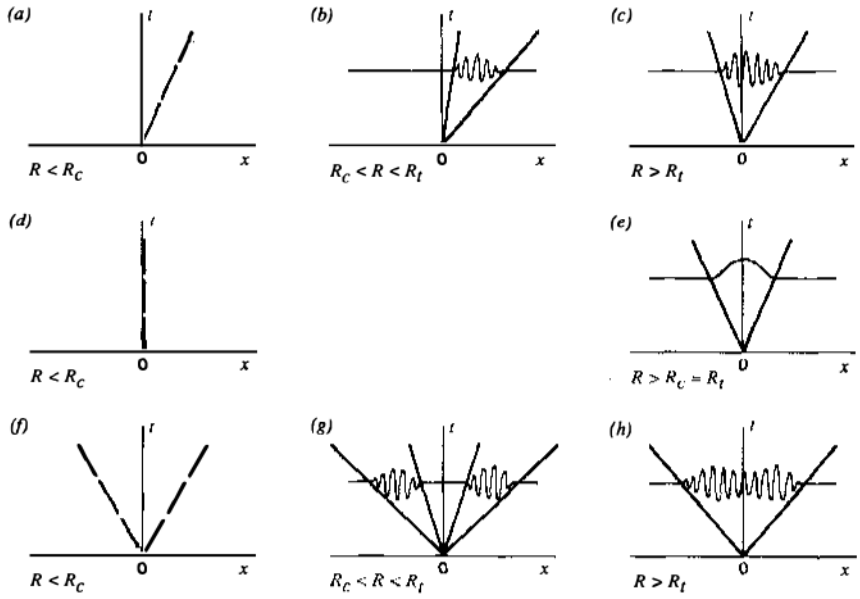


Figure 1.4: Schematic of impulse response Huerre and Monkewitz (1990)

For the realization of absolutely unstable flows a feedback mechanism is essential for upstream spreading of perturbations. This condition is achieved with a pressure feedback as created by placing the rigid body in the flow field. Periodic shedding of Karman vortices in flow over cylinder is one celebrated example. The self-sustaining oscillator behavior can also be achieved purely hydrodynamically when there is sufficient region of reverse flow. Separation bubbles over flat surfaces or airfoil, countercurrent shear layers and low/high density jets are examples of such flows. Countercurrent shear flows and separation bubbles under appropriate conditions can sustain self-sustained oscillating behavior (Strykowski and Niccum, 1991; Hammond and Redekopp, 1998). The self-excited oscillations in heated round jets were studied by Monkewitz et al. (1990). In the following section we will have more discussion on countercurrent shear layers followed by their application overview.

### 1.2.3 Counter-current shear layers

Counterflowing shear layers are quite commonly encountered in many engineering applications such as cavity flows, separated boundary layers. However, only a few studies on countercurrent shear layers have been reported in literature compared to co-flowing shear layers. Notable contributions towards flow physics of counter current shear flows are (Humphrey and Li, 1981; Huerre and Monkewitz, 1985; Strykowski and Niccum, 1991; Khemakhem, 1997; Xie et al., 2003; Forliti et al., 2005). Humphrey and Li (1981) studied a countershear configuration where two symmetrical channel streams were separated by a thin wall and interaction was allowed only over a short streamwise length by providing a gap in the wall. The two interacting streams formed a stagnation point upon which both the streams bifurcated and a part of each stream turned around and entered the opposite stream. A key observation of this experiment was the periodic shedding of vortices, pairing and onset of three dimensionality over a short streamwise distance. Intense mixing of main and bifurcated stream was observed in the recirculation bubble while the flow remained streamlined in rest of the domain. The spatio-temporal stability similar planar parallel countercurrent shear flows was

explored by Huerre and Monkewitz (1985). They reported a transition in shear layer from convective to absolute instability beyond $\lambda = (U_1 - U_2)/(U_1 + U_2) = 1.315$, where $U_1$ and $U_2$ are velocities of primary and secondary fluid streams. The limit $\lambda = 1.315$ constitutes a secondary stream velocity magnitude greater than 13% of primary stream. These results were experimentally verified for axisyemtric parallel counter-current shear flows Strykowski and Niccum (1991, 1992) and for planar countercurrent shear flow (Forliti et al., 2005).

Strykowski and Niccum (1991) investigated the dynamical behavior of countercurrent axisymmetric streams of identical fluids at isothermal conditions. The counter flowing axisymmetric stream was created by applying suction over a annular region surrounding the central jet discharging from a axisymmetric nozzle. A critical velocity ratio $\lambda = 1.32$ was observed beyond which shear layer exhibits the organized axisymmetric coherent structures at a discrete frequency - an indication of global instability mode. The inference was based on $(i)$ spectral records of velocity signal - discrete frequency, $(ii)$ response to low level forcing - insensitivity to low level external perturbation and $(iii)$ verifying if saturated turbulent intensity can be modeled with Landau equation - indication of a Hopf bifurcation. Dynamic characteristics of a similar flow configuration were investigated by Xie et al. (2003). They reported various stages of spatial evolution of axisymetric and helical flow structures along with sequence of bifurcation 2-torus - limit cycle - subharmonic bifurcation and ultimately to chaos. Khemakhem (1997); Forliti et al. (2005) investigated a planar counter-current shear layer without the formation of global stagnation point in the flow field. The counter flowing stream was formed by applying suction below the splitter plate separating primary and secondary stream. A spatially developing parallel counter-current shear layer was formed off the tip of splitter plate. Consitent with therotical predictions of Huerre and Monkewitz (1985) the critical parameter $\lambda = 1.31$ was found beyond which onset of absolute instability was witnessed. These conclusions were based on a transition in self-similar turbuent velocity profile below critical $\lambda$ when appropriate scaling was used.

A general classification of countercurrent shear layers based on existence of global stagna-

tion point emerges through aforementioned studies. While parallel shear layer approximation holds for counter-current shear layers without formation of global stagnation, counter-current shear layers with stagnation exhibit a lagre recirculation, invalidating parallel shear layer assumptions. Theoretical background of stability analysis of such flows is established in (Hammond and Redekopp, 1998) where, they analysed linear stability of number of Falkner-Skan type velocity profiles with reversed flow, typical to the laminar separation bubbles. Onset of global dynamics was reported when the reversed flow exceeds 30% of primary stream velocity. Before proceeding with account of experimental verification of Hammond and Redekopp theory applied to separation bubbles in counter-current shear layers, it is necessary to discuss the genesis of specific counter-current configurations based on intended practical applications.

Controllable flow dynamics, turbulence and compact mixing region of counter-current shear layers are ideally suitable for combustion and mixing applications. A number of studies devoted to develop a counter-current flow configuration for compact and high power combustors were reported by Strykowski and Wilcoxon (1993); Strykowski and Forliti (2000); Forliti and Strykowski (2005). Central to these applications was the idea of using a smaller counter flowing stream to fluidically control the dynamic characterisitcs of the primary stream. Mixing enhancement in axisymmetric counter-current shear flows with annular counterflow was studied by Strykowski and Wilcoxon (1993) in a similar setup used by Strykowski and Niccum (1991). An additional annular collar was used to minimize the reversed flow. Significant mixing enhancements were achieved through global excitation of the central jet. Similar configuration was used at supersonic Mach numbers by Strykowski et al. (1993). Strykowski and Forliti (2000); Forliti and Strykowski (2005); Anderson and Strykowski (2009) applied concept of counter flowing control jet to planar dump combustors. Strykowski and Forliti (2000) developed a planar counter-current flow configuration by applying the suction below the step of the dump combustor. They reported increase in over all and spanwise turbulence along with increase in length scales - a particularly desired characteristics to avoid thermo-

acoustic instabilities and strain induced quenching. A slightly different setup where suction was applied to a narrow strip below the splitter plate at the dump plane was experimented by Forliti and Strykowski (2005). Application of counter-current velocities upto 10% of primary stream did not result in transition phenomenon. However, compact recirculation with enhanced turbulence was observed behind the dump plane. Key characteristics like increased three-dimensionality and disrupted spanwise coherence were observed and quantified. All of the applications mentioned, were based on experiments by Strykowski and Niccum (1991) and supported by theory provided by Huerre and Monkewitz (1985).

A distinct configuration of momentum driven counter-current shear flow was devised by Anderson and Strykowski (2009) primarily, to avoid the challenges of applying suction in combusting environments. In their experimental setup a counter flowing jet assembly was placed down stream of the dump plane and secondary jet was discharged to establish counter-current flow. Interaction of primary and secondary jet formed a global stagnation point upon which a branch of secondary jet bifurcated and turned into the primary jet forming a recirculation bubble. Increase in recirculation bubble size and turbulence levels increased with higher secondary jet velocity was observed. In the further investigations Anderson and Strykowski (2009) analysed the flow based on characteristics of velocity spectra and sensitivity to low level external forcing. Based theoretical findings of Hammond and Redekopp (1998) and insensitivity of the flow field to external perturbations beyond 14% flow rate of primary stream, they concluded onset of global dynamics. However, the detailed mechanistic analysis of the coherent flow structures was not done experimentally. The present work includes numerical study instability mechanisms in an identical flow and geometrical configuration complementing the experimental findings in Anderson (2011).

### 1.3 Film cooling flows

In this section a brief introduction is provided for a shear flow formed due to interaction of a jet in crossflow applied to film cooling of gas turbine blades, well known as film cooling

jets Goldstein (1971). Before divulging the details, it is appropriate to briefly discuss the motivation of film cooling flows.

The limit on thermodynamic efficiency of gas turbine engines operating on Brayton cycle is set by the turbine inlet temperature. Solely due to this reason modern gas turbine engines operate at a higher turbine inlet temperature to achieve higher thermodynamic efficiency. The maximum temperature levels encountered in hot gas path of a turbine exceed $1500°C$, beyond the material limit for gas turbine components. It is the function of cooling system to block or remove heat imparted to the turbine components and maintain component temperature within operating range to ensure their structural integrity and optimal life cycle. Cooling of turbine components in hot gas path is an active area of research and means to achieve higher turbine efficiency. Usually a combination of internal and external cooling techniques is employed to achieve reliable and effective cooling. Film cooling of a gas turbine component is an external cooling technique used to reduce the component temperature by reducing the heat flux from hot gases to the component material. Typically, an inclined coolant jet is used to effuse the coolant into hot crossflow to form a film of coolant fluid separating the hot gases from turbine component surface. Primary function of film cooling is to block the heat transfer to the component while internal cooling techniques remove heat from components.

In practice film cooling is realized by drilling an array of inclined holes on blade surface. A typical example of film cooled turbine blade shown in Figure 1.5a where rows of film cooling holes are drilled on surface of turbine blade. A representative 3D CAD model (Figure 1.5b) shows the delivery tube connecting the internal cooling passage acting as plenum chamber for film cooling holes.

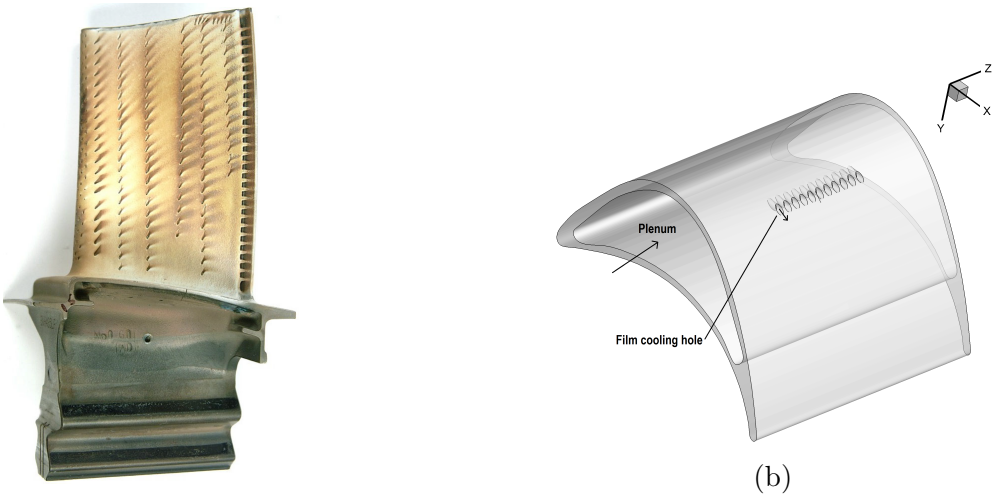


(a) (b)

Figure 1.5: Gas turbine blade

The coolant fluid is typically bled from the HP compressor at a higher pressure and fed to the internal cooling passage. The coolant effusing out of cooling holes forms a protective film of relatively cool fluid (air) over the turbine component surface. The effective formation of the cooling film and sustaining it for a range of condition encountered throughout the operation cycle is the goal of film cooling design. About 20-30% of compressed air is drawn in current gas turbines as coolant fluid from compressor stage. This fluid does not contribute in producing the work in turbine stage and excessive coolant reduces working fluid temperature, sacrificing efficiency. Thus, the essence of film cooling technique is in providing maximum cooling effect by using minimum coolant fluid.

### 1.3.1 Heat transfer and performance of film cooling

Convective heat transfer over a material surface is given as,

$$q_0'' = h_0(T_\infty - T_s) \tag{1.1}$$

where, $T_\infty$ is hot gas temperature flowing over the component, $T_s$ is surface temperature of the component and $h$ is convective heat transfer coefficient. In many convective heat

transfer scenario a correlation may be obtained for $h$ based on the choice of temperature difference driving the heat transfer. In case of flow with film cooling jets the heat transfer is driven by the film temperature near the wall and not by the free stream bulk temperature. Therefore, equation (1.1) is modified with an assumption of thin thermal boundary layer,

$$q''_{fc} = h_{fc}(T_a - T_s) \tag{1.2}$$

such that, adiabatic wall temperature $T_a$ is a close estimation of $T_\infty$ driving heat flux into the component material. Thus, reduction in $T_a$ by the usage of film cooling jet would result in direct reduction in heat flux to the turbine component for a target wall temperature $T_s$.

The film cooling performance is measured in terms of non-dimensional temperature $\theta$ that represents the actual cooling achieved relative to full cooling potential and known as film cooling effectiveness $\theta$, defined as,

$$\theta = \frac{T_\infty - T_s}{T_\infty - T_c} \in [0, 1] \tag{1.3}$$

where $T_s$ is blade surface temperature, $T_c$ is coolant temperature, $T_\infty$ is hot gas or crossflow temperature. Following the necessity for equation (1.2), for adiabatic conditions, $T_s = T_a$ and adiabatic film cooling effectiveness is given as,

$$\eta = \frac{T_\infty - T_a}{T_\infty - T_c} \in [0, 1] \tag{1.4}$$

Taking equation (1.1) as heat flux without film cooling and using equation (1.3) and (1.4) the factor of reduction in heat flux may be given as,

$$q''_r = 1 - \frac{h_{fc}(T_a - T_s)}{h_0(T_\infty - T_s)} = 1 - \frac{h_{fc}}{h_0}\left(1 - \frac{\eta}{\theta}\right) \tag{1.5}$$

Although heat transfer coefficient may be influenced due to film cooling jet, the effect of possible increased $h_{fc}$ is mitigated by reduction in $\eta$. Thus, for a target value of $\theta$ the

reduction of heat flux strongly depends on adiabatic film cooling effectiveness $\eta$. Therefore, adiabatic film cooling effectiveness is used to characterize the performance of film cooling hole, as higher adiabatic film cooling effectiveness indicates reduction in heat transfer potential $T_a - T_s$ driving heat to the component material. With this preamble to heat transfer in film cooling flows, the objective of film cooling design remains, to keep coolant fluid attached to the cooling surface covering maximum area and reduce mixing of jet and freestream fluid.

### 1.3.2 Jet in crossflow background

Fundamental configuration of film cooling flows is that of jets in crossflow (JICF). Study began as an investigation of chimney plumes (1932) and smoke dispersion from industrial smoke stacks. Later applications were developed in in later half of 1940s mainly for military applications of JICF, such as V/STOL, combustor cooling and thrust vectoring system. A summary of work before 1993 is presented by Margason (1993) in his famous paper 50 years of jet in crossflow research. A number of experimental and computational studies are devoted for identifying dynamic mechanisms responsible for genesis of coherent structures in JICF. A representative list of such studies is, (Sykes et al., 1986; Andreopoulos and Rodi, 1984; Coelho and Hunt, 1989; Krothapalli et al., 1990; Fric and Roshko, 1994; Kelso and Smits, 1995; Kelso et al., 1996; Haven and Kurosaka, 1997; Yuan et al., 1999; Lim et al., 2001; Sau and Mahesh, 2008; Ilak et al., 2012). Collective focus of all these studies was on four basic flow structures viz. (i) counter rotating vortex pair (kidney pair), (ii) Kelvin-Helmholtz shear layer structures, (iii) horse shoe vortex and (iv) wake vortices (tornado like structures).

The interaction of these flow structures in the flow field give rise to a highly three dimensional, anisotropic flow and making conclusive observations a challenging task. As a result several theories about initiation mechanism of these structures were proposed. Although there is general consensus about multiple initiation mechanisms for all four fundamental vortical structures of JICF, the topic remains an active area of research. A detailed discussion on flow physics is provided in chapter 5 and role of each flow structure is discussed in

context of current inclined jet in crossflow with an historical perspective.

### 1.3.3 A perspective on film cooling studies

A huge amount of effort has been out in film cooling research, to investigate the effect of a variety of parameters and optimize film cooling performance. In short, the film cooling effectiveness of a single discrete film cooling hole depends a set of geometric and flow parameters,

$$\eta = f(\Phi, \beta, l/D, B.R., D.R., I, Re_D, \tau, S) \tag{1.6}$$

$\Phi$ - angle of injection,$\beta$ is compound angle, delivery tube aspect ratio - $l/D$, blowing ratio $B.R = (\rho_j V_j)/(\rho_\infty V_\infty)$, density ratio $D.R = \rho_j/\rho_\infty$, momentum flux ratio $I = (\rho_j V_j^2)/(\rho_\infty V_\infty^2)$, Reynolds number $Re_D$, cross flow conditions upstream (turbulence and boundary layer thickness) $\tau$ and film cooling hole shape $S$

Blowing ratio $B.R = (\rho_j V_j)/(\rho_\infty V_\infty)$ is the ratio of jet mass flux to crossflow mass flux. Blowing ratio is most important control parameter due to $(i)$ its significant influence on jet behavior and $(ii)$ controllability. Therefore, blowing ratio is most commonly studied control parameter and reported by almost all the investigators in film cooling community. At low blowing ratio, the jet quickly spreads as it emerges out of film cooling hole due to smearing effect of crossflow. Therefore, higher film cooling effectiveness in the near hole regions and increased overall coolant spreading is observed. However, a rapid decay in film cooling effectiveness in streamwise direction is observed smaller mass coolant mass flow rate . At moderate blowing ratios the overall increased film cooling effectiveness is attributed to increased mass flow rate and moderate to less tendency of jet liftoff. At higher blowing ratios ($> 1$) the jet liftoff is witnessed immediately downstream of film cooling hole and partial reattachment is observed and recovering the film cooling effectiveness far downstream of the film cooling hole (Sinha et al., 1991; Baldauf et al., 2002).

Density ratio $D.R. = \rho_j/\rho_\infty$ is ratio of jet fluid density to crossflow fluid density. Density ratio may be seen as means to control the velocity ratio for a target blowing ratio. This

leads to realization of drastically different characteristics of primary shear layer. A more detailed discussion will be done in flow physics section in the context of present case ($D.R = 2.0$). Goldstein et al. (1974) observed that for identical blowing ratio higher film cooling effectiveness is found for $D.R. > 1.0$. Pedersen et al. (1977) conducted first comprehensive study of velocity ratio, mass flux ratio and momentum flux ratio for a number of density ratio. Accurate measurements of adiabatic film cooling effectiveness for variable density jets ($D.R. = 1.2 - 2.0$) were performed by Sinha et al. (1991) their observation was similar to (Goldstein et al., 1974), that lateral spreading increased with density ratio for a given mass flux ratio.

A film cooling hole is called cound angle when the major axis of exit cross section geometry of film cooling hole is oriented at an angle $\beta$ with the crossflow direction. The resulting film cooling hole configuration is called compound angle film cooling hole. The roots of compound angle injection concepts are found in Goldstein et al. (1970) and caught attention in early 1990 with Mehendale and Han (1992), Ligrani et al. (1992), Schmidt et al. (1996). Lee et al. (1997) showed compund angle $\beta$ significantly influences the formation of counter rotating vortex pair (CRVP). For $\beta = 15^\circ$ they observed complete merging of CRVP to form a single vortex. Jung and Lee (2000) studied the effect of compound angle $0^\circ$, $30^\circ$, $60^\circ$, $90^\circ$ for velocity ratios 0.5, 1.0, 2.0. They reported increased over all effectiveness for higher orientation angle and higher velocity ratios. The primary reason cited for improvements are higher entrainments and mixing of crossflow fluid leading to spreading of the coolant fluid.

An ideal film cooling would be a tangential jet with $0^\circ$ injection angle parallel to free stream flow. However, in practice $30^\circ$ and $35^\circ$ angle of injection is preferred for manufacturing constraints. Baldauf et al. (2002) investigated the effect of hole injection angle for $30^\circ$, $60^\circ$ and $90^\circ$ jets. They found for momentum flux ratio $I < 1.0$ jets with lower inclination angle show higher over all film cooling effectiveness. The performance difference of $\leq 10\%$ was observed between $30^\circ$ and $60^\circ$ inclined jet, whereas in excess of 30% performance loss was observed for $90^\circ$ inclined jet. However, for higher momentum flux ratio $I > 1.0$ film cooling

performance of 60° and 90° inclined jets were better than 30° inclined jet. Baldauf et al. (2002) attributed this observation to significantly higher mixing of jet and crossflow fluid at higher jet inclination angles. Although the optimal film cooling performance is observed at smaller inclination angle with low blowing ratio, in some cases to negate the risk of hot gas ingestion in film cooling hole higher blowing ratios, usually in the range $1.0 - 2.0$ are preferred. Therefore, injection angle plays a rather less significant role for $I > 1.0$ and a significant performance factor for $I < 1.0$.

Effect of film cooling hole aspect ratio is significant on film cooling performance as, the jet exit conditions vary significantly with aspect ratio. This parameter is particularly important in the context of inclined jet film cooling where the flow entering the delivery tube from plenum chamber separates and a wake region is formed within delivery tube. For a long delivery tube, the re-attachment of jet is observed within delivery tube with partially developed conditions at the jet exit. However, for short delivery tubes, the wake region may get swept out and interact with crossflow. Higher film cooling effectiveness is observed for the same blowing ratio for higher aspect ratio ($l/D$) delivery tube(Acharya and Leedom, 2013). The wake in leeward region causes local jet acceleration in the windward region of delivery tube, resulting in locally high blowing ratio therefore increased tendency of jet liftoff. For longer delivery tube the jet may reattach and local blowing ratios are closer to the target value hence increased film cooling performance compared to former case.

Modifying the hole exit geometry received a lot of attention in the decade of 1990 and onward. Goldstein et al. (1974) noted that widening of the jet exit cross-section leads to deceleration of the coolant fluid and increased lateral spreading. With coolant mass flow rate remaining same, a significant improvement in the film cooling performance is observed. Another important effect of hole exit geometry on the vertical jet characteristics was observed by Haven and Kurosaka (1997) in the form of Anti-vortex pair formed on the top region of the jet. Diminishing jet lift off and increased concentration of jet tracer on bottom wall was associated with the formation of anti-vortex pair. Other techniques of creating anti-vortex

pair by usage of triangular tab at the upstream edge of film cooling hole was devised by Nasir et al. (2003). However, from manufacturing and reliability point of view the viable options are (*i*) shaped holes, (*ii*) film cooling holes embedded in craters and (*iii*) film cooling holes embedded in trenches. An excellent review of shaped film cooling holes mat be found at (Bunker, 2005). The idea of film cooling hole embedded in transverse trenches originated from (Bunker, 2001) and soon after, the idea of film cooling hole embedded in craters was patented by Fric and Campbell (2002). The central idea behind craters and trenches is to provide the cooling fluid an sudden expansion volume that allows reduction in local blowing ratio without reduction in mass flow rate of the coolant. Additionally, higher mixing and lateral spreading is observed. A rather significant effect of craters and trenches is to disrupt the development of CRVP from the boundary layer vorticity (mechanism described by Haven and Kurosaka (1997)). Craters and trenches may be manufactured in the protective layer of thermal barrier coating and not necessarily be machined in the metal of turbine blade. This provides a unique advantage from a manufacturing point of view although craters and trenches do not perform at par with shaped holes. However, they are susceptible to hot gas ingestion in the cratered/trenched region and must be carefully designed to avoid associated thermal failures.

### 1.3.4 Effect of inlet conditions $\tau$

Although the mass flux ratio of momentum flux ratio is determined with average velocity of jet and crossflow, the locally these parameters may have large variations. The source of variations are rooted in jet exit conditions as discussed in context of hole aspect ratio and crossflow boundary layer thickness. Higher crossflow boundary layer thickness leads to higher tendency of jet penetration and liftoff. Additionally, turbulence levels in incoming crossflow boundary layer is critical in determining the cooling performance as it may lead to loss of cooling effectiveness and increase heat transfer coefficient. Lower blowing ratio jets are susceptible for upto 40% loss in cooling performance (Saumweber et al., 2002). This loss

is mainly associated with increased mixing. However, for higher blowing ratios the effect of crossflow boundary layer turbulence is minimal. This may be attributed to less susceptibility of film cooling jets to arbitrary external perturbation at higher blowing ratios.

## 1.4 Objective

Countercurrent shear layers are potential means for addressing the flow control, mixing and acoustic instability in combustors. There have been few fundamental and applied studies, mostly studying an suction based counter current shear layer that has sever limitations in practice. A momentum driven countercurrent shear flow offer an alternative to this issue however, fewer studies are reported. Therefore, one of the goal of current research is to numerically study characterize the flow dynamics of isothermal countercurrent shear flows. The specific goals in this regard are,

($a$) Obtain validated LES simulations to capture flow dynamics accurately.

($b$) Identify the instability mechanisms and quantify their characteristics for various parameters.

Film cooling flows are seen as primary means to improve thermodynamic efficiency of land based power generating and aviation gas turbine engines. Therefore, understanding the flow physics and quantifying various mechanisms involved in heat transfer and mixing is vital. The specific objectives of the film cooling study are,

($a$) Obtain validated LES simulations for the baseline case and study flow physics based on detailed flow visualization.

($b$) Quantify the contributions of coherent flow structures towards cooling effectiveness of film cooled wall and bulk mixing of coolant and cross flow fluid.

($c$) Use the knowledge gained from above studies to modify the film cooling geometry for improved film cooling performance.

## 1.5 Organization

Subsequent chapters of this dissertation are organized in following manner,

Chapter 2 describes the governing equations for flow and species transport for an incompressible Newtonian fluid. It discusses the implementation of large eddy simulation in curvilinear coordinate system and the validity of dynamic subgrid scale eddy viscosity model is established.

Chapter 3 presents the results of countercurrent shear flow analysis. Shear layer is simulated for three control parameters. The results are compared with available measurements for two cases. Spectral analysis of time series velocity signal, Orr-Sommerfeld analysis is performed to identify primary instability mechanism. A three dimensional stability analysis of entire flow field is performed to identify global mode and corresponding coherent flow structures. Lastly, the global mode frequency synchronization is described.

In Chapter 4 the effect of spanwise discrete secondary jets on momentum driven countercurrent shear flows is investigated. The objective of the study is the formulate a mechanism to retain the ability of countercurrent shear layers to excite and control turbulence while eliminating the large oscillations of secondary jet observed in case of spanwise continuous secondary jet observed in chapter 3

In chapter 5 a baseline film cooling flow geometry is simulated. The heat transfer and flow statistics are compared with experiments and validity of simulation is established. The flow physics is investigated by identifying coherent flow structures of film cooling flows, describing their origin and evolution. The role of identified coherent structures, in film cooling performance is discussed. Aforementioned study is based on extensive flow visualization.

In chapter 6 the time series flow field obtained in baseline simulation in chapter 5 is analysed with dynamic mode decomposition technique. The modes are ranked by their growth rate and energy content to identify dynamically and energetically significant modes and their time scales. The contribution of individual modes in film cooling effectiveness

variation is quantified and dominant modes are identified. The topological structure of dominant modes is then related to the coherent structures in the flow field.

In chapter 7 the mixing processes in inclined jet in cross flow (baseline case in chapter 5) is studied. The comparisons are drawn with the mixing characteristics of vertical jet in crossflow from earlier studies. A modal analysis using dynamic mode decomposition is done to quantify the mixing strength and active regions of coherent flow structures based on scalar dissipation rate.

In chapter 8 a design of film cooling hole embedded in new contoured crater is proposed. The film cooling performance of new design was evaluated for three depth parameters. The improved film cooling performance is shown over best performing craters and trench design. The flow physics is studied to identify the coherent structures/flow physics contributing to improved performance.

Finally, conclusion from the accomplished study are presented in chapter 9

# Chapter 2
# Computational Methodology

## 2.1 Computational tool overview

The computational tool used for the study is a three dimensional compressible flow solver code that uses a block structured grid system in curvilinear co-ordinate system. An in-house developed parallel multi-block chemically reacting compressible flow code for generalized curvilinear coordinates, CHEM3D, is used. For incompressible flows, low Mach number preconditioning is used (Weiss and Smith, 1995). A second order backward 3-point physical time differencing is used for the temporal derivatives. Second order low diffusion flux-splitting algorithm is used for convective terms (Edwards, 1997). Second order central differences are used for the viscous terms. An incomplete Lower-Upper (ILU) matrix decomposition solver is used. Domain decomposition and load balancing are accomplished using a family of programs for partitioning unstructured graphs and hypergraphs and computing fill-reducing ordering of sparse matrices, METIS. The message communication in distributed computing environment is achieved using Message Passing Interface, MPI (Gropp and Lusk, 1999). All the multi-block structured curvilinear grids presented in this paper are generated using commercial grid generation software GridProTM and ANSYS-ICEM CFD.

## 2.2 Block structured grid system

In a typical block structured grid the domain of interest in curvilinear co-ordinate system is topologically divided in a set of non-overlapping watertight hexahedral volumes. Each of such

volume has its local co-ordinate system with index (j,k,l) in respective $(\xi, \eta, \zeta)$ directions. In order to create the grid each of such volume is divided into the regular array of hexahedral cells. The connectivity of all the blocks is given in terms of the orientation of the local coordinate systems with the connected neighboring block. The connectivity oh hexahedral cells is implicit in the index space (j,k,l) in the local co-ordinate system. Such a grid in general can be viewed as unstructured at the block level and purely structured in the sub-block level. This feature offers the flexibility of handling complex flow domain in curvilinear coordinate system with higher order accurate numerical scheme. The topological division of the entire domain can be carefully done in such a way that the grid quality (importantly skewness and aspect ratio) can be controlled to achieve smoother and quality grids. Typically this is done by solving Poissons equations to obtain near orthogonal grids.

### 2.3 General Transport Equation

The transport equation for generic transport quantity $\phi$ is given by,

$$\frac{\partial}{\partial t}(\rho\phi) + \nabla \cdot (\rho u\phi) = \nabla \cdot (\Gamma \nabla\phi) + S \tag{2.1}$$

where $\rho$ is density, $u$ is convective velocity and $\Gamma$ is diffusivity. The unsteady and convective fluxes are respectively represented first two terms of left hand side. The first term on right hand side represent the diffusion and $S$ is a generic source term. In Cartesian coordinate system the conservation equation becomes,

$$\frac{\partial}{\partial t}(\rho\phi)+\frac{\partial}{\partial x}(\rho u\phi)+\frac{\partial}{\partial y}(\rho v\phi)+\frac{\partial}{\partial z}(\rho w\phi) = \frac{\partial}{\partial x}\left(\Gamma\frac{\partial\phi}{\partial x}\right)+\frac{\partial}{\partial y}\left(\Gamma\frac{\partial\phi}{\partial y}\right)+\frac{\partial}{\partial z}\left(\Gamma\frac{\partial\phi}{\partial z}\right)+S \tag{2.2}$$

The same equation in conservative form is written as,

$$\frac{\partial}{\partial t}(\rho\phi) + \frac{\partial}{\partial x}\left(\rho u\phi - \Gamma\frac{\partial\phi}{\partial x}\right) + \frac{\partial}{\partial y}\left(\rho v\phi - \Gamma\frac{\partial\phi}{\partial y}\right) + \frac{\partial}{\partial z}\left(\rho w\phi - \Gamma\frac{\partial\phi}{\partial z}\right) = S \tag{2.3}$$

Representing convective fluxes in $x$,$y$,$z$ direction by $E$,$F$ and $G$ and viscous terms by $E_v$,$F_v$ and $G_v$ respectively. The flux conservation equation becomes,

$$\frac{\partial}{\partial t}(\rho\phi) + \frac{\partial}{\partial x}(E - E_v) + \frac{\partial}{\partial y}(F - F_v) + \frac{\partial}{\partial z}(G - G_v) = S \tag{2.4}$$

## 2.4 Governing equations

$$\frac{\partial}{\partial t}(\hat{Q}) + \frac{\partial}{\partial x}(\hat{E} - \hat{E}_v) + \frac{\partial}{\partial y}(\hat{F} - \hat{F}_v) + \frac{\partial}{\partial z}(\hat{G} - \hat{G}_v) = \hat{S} \tag{2.5}$$

$$\begin{aligned}
\hat{Q} &= \frac{1}{J}Q & \hat{H} &= \frac{1}{J}H \\
\hat{E} &= \frac{1}{J}\left(\xi_x E + \xi_y F + \xi_z G\right) & \hat{E}_v &= \frac{1}{J}\left(\xi_x E_v + \xi_y F_v + \xi_z G_v\right) \\
\hat{F} &= \frac{1}{J}\left(\eta_x E + \eta_y F + \eta_z G\right) & \hat{F}_v &= \frac{1}{J}\left(\eta_x E_v + \eta_y F_v + \eta_z G_v\right) \\
\hat{G} &= \frac{1}{J}\left(\zeta_x E + \zeta_y F + \zeta_z G\right) & \hat{G}_v &= \frac{1}{J}\left(\zeta_x E_v + \zeta_y F_v + \zeta_z G_v\right)
\end{aligned} \tag{2.6}$$

The conserved variable and Cartesian inviscid fluxes are,

$$Q = [\rho Y_1, ...., \rho Y_N, \rho u, \rho v, \rho w, E_t]^T \tag{2.7}$$

$$E = \left[\rho u Y_1, ...., \rho u Y_N, \rho u^2 + p, \rho uv, \rho uw, (E_t + p)u\right]^T \tag{2.8}$$

$$F = \left[\rho v Y_1, ...., \rho v Y_N, \rho uv, \rho v^2 + p, \rho vw, (E_t + p)v\right]^T \tag{2.9}$$

$$G = \left[\rho w Y_1, ...., \rho w Y_N, \rho uw, \rho vw, \rho w^2 + p, (E_t + p)w\right]^T \tag{2.10}$$

The viscous fluxes are given as,

$$E_v = [q_{x1}, ...., q_{xN}, \tau_{xx}, \tau_{xy}, \tau_{xz}, (\overrightarrow{u} \cdot \nabla\tau)_x + q_{xe}]^T \tag{2.11}$$

$$F_v = [q_{y1}, ...., q_{yN}, \tau_{xy}, \tau_{yy}, \tau_{yz}, (\overrightarrow{u} \cdot \nabla\tau)_y + q_{ye}]^T \tag{2.12}$$

$$G_v = [q_{z1}, ...., q_{zN}, \tau_{xz}, \tau_{yz}, \tau_{zz}, (\overrightarrow{u} \cdot \nabla\tau)_z + q_{ze}]^T \tag{2.13}$$

The viscous components are given as,

$$\begin{aligned}
\tau_{xx} &= 2\mu_e \frac{\partial u}{\partial x} - \frac{2}{3}\mu_e \left(\frac{\partial u}{\partial x} + \frac{\partial v}{\partial y} + \frac{\partial w}{\partial z}\right) & \tau_{xy} &= \tau_{yx} = \mu_e \left(\frac{\partial v}{\partial x} + \frac{\partial u}{\partial y}\right) \\
\tau_{yy} &= 2\mu_e \frac{\partial v}{\partial y} - \frac{2}{3}\mu_e \left(\frac{\partial u}{\partial x} + \frac{\partial v}{\partial y} + \frac{\partial w}{\partial z}\right) & \tau_{yz} &= \tau_{zy} = \mu_e \left(\frac{\partial v}{\partial z} + \frac{\partial w}{\partial y}\right) \\
\tau_{zz} &= 2\mu_e \frac{\partial w}{\partial z} - \frac{2}{3}\mu_e \left(\frac{\partial u}{\partial x} + \frac{\partial v}{\partial y} + \frac{\partial w}{\partial z}\right) & \tau_{xz} &= \tau_{zx} = \mu_e \left(\frac{\partial u}{\partial z} + \frac{\partial w}{\partial x}\right)
\end{aligned} \tag{2.14}$$

The energy fluxes in the three coordinate directions are given by,

$$q_{xe} = k_e \frac{\partial T}{\partial x} + \rho \sum\nolimits_{s=1}^{N} h_s D_{sm} \frac{\partial Y_s}{\partial x} \tag{2.15}$$

$$q_{ye} = k_e \frac{\partial T}{\partial y} + \rho \sum\nolimits_{s=1}^{N} h_s D_{sm} \frac{\partial Y_s}{\partial y} \tag{2.16}$$

$$q_{ze} = k_e \frac{\partial T}{\partial z} + \rho \sum\nolimits_{s=1}^{N} h_s D_{sm} \frac{\partial Y_s}{\partial z} \tag{2.17}$$

where $T$ is the temperature and $k_e$ is effective thermal conductivity.

### 2.4.1 Low Mach number preconditioning

In order to handle the low velocity flows in the incompressible regime a low mach number preconditioner (Weiss and Smith, 1995) has been used to rescale the acoustic scales to the convective scales. The pseudo derivative if a dependent primitive variable is added to the transport equation as,

$$\Gamma\frac{\partial\hat{U}}{\partial\tau}+\frac{\partial}{\partial t}\hat{Q}+\frac{\partial}{\partial x}(\hat{E}-\hat{E}_v)+\frac{\partial}{\partial y}(\hat{F}-\hat{F}_v)+\frac{\partial}{\partial Z}(\hat{G}-\hat{G}_v)=\hat{S} \tag{2.18}$$

where $\hat{U}$ the dependent variable is defined as the vector comprised of primitive variables.

$$\hat{U}=\frac{1}{J}[p1,p2,...,pN,u,v,w,T]^T \tag{2.19}$$

and preconditioning matrix $\Gamma$ is given as,

$$\Gamma=\begin{bmatrix}
\frac{W_1}{RT}+\Theta Y & \Theta Y_1 & \cdots & \Theta Y_1 & 0 & 0 & 0 & -\frac{\rho_1}{T} \\
\Theta Y_2 & \frac{W_2}{RT}+\Theta Y_2 & \cdots & \Theta Y_2 & 0 & 0 & 0 & -\frac{\rho_2}{T} \\
\cdots & \cdots & \cdots & \cdots & \cdots & \cdots & \cdots & \cdots \\
\Theta Y_N & \Theta Y_N & \cdots & \frac{W_N}{RT}+\Theta Y_2 & 0 & 0 & 0 & -\frac{\rho_N}{T} \\
u\left(\frac{W_1}{RT}+\Theta\right) & u\left(\frac{W_2}{RT}+\Theta\right) & \cdots & u\left(\frac{W_N}{RT}+\Theta\right) & \rho & 0 & 0 & -\frac{\rho u}{T} \\
v\left(\frac{W_1}{RT}+\Theta\right) & v\left(\frac{W_2}{RT}+\Theta\right) & \cdots & v\left(\frac{W_N}{RT}+\Theta\right) & 0 & \rho & 0 & -\frac{\rho v}{T} \\
w\left(\frac{W_1}{RT}+\Theta\right) & w\left(\frac{W_2}{RT}+\Theta\right) & \cdots & w\left(\frac{W_N}{RT}+\Theta\right) & 0 & 0 & \rho & -\frac{\rho w}{T} \\
\alpha_1 & \alpha_2 & \cdots & \alpha_N & \rho u & \rho v & \rho w & \rho\left(C_{pm}-\frac{H}{T}\right)
\end{bmatrix}$$

where,

$$\Theta=\frac{1}{U_{ref}^2}-\frac{1}{a^2} \tag{2.20}$$

$$U_{ref}=min\left[a^2,max\left(|\overrightarrow{V}|^2,k,|\overrightarrow{V_\infty}|^2\right)\right] \tag{2.21}$$

For $p^{th}$ species,

$$\alpha_p=H\left(\Theta+\frac{W_p}{RT}\right)-1 \tag{2.22}$$

$H$ is enthalpy per unit mass, $|\overrightarrow{V}|$ is the local velocity magnitude, $|\overrightarrow{V_\infty}|$ is reference velocity, $a$ is the local sound speed and $K$ is a constant.

Eq 18 gives the unsteady transport equation for a chemically reacting mixture of N species in a generalized coordinate system. The N continuity equations solved to calculate partial pressures of each species and three momentum equations and the energy equation. The eq. 18 is system of N+4 coupled partial differential equations. The following numerical method is used to solve the system of non-linear equations.

### 2.4.2 Numerical Method

A second order accurate three point physical time differencing scheme is used,

$$\frac{\partial \hat{Q}_1}{\partial t} = \frac{3\hat{Q}_i^{n+1} - 4\hat{Q}_i^n + \hat{Q}_i^{n-1}}{2\Delta t} \tag{2.23}$$

where $n$ is time level and $i$ is position in three dimensional spatial index space. $\Delta t$ is physical time increment. Pseudo-time derivatives is evaluated using standard two pint Euler differencing,

$$\frac{\partial \hat{U}_i^{n,p+1}}{\partial \tau} = \frac{\hat{U}_i^{n,p+1} - \hat{U}_i^{n,p}}{\Delta \tau} \tag{2.24}$$

### 2.4.3 Low Diffusion Flux Splitting Scheme (Edwards 1997)

The transformed Navier-Stokes equation in flux conservative form is given as,

$$\Gamma \frac{\partial \hat{U}}{\partial \tau} + \frac{\partial}{\partial t}\hat{Q} + \frac{\partial}{\partial x}\left(\hat{E} - \hat{E}_v\right) + \frac{\partial}{\partial y}\left(\hat{F} - \hat{F}_v\right) + \frac{\partial}{\partial z}\left(\hat{G} - \hat{G}_v\right) = \hat{S} \tag{2.25}$$

The fluxes in transformed co-ordinate system are split in convective and pressure part. The viscous fluxes are separately calculated using second order central differencing scheme. The typical convective flux in $\xi$ direction is split as,

$$\hat{E}_{i+1/2} = \hat{E}^c_{i+1/2} + \hat{E}^p_{i+1/2} \tag{2.26}$$

where $i+1/2$ is a finite volume cell face location in $\xi$ direction. Superscript $c$ and $p$ stands for convective and pressure part respectively. The convective and pressure fluxes for compressible flows is split in two components right and left denoted by superscript + and  respectively. Splitting of convective part is given as,

$$\hat{E}_{i+1/2} = U^{+}\hat{W}_L + U^{-}\hat{W}_R \tag{2.27}$$

where $\hat{W}$ is primary variable vector,

$$\hat{W} = [p_1, p_2, ..., p_N, u, v, w, T] \tag{2.28}$$

$$\hat{W}_L = \hat{W}_i + \frac{\Gamma_i \Psi_i}{2} \tag{2.29}$$

$$\hat{W}_R = \hat{W}_{i+1} - \frac{\Gamma_{i+1} \Psi_{i+1}}{2} \tag{2.30}$$

with,

$$\Gamma_i = \left(1 - \frac{|p_{i+1} - p_{i-1}|}{|p_{i+1} - p_{i-1}| + \varepsilon p_{ref}}\right) \tag{2.31}$$

and,

$$\Psi_i = \frac{(\Delta_+^2 + \varepsilon)\Delta_- + (\Delta_-^2 + \varepsilon)\Delta_+}{(\Delta_+^2 + \Delta_-^2 + 2\varepsilon^2)} \tag{2.32}$$

$$\Delta_+ = \hat{W}_{i+1} - \hat{W}_i \tag{2.33}$$

$$\Delta_- = \hat{W}_i - \hat{W}_{i-1} \tag{2.34}$$

and $\epsilon$ is a constant.

Now,

$$U^{\pm} = \hat{a}_{1/2}\left[M \pm M_{1/2}\left(1 - \frac{P_L - P_R}{2\rho V^2}\right)\right] \tag{2.35}$$

where, $\hat{a}_{1/2}$ is geometric mean of sound speed based on temperature and pressure component of $\hat{W}_L$ and $\hat{W}_R$

The Mach numbers terms are calculated as,

$$M = \frac{U_{abs}}{a_{abs}} \tag{2.36}$$

$$M_{1/2} = 0.25\beta_L\beta_R\left[\sqrt{\frac{1}{2}(M_L^2 + M_R^2)} - 1\right]^2 \tag{2.37}$$

where,

$$M_{L,R} = \frac{u_{L,R}}{\hat{a}_{L,R}} \tag{2.38}$$

$$\beta_{L,R} = -max\left(0, 1 - int(|M_{L,R}|)\right) \tag{2.39}$$

The pressure splitting is given as,

$$P_{L,R} = \frac{1}{4}(M_{L,R} + 1)^2(1 \mp M_{L,R}) \tag{2.40}$$

The net pressure in-terms of $P_L$ and $P_R$ and is given as,

$$P_{net} = \frac{1}{2}(P_L + P_R) + \frac{1}{2}(P_L + P_R)(P^+ - P^-) + \rho V_{ref}^2(P^+ + P^- + 1) \tag{2.41}$$

where,

$$P^{\pm} = \alpha_{L,R}(1 + \beta_{L,R}) - \beta_{L,R}P_{L,R} \tag{2.42}$$

$$\alpha_{L,R} = \frac{1}{2}(1 + sgn(M_{L,R})) \tag{2.43}$$

### 2.4.4 Linearizion and solution scheme

The Discretized linear equations for an arbitrary point in computational grid $(j,k,l)$ at $(n+1)^{th}$ time step and $(p+1)^{th}$ pseudo time step is following,

$$\begin{aligned}
&\frac{\Gamma}{\Delta\tau}\left(\hat{U}_i^{p+1,n+1}-\hat{U}_i^{p,n+1}\right)+\frac{1}{\Delta t}\left(3\hat{Q}_i^{n+1}-4\hat{Q}_i^{n}+\hat{Q}_i^{n-1}\right)\\
&+\left[\hat{E}-\hat{E}_v\right]_{j+1/2}^{p+1,n+1}-\left[\hat{E}-\hat{E}_v\right]_{j-1/2}^{p+1,n+1}\\
&+\left[\hat{F}-\hat{F}_v\right]_{k+1/2}^{p+1,n+1}-\left[\hat{F}-\hat{F}_v\right]_{k-1/2}^{p+1,n+1}\\
&+\left[\hat{G}-\hat{G}_v\right]_{l+1/2}^{p+1,n+1}-\left[\hat{G}-\hat{G}_v\right]_{l-1/2}^{p+1,n+1}=\hat{H}_i^{p+1,n+1}
\end{aligned} \tag{2.44}$$

The solution vector is the change in dependent variable and is defined as,

$$\delta\hat{U}_i^{p+1}=\hat{U}_i^{p+1}-\hat{U}_i^{p} \tag{2.45}$$

The linearization for generic variable $v$ is given as,

$$P_{1\pm1/2}^{p+1,n+1}=v_{1\pm1/2}^{p,n+1}+\partial_{\hat{u}}v_{i\pm1/2}\delta\hat{U}_{i\pm1/2}^{p+1,n+1} \tag{2.46}$$

and corresponding jacobian are givena as,

.

$$\delta_{\tilde{u}}\hat{P} = \begin{bmatrix} \frac{UW_1}{RT} & 0 & \cdots & 0 & \rho_1 k_x & \rho_1 k_y & \rho_1 k_z & -\frac{\rho_1 U}{T} \\ 0 & \frac{UW_2}{RT} & \cdots & 0 & \rho_2 k_x & \rho_2 k_y & \rho_2 k_z & -\frac{\rho_2 U}{T} \\ \cdots & \cdots & \cdots & \cdots & \cdots & \cdots & \cdots & \cdots \\ 0 & 0 & \cdots & \frac{UW_N}{RT} & \rho_N k_x & \rho_N k_y & \rho_N k_z & -\frac{\rho_N U}{T} \\ U_u\left(\frac{W_1}{RT}+k_x\right) & U_u\left(\frac{W_2}{RT}+k_x\right) & \cdots & U_u\left(\frac{W_N}{RT}+k_x\right) & \rho & 0 & 0 & -\frac{\rho U_u}{T} \\ U_v\left(\frac{W_1}{RT}+k_y\right) & U_v\left(\frac{W_2}{RT}+k_y\right) & \cdots & U_v\left(\frac{W_N}{RT}+k_y\right) & 0 & \rho & 0 & -\frac{\rho U_v}{T} \\ U_w\left(\frac{W_1}{RT}+k_z\right) & U_w\left(\frac{W_2}{RT}+k_z\right) & \cdots & U_w\left(\frac{W_N}{RT}+k_z\right) & 0 & 0 & \rho & -\frac{\rho U_w}{T} \\ Uh_{t1}\frac{W_1}{RT} & Uh_{t2}\frac{W_2}{RT} & \cdots & Uh_{tN}\frac{W_N}{RT} & \rho(uU+hk_x) & \rho(vU+hk_y) & \rho(wU+hk_z) & \rho U\left(C_{pm}-\frac{H}{T}\right) \end{bmatrix}$$

$$U = uk_x + vk_y + wk_z \tag{2.47}$$

$$\delta_{\tilde{u}}\hat{Q} = \begin{bmatrix} \Lambda D_{im}\beta_1(1-Y_1) & \Lambda D_{im}\beta_2 Y_1 & \cdots & \Lambda D_{im}\beta_N Y_1 & 0 & 0 & 0 & 0 \\ \Lambda D_{im}\beta_1 Y_2 & \Lambda D_{im}\beta_2(1-Y_2) & \cdots & \Lambda D_{im}\beta_N Y_2 & 0 & 0 & 0 & 0 \\ \vdots & \vdots & \vdots & \vdots & \vdots & \vdots & \vdots & \vdots \\ \Lambda D_{im}\beta_1 Y_N & \Lambda D_{im}\beta_2 Y_N & \cdots & \Lambda D_{im}\beta_N(1-Y_N) & 0 & 0 & 0 & 0 \\ 0 & 0 & \cdots & 0 & \mu_e\left(\Lambda+\frac{k_x^2}{3}\right) & \mu_e\frac{k_x k_y}{3} & \mu_e\frac{k_x k_z}{3} & 0 \\ 0 & 0 & \cdots & 0 & \mu_e\frac{k_x k_y}{3} & \mu_e\left(\Lambda+\frac{k_y^2}{3}\right) & \mu_e\frac{k_y k_z}{3} & 0 \\ 0 & 0 & \cdots & 0 & \mu_e\frac{k_x k_z}{3} & \mu_e\frac{k_y k_z}{3} & \mu_e\left(\Lambda+\frac{k_z^2}{3}\right) & 0 \\ \Lambda\beta_1(h1-h_m) & \Lambda\beta_2(h2-h_m) & \cdots & \Lambda\beta_N(h_N-h_m) & \pi_u & \pi_v & \pi_w & k_e\Lambda C_{pm} \end{bmatrix}$$

$$\Lambda = k_x^2 + k_y^2 + k_z^2 \tag{2.48}$$

$$\pi_u = \mu_e\left(\Lambda + \frac{k_x^2}{3}\right)u + \mu_e\frac{k_x k_y}{3}v + \mu_e\frac{k_x k_z}{3}w \tag{2.49}$$

$$\pi_v = \mu_e\frac{k_x k_y}{3}u + \mu_e\left(\Lambda + \frac{k_y^2}{3}\right)v + \mu_e\frac{k_y k_z}{3}w \tag{2.50}$$

$$\pi_w = \mu_e\frac{k_x k_z}{3}u + \mu_e\frac{k_y k_z}{3}v + \mu_e\left(\Lambda + \frac{k_z^2}{3}\right)w \tag{2.51}$$

$$\delta_{\tilde{u}}\hat{Q} = \begin{bmatrix} \frac{W_1}{RT} & 0 & \cdots & 0 & 0 & 0 & 0 & -\frac{\rho_1}{T} \\ 0 & \frac{W_2}{RT} & \cdots & 0 & 0 & 0 & 0 & -\frac{\rho_2}{T} \\ \cdots & \cdots & \cdots & \cdots & \cdots & \cdots & \cdots & \cdots \\ 0 & 0 & \cdots & \frac{W_N}{RT} & 0 & 0 & 0 & -\frac{\rho_N}{T} \\ u\left(\frac{W_1}{RT}\right) & u\left(\frac{W_2}{RT}\right) & \cdots & u\left(\frac{W_N}{RT}\right) & \rho & 0 & 0 & -\frac{\rho u}{T} \\ v\left(\frac{W_1}{RT}\right) & v\left(\frac{W_2}{RT}\right) & \cdots & v\left(\frac{W_N}{RT}\right) & 0 & \rho & 0 & -\frac{\rho v}{T} \\ w\left(\frac{W_1}{RT}\right) & w\left(\frac{W_2}{RT}\right) & \cdots & w\left(\frac{W_N}{RT}\right) & 0 & 0 & \rho & -\frac{\rho w}{T} \\ \Lambda_1 & \Lambda_2 & \cdots & \Lambda_N & \rho u & \rho v & \rho w & \delta_T E_t \end{bmatrix}$$

$$\Lambda_i = \frac{1}{\gamma - 1} + \frac{W_i}{2RT}(u^2 + v^2 + w^2) \tag{2.52}$$

$$E_t = \rho\left[e + \frac{1}{2}(u^2 + v^2 + w^2)\right] \tag{2.53}$$

$$\delta_T E_t = \frac{\rho R}{\gamma - 1} - \frac{\rho}{T}\left[e + \frac{1}{2}(u^2 + v^2 + w^2)\right] \tag{2.54}$$

$$\begin{aligned} &\left(\frac{\Gamma}{\Delta\tau}\delta_{\tilde{U}}\hat{H}_i + \frac{1.5}{\Delta t}\hat{Q}_i\right)\delta\hat{U}_i^{p+1,n+1} \\ &+ \left[\delta_{\tilde{U}}\hat{E} - \delta_{\tilde{U}}\hat{E}_v\right]_{j+1/2}\delta\tilde{U}_{j+1/2}^{p+1,n+1} - \left[\delta_{\tilde{U}}\hat{E} - \delta_{\tilde{U}}\hat{E}_v\right]_{j-1/2}\delta\tilde{U}_{j-1/2}^{p+1,n+1} \\ &+ \left[\delta_{\tilde{U}}\hat{F} - \delta_{\tilde{U}}\hat{F}_v\right]_{k+1/2}\delta\tilde{U}_{k+1/2}^{p+1,n+1} - \left[\delta_{\tilde{U}}\hat{F} - \delta_{\tilde{U}}\hat{F}_v\right]_{k-1/2}\delta\tilde{U}_{k-1/2}^{p+1,n+1} \\ &+ \left[\delta_{\tilde{U}}\hat{G} - \delta_{\tilde{U}}\hat{G}_v\right]_{l+1/2}\delta\tilde{U}_{l+1/2}^{p+1,n+1} - \left[\delta_{\tilde{U}}\hat{G} - \delta_{\tilde{U}}\hat{G}_v\right]_{l-1/2}\delta\tilde{U}_{l-1/2}^{p+1,n+1} = RHS^{p,n+1} \end{aligned} \tag{2.55}$$

$$RHS^{p,n+1} = \left\{ \begin{array}{l} \left(1.5\hat{Q}_i^{p,n+1} - 2\hat{Q}_i^{p,n} + 0.5\hat{Q}_i^{p,n-1}\right)/\Delta t \\ + \left[\hat{E} - \hat{E}_v\right]_{j+1/2}^{p,n+1} - \left[\hat{E} - \hat{E}_v\right]_{j-1/2}^{p,n+1} \\ + \left[\hat{F} - \hat{F}_v\right]_{k+1/2}^{p,n+1} - \left[\hat{F} - \hat{F}_v\right]_{k-1/2}^{p,n+1} \\ + \left[\hat{G} - \hat{G}_v\right]_{l+1/2}^{p,n+1} - \left[\hat{G} - \hat{G}_v\right]_{l-1/2}^{p,n+1} \end{array} \right\} \tag{2.56}$$

Above equation is solved using zonal ILU decomposition technique.

## 2.5 Parallel implementation and scalability

The domain decomposition for parallelization follows the native structured block in the grid, where Z is total number of blocks. Therefore, number of parallel processes $P \leq Z$. The domain decomposition thus assigns integer number of blocks to each processor. METIS library (Karypis and Kumar, 1998) is used to obtain optimal domain decomposition. The global map of the zone assignment to specified number of processes is maintained at all the time and appropriate buffers are initialized based on inter-block connectivity table. Standard MPI library is used for inter-processor communication Gropp and Lusk (1999). The latency between message passing may be minimized by using uniform block size as much possible. Every iteration the inter-block data is exchanged.

Experiences of using this code upto 800 processors on quadcore Xeon clusters (of queenbee, LONI) using infiband communications confirm the scalability of this code upto a large number of processors (Table 7.1).

Table 2.1: Computational time for different number of processors in Queenbee

| Grid size (blocks) | processors | No.of Iterations | Computational time | Computational time ($s$) for single iteration /processor/cell |
|---|---|---|---|---|
| 3.1 M cells (2088) | 320 | 9200 | 48 | $1.893 \times 10^{-8}$ |
| 4.2 M cells (3552) | 320 | 5760 | 48 | $2.323 \times 10^{-8}$ |
| 4.2 M cells (3552) | 800 | 12820 | 48 | $3.76 \times 10^{-9}$ |

Figure 2.1 shows the parallel scalability of CHEM3D.

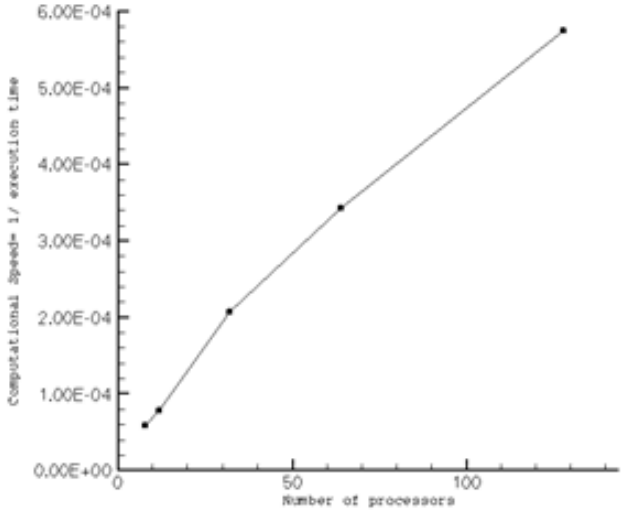


Figure 2.1: Parallel scale up for Chem3D

## 2.6 Large eddy simulation

The idea of large eddy simulation exploits the proposition that the smaller scale turbulence is universal in nature and can adequately represented by modeling compared to large scale energetic eddies that are anisotropic and non-homogeneous in nature. In the energy cascade process in turbulence the large scale flow structures extracts the turbulent kinetic energy from the mean flow and pass it on to the smaller scales and hence dictates the global dissipation

levels. The anisotropic and nonhomogeneous nature requires the large scale structures to be resolved in order to represent accurately. The role of subgrid scale model (SGS) is to mimic the energy transfer from larger scales to smaller scales accurately by adding appropriate eddy viscosity in the flow field. The smaller scales of the fluid motions are separated from the larger scales through filtering operation. A filtered variable is a quantity with larger scales resolved and smaller scales filtered out. The definition of a filtering operation is as introduced by Leonard (1974).

$$\bar{f}(x) = \int_D f(x')G(x, x'; \bar{\Delta})dx' \tag{2.57}$$

where $D$ is the complete domain, $f(x')$ is a test function. $G$ is a filter function, $\bar{\Delta}$ is filter width. The size of the largest scale resolved depends upon the size of the filter. Any scales less than the filter width are typically filtered out. Figure 2.2 shows the effect of filter width on the small scales (Piomelli et al.).

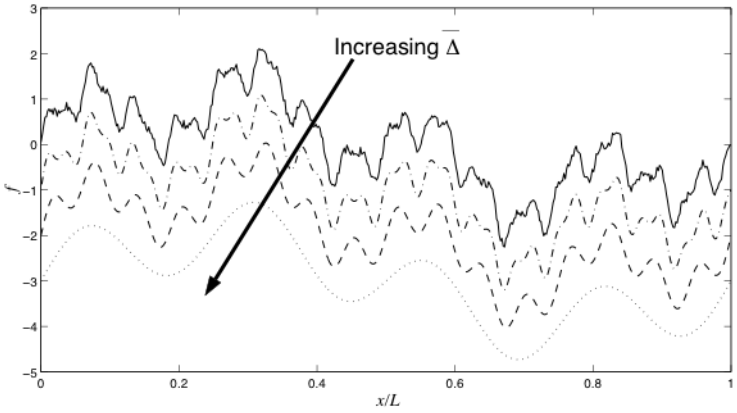


Figure 2.2: Effect of filter width in a test function

In the present implementation a top-hat or box filter is used for filtering operation,

$$G(x) = \begin{cases} 1/\bar{\Delta} & \text{if x} \leq \bar{\Delta}/2 \\ 0 & \text{elsewhere} \end{cases} \tag{2.58}$$

The box filters are has unique mean value and commuting property with differentiation operation when the filter width is uniform. Two types of modeling approaches exists to represent smaller scales in large eddy simulation by eddy viscosity approach: (i) Functional modeling based on kinetic energy transfer and (ii) structural modeling based on accurate reproduction eigenvectors of statistical correlation tensors.

### 2.6.1 Large eddy simulation on curvilinear grids

In order to simulate turbulent flows using large eddy simulation in complex topologies the SGS model must be formulated in curvilinear coordinate system. When grid size is used as filetr width, the spatial filtering of N-S equations leads to the commutation errors owing to non-uniform grid filter width (Tyagi and Acharya, 2005). There exist two filtering approaches of this formulation (i) Governing equations are transformed from curvilinear co-ordinate system and then the filtering operation is performed (Jordan, 2001). (ii) The equations are spatially filtered then transformed to computational domain (Tafti, 2005). In the present implementation is based on the second approach. The filtered continuity and momentum equation in the conservative form are given as,

$$\frac{\partial\left(\sqrt{g}\bar{U}^{j}\right)}{\partial x_i} = 0 \tag{2.59}$$

$$\frac{\partial\left(\sqrt{g}\bar{u}_i\right)}{\partial t} + \frac{\partial\left(\sqrt{g}\bar{U}^{j}\bar{u}_i\right)}{\partial \xi_j} = -\frac{\partial\left(\sqrt{g}\left(\vec{a}^{j}\right)_i\bar{u}_i\right)}{\partial \xi_j} + \frac{\partial}{\partial \xi_j}\left(\left(\frac{1}{Re}+\frac{1}{Re_t}\right)\sqrt{g}g^{jk}\frac{\partial \bar{u}_i}{\partial \xi_k}\right) \tag{2.60}$$

where $\sqrt{g}$ is Jacobian of transformation $\sqrt{g}U_j = \sqrt{g}\left(\vec{a}^{j}\right)_k u_k$ is covariant flux vector, and $g^{ij}$ are the elements of contravariant metric tensor. Eddy viscosity at each time step is dynamically calculated using Smagorinsky sub-grid scale model (Sagaut, 2001; Tyagi and Acharya, 2005).

$$\frac{1}{Re_t} = C_s^2 \left(\sqrt{g}\right)^{2/3} \left|\bar{S}\right| \tag{2.61}$$

where, $|S|$ is magnitude of the strain rate tensor given by,

$$\bar{S}_{ik} = \frac{1}{2}\left( \left(a^m\right)_k \frac{\partial \bar{u}_i}{\partial \xi_m} + \left(a^m\right)_i \frac{\partial \bar{u}_k}{\partial \xi_m} \right) \tag{2.62}$$

In the above equations an over bar represents the grid filtered quantity. Test filtered quantities are obtained by second order trapezoidal filter,

$$\bar{\phi} = \frac{1}{4}\left(\bar{\phi}_{i-1} + 2\bar{\phi}_i + \bar{\phi}_{i+1}\right) \tag{2.63}$$

The anisotropic sub-grid $(-)$ and subtest scale $(\sim)$ stress tensor is formulated by Smagorinsky eddy viscosity model (Smagorinsky 1963),

$$\tilde{\tau}_{ij}^a = -2C_s^2 \left(\sqrt{g}\right)^{2/3} \widetilde{\left|\bar{S}\right| \bar{S}_{ij}} \tag{2.64}$$

$$T_{ij}^a = -2C_s^2 \alpha \left(\sqrt{g}\right)^{2/3} \left| \tilde{\bar{S}} \right| \tilde{\bar{S}}_{ij} \tag{2.65}$$

$C_s$ is the model coefficient assumed at sub-grid and subtest level. $\alpha$ is square of the ratio of length scales of test filter to the grid filter taken as $\tilde{\bar{\Delta}}/\bar{\Delta} = \sqrt{6}$. The Germano identity relates the sub-grid scale stresses at different filter levels (Germano, Piomelli et al. 1991),

$$T_{ij} = \widetilde{\overline{u_i u_j}} - \tilde{\bar{u}}_i \tilde{\bar{u}}_j = \overline{u_i u_j} - \bar{u}_i \bar{u}_j \tag{2.66}$$

$$L_{ij} = T_{ij} - \tau_{ij} = \widetilde{\overline{u_i u_j}} - \tilde{\bar{u}}_i \tilde{\bar{u}}_j \tag{2.67}$$

where $L_{ij}$ is Leonard stress is the difference between sub-test and sub-grid stress terms. Using Smagorinskys model for subgrid scale stress terms, the Germano identity relates the

anisotropic components of Leonard stress with the strain rate tensor as,

$$L_{ij}^{a} = L_{ij} - \frac{1}{3}\delta_{ij}L_{kk} = -2C_s^2\left(\sqrt{g}\right)^{2/3}\left(\alpha\left|\tilde{\bar{S}}\right|\tilde{\bar{S}}_{ij} - \widetilde{\left|\bar{S}\right|\bar{S}_{ij}}\right) \tag{2.68}$$

$$L_{ij}^{a} = L_{ij} - \frac{1}{3}\delta_{ij}L_{kk} = -2C_s^2 M_{ij} \tag{2.69}$$

The Smagorinsky model constant is dynamically evaluated by,

$$C_s^2 = -\frac{1}{2}\frac{1}{\left(\sqrt{g}\right)^{2/3}}\frac{L_{ij}^{a}\cdot M_{ij}}{M_{ij}\cdot M_{ij}} \tag{2.70}$$

The negative value of $C_s$ can be physically interpreted as backscattering, which accounts for transfer of energy from smaller modeled scale to larger resolved scales. From numerical point of view allowance of backscattering lead to numerical instability, hence $C_s$ is restricted to positive values and smoothed over neighboring computational cells to avoid sharp spatial fluctuations (Tyagi and Acharya, 2005).

## 2.7 Ensemble vs time average

The motivation for ensemble average comes from the fact that a generic turbulent flow is not statistically stationary. Under such circumstances the idea of time average looses the physical meaning and therefore not appropriate.This issue is resolved by computing the average of large number ($N$) of flow field realizations at identical time instant. Ensemble average is defined, in the limit $N \to \infty$, as,

$$\langle u(x,t)\rangle \equiv \frac{1}{N}\sum_{i=1}^{N} u^i(x,t) \tag{2.71}$$

where, $[u^i(x,t)]_{i=1}^{N}$ is sequence of realizations of velocity field $u(x,t)$. The necessity of large number of realizations ($N \to \infty$) at identical instant of time makes ensemble averages extremely difficult to compute in experiments or simulations of turbulent flows. Also there

is no generic consensus on how large $N$ should be for the statistical convergence. However, time average is routines used in turbulence research to evaluate the statistical moments of variables by invoking the 'Ergodicity hypothesis'. It states "A dynamical process is called 'ergodic' when averages of all the evolutionary variables converge" (Tennekes and Lumley, 1983). Therefore, for an ergodic process the time average are the ensemble average for sufficiently large time signal. The ergodicity hypothesis is typically invoked in case of periodic flows, where the mean computed from periodic signal converges statistically stationary value for a large enough signal.

In the present study, ergodicity hypothesis is invoked for the turbulent flow field under consideration. Therefore, time average method is used to compute all the statistical moments of the variable of interest,

$$\bar{u}(x) \equiv \lim_{T\to\infty} \frac{1}{T} \int_0^T u(x,t)dt \tag{2.72}$$

## 2.8 Bench mark validation -Turbulent flow over backward facing step

The implementation of large eddy simulation is verified by testing a benchmark case of flow over backward facing step for Reynolds number $Re = 5100$ (Jovic and Driver). The geometry consists of a channel with a sudden expansion with expansion ratio of 1.2 as shown schematically in Figure 2.3. The sudden expansion forms a dump plane (step) upon which the incoming boundary layer separates forming a recirculation bubble behind the step. The past the recirculation bubble is reattached and streamwise developing boundary layer is formed. Jovic and Driver measured the time averaged length of recirculation bubble, streamwise velocity and Reynolds stress profiles at certain measurement locations. Le et al. (1997) performed DNS simulation with domain size of $30H$ in streamwise, $4H$ in spanwise $6H$ in lateral direction (Le et al., 1997) maintaining the same expansion ratio of 1.2. They used 9.5 Million grid points for the DNS simulation.

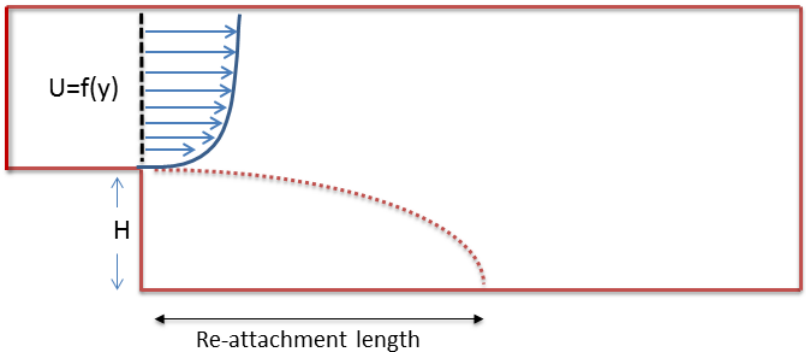


Figure 2.3: Schematic of domain

In the present case, block structured grid consisting of1.5 Million grid points and 300 uniform blocks was used for LES simulation. The inlet boundary condition was applied at the step wall (shown in Figure 2.3) and wall upstream of the step was not modeled. The inlet mean boundary layer profile was closely matched the experimentally reported profile by Jovic and Driver using $1/5^{th}$ power law profile shown in Figure 2.4. No information of boundary layer turbulence was provided at the inlet.

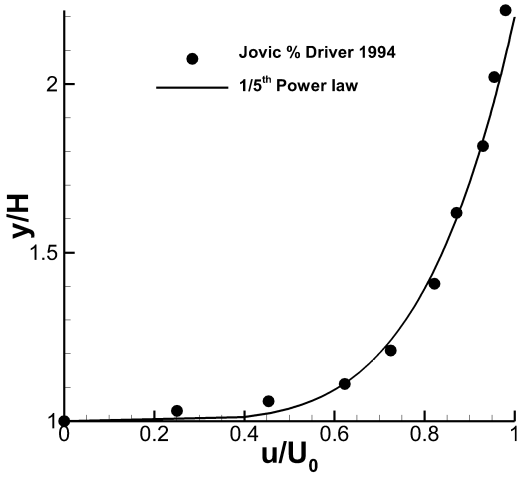


Figure 2.4: Inlet boundary layer profile at $x/H = 0$

The top boundary of the domain was treated as impenetrable no-stress wall,.

$$v = 0 \frac{\partial u}{\partial y} = \frac{\partial w}{\partial y} = 0 \tag{2.73}$$

The spanwise boundaries were applied treated with periodic boundary condition assuming the statistically homogeneous flow. The outlet boundary is treated as non-reflecting/convective boundary with,

$$\frac{\partial u_i}{\partial t} + U_c \frac{\partial u_i}{\partial x} = 0 \tag{2.74}$$

where $U_c$ is mean velocity at exit calculated based on total mass flow rate at the inlet also called as convection velocity. All other boundaries were treated as no-slip wall.

The simulation is carried out with a physical time step of $0.01s$. The turbulence statistics is collected for total of $600s$ amounting to 20 flow-through times based on streamwise length of the domain. Total of 160 CPUs for 72Hrs used for the computation in order to obtain statistically steady results. The results are compared with Jovic and Driver at measurement locations $x/H = 4.0, 6.0, 10.0$ and 19.0 for mean streamwise velocity, Reynolds stress profiles and flow reattachment length. The reattachment length in the present simulation is found to be $6.35H$ compared to 6.28 with (Le et al., 1997) and $6.0H$-$6.1H$ in (Jovic and Driver).

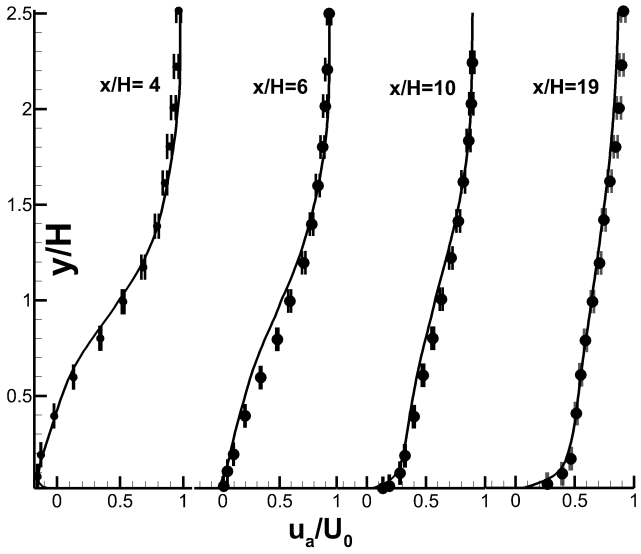


Figure 2.5: Comparison of mean streamwise velocity (− Simulation, • (Jovic and Driver))

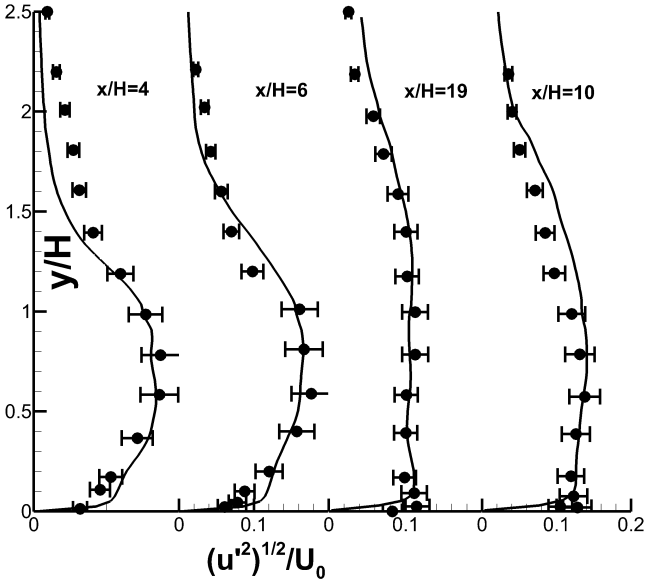


Figure 2.6: Streamwise normal Reynolds stress profile

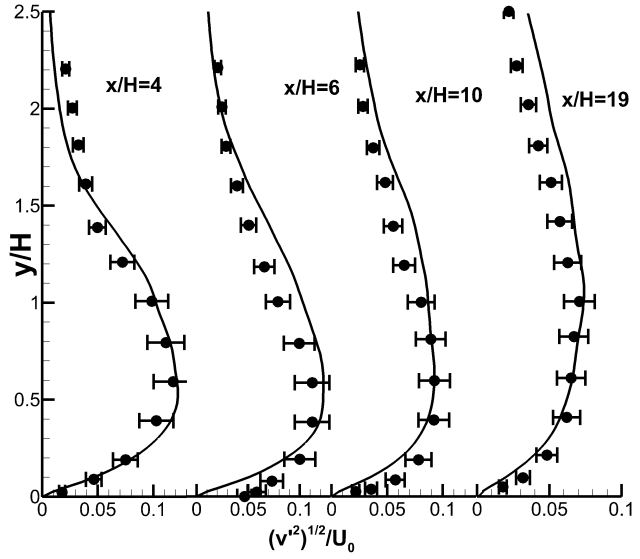


Figure 2.7: Wall nromal Reynolds stress profile

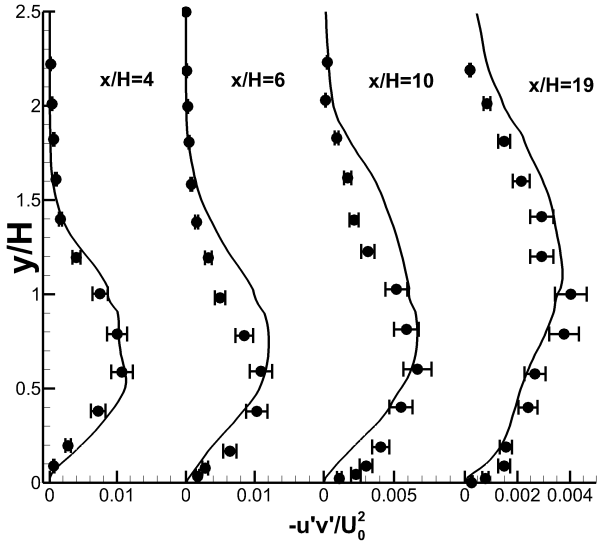


Figure 2.8: Cross stream Reynolds stress profile

Figure 2.5 through Figure 2.8 show the agreement between simulated and measured (Jovic and Driver) mean velocity and Reynolds stress profiles. The agreement in mean, normal and cross stream Reynolds stress show that the statistical characteristics of turbulence is accurately captured with present LES model, verifying the validity of implemented SGS model.

# Chapter 3
# Stability of Momentum Driven Planar Countercurrent Shear Flows in Dump Geometry

**Abstract**

A momentum driven countercurrent shear flow in a confined geometrical configuration is numerically studied using large eddy simulation (LES). The primary controlling parameter is the ratio of the primary jet to the counter (secondary) jet velocity or mass flow rates. A transition in the instability mode to a global mode is observed as mass ratio increases from 7.5% to 36%. The transition phenomenon is shown to be associated with change in secondary-jet behavior, and a significant increase in turbulence levels in the primary channel. The spectral records showed the spatial synchronization of the primary instability (Kelvin-Helmholtz) at the 36% mass ratio. The establishment of self-excited global mode was verified by three dimensional stability analysis using the dynamic mode decomposition (DMD) method. Both DMD and spectral records indicate that the increased mass ratio did not affect the time scale of primary instability but increased the growth rates leading to to the transition to the self-excited global mode. DMD analysis of the flow field at lower mass flow ratio cases showed decaying modes and convective modes in the flow.

### 3.1 Geometry and Flow conditions

A planar dump type of geometry 3.1 with inlet section consisting of a rectangular channel with $20mm$ height before the dump plane and a width of $160mm$. Lower wall of the channel is a splitter plate extending $100mm$ from inlet boundary in streamwise direction till dump plane, where it ends with a sharp edge. The counter flowing jet (secondary jet) is used as a control jet and has $2mm$ thickness and spans out $160mm$ for the entire width of the domain. The secondary jet assembly is placed $20mm$ downstream of the splitter plate edge (dump plane) with its centerline aligned parallel and $\delta = 5.2mm$ below the splitter plate. In the experimental investigation of Anderson (2011) it was observed that with higher $\delta$ values, interaction of secondary and primary jet is significantly reduced, and for smaller values, the stagnation point is formed well above the splitter plate in primary jet region, creating a major obstruction to the flow. At a specified value of 5.2mm, the formation of stagnation point is close to the splitter plate and the interaction is considered as optimal Anderson (2011). A streamwise distance of 20mm was allowed for shear layer to develop. The center of coordinate system was situated at the leading edge of the splitter plate with $x$ axis oriented in streamwise direction, $y$ axis oriented in cross-stream direction and $z$ axis in lateral direction.

Flow conditions at the inlet of primary and secondary streams were experimentally measured for mean velocity profile and turbulence. Inlet boundary layers had turbulence levels $\approx 10\%$ in the inlet boundary layers and less than $2-3\%$ in the bulk in the experimental facility (Anderson, 2011). Boundary conditions in the simulations are provided specified only with the mean flow profile and no inlet turbulence specified for the primary or secondary inlet flows. The jet Reynolds number of the primary stream based on the mean inlet flow velocity U1 is set at 14700. The amount of shear applied is controlled by the normalized velocity ratio $\lambda = (U_1 - U_2)/(U_1 + U_2)$ and $r = U_1/U_2$ where $U_2$ is the secondary (control) jet velocity. Velocity ratio is varied by adjusting the secondary jet velocity only and other flow conditions

and geometric parameters are held constant for different velocity ratios. Three simulations are conducted for 7.5%, 23% and 36% secondary jet mass flow rate with corresponding $r$ values of $-1.01$, $-0.32$ and $-0.21$ respectively. The solid boundaries of the domain including spanwise extreme boundaries are treated as no-slip walls. Bottom boundary of the domain and streamwise exit boundary are applied with non-reflecting outflow boundary to negate any perturbations to reflect back in the domain.

$$\frac{\partial u_i}{\partial t} + U_c \frac{\partial u_i}{\partial x_i} = 0 \tag{3.1}$$

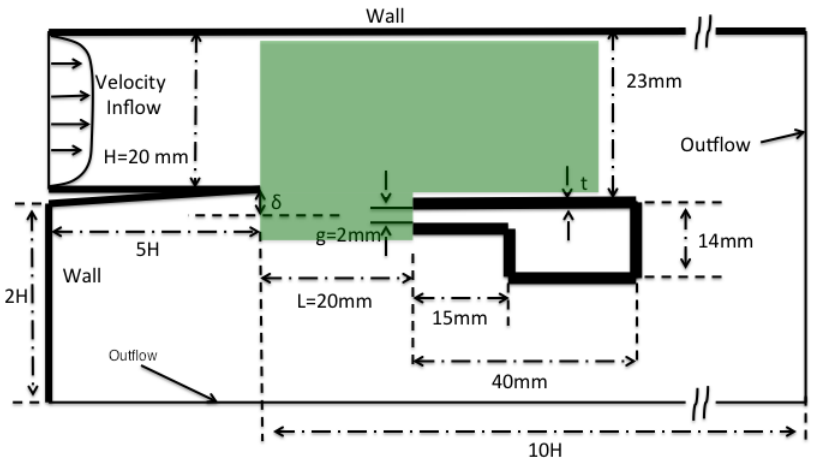


Figure 3.1: Schematic of countercurrent flow domain

A key objective of this study is to investigate the counter-current shear flow behavior, the region of interest to focus on for the analysis and presentation of results is the domain where the interaction of the primary and secondary streams are the strongest. Therefore the region of interest is extended $2.5H$ downstream from the edge of the splitter plate (dump plane); it will be shown in subsequent section that this region fully contains the mean recirculation bubble formed in the primary region and sufficient to capture the shear layer dynamics and mean recirculation bubble.

### 3.2 Numerical Method

The governing equations for incompressible viscous flow are given in non-dimensional form as,

$$\frac{\partial u_i}{\partial x_i} = 0 \tag{3.2}$$

$$\frac{\partial u_i}{\partial t} + \frac{\partial u_i u_j}{\partial x_j} = -\frac{\partial p}{\partial x_i} + \frac{1}{Re}\frac{\partial^2 u_i}{\partial x_j^2} \tag{3.3}$$

where $u_i$, $p$ and $Re$ are the velocity vector, pressure and Reynolds number respectively. The CFD code used for simulation was developed in-house and operates on block-structured grids in generalized curvilinear coordinate system to solve compressible flows. A low Mach number pre-conditioner was used to solve incompressible flow equations.

A Large Eddy Simulation (LES) approach is used to capture the dynamics in the flow and resolve the larger scales. The corresponding spatially filtered governing equations for mass and momentum for an incompressible flow in curvilinear coordinates are given as,

$$\frac{\partial \left(\sqrt{g}\bar{U}^j\right)}{\partial x_i} = 0 \tag{3.4}$$

$$\frac{\partial \left(\sqrt{g}\bar{u}_i\right)}{\partial t} + \frac{\partial \left(\sqrt{g}\bar{U}^j\bar{u}_i\right)}{\partial \xi_j} = -\frac{\partial \left(\sqrt{g}\left(\vec{a}^j\right)_i\bar{u}_i\right)}{\partial \xi_j} + \frac{\partial}{\partial \xi_j}\left(\left(\frac{1}{Re} + \frac{1}{Re_t}\right)\sqrt{g}g^{jk}\frac{\partial \bar{u}_i}{\partial \xi_k}\right) \tag{3.5}$$

where $\sqrt{g}$ is Jacobian of transformation $\sqrt{g}U_j = \sqrt{g}\left(\vec{a}^j\right)_k u_k$ is covariant flux vector, and $g^{ij}$ are the elements of contravariant metric tensor. Eddy viscosity at each time step is dynamically calculated using Smagorinsky sub-grid scale model (Sagaut, 2001; Tyagi and Acharya, 2005).

$$\frac{1}{Re_t} = C_s^2\left(\sqrt{g}\right)^{2/3}\left|\bar{S}\right| \tag{3.6}$$

where, $|S|$ is magnitude of the strain rate tensor given by,

$$\bar{S}_{ik} = \frac{1}{2}\left( (a^m)_k \frac{\partial \bar{u}_i}{\partial \xi_m} + (a^m)_i \frac{\partial \bar{u}_k}{\partial \xi_m} \right) \tag{3.7}$$

In the above equations an over bar represents the grid filtered quantity. Test filtered quantities are obtained by second order trapezoidal filter,

$$\bar{\phi} = \frac{1}{4}\left( \bar{\phi}_{i-1} + 2\bar{\phi}_i + \bar{\phi}_{i+1} \right) \tag{3.8}$$

The anisotropic sub-grid $(-)$ and subtest scale $(\sim)$ stress tensor is formulated by Smagorinsky eddy viscosity model (Smagorinsky 1963),

$$\tilde{\tau}^a_{ij} = -2C_s^2 \left(\sqrt{g}\right)^{2/3} \widetilde{\left|\bar{S}\right| \bar{S}_{ij}} \tag{3.9}$$

$$T^a_{ij} = -2C_s^2 \alpha \left(\sqrt{g}\right)^{2/3} \left| \tilde{\bar{S}} \right| \tilde{\bar{S}}_{ij} \tag{3.10}$$

$C_s$ is the model coefficient assumed at sub-grid and subtest level. $\alpha$ is square of the ratio of length scales of test filter to the grid filter taken as $\tilde{\bar{\Delta}}/\bar{\Delta} = \sqrt{6}$. The Germano identity relates the sub-grid scale stresses at different filter levels (Germano et al., 1991),

$$T_{ij} = \widetilde{\overline{u_i u_j}} - \tilde{\bar{u}}_i \tilde{\bar{u}}_j = \overline{u_i u_j} - \bar{u}_i \bar{u}_j \tag{3.11}$$

$$L_{ij} = T_{ij} - \tau_{ij} = \widetilde{\overline{u_i u_j}} - \tilde{\bar{u}}_i \tilde{\bar{u}}_j \tag{3.12}$$

where $L_{ij}$ is Leonard stress is the difference between sub-test and sub-grid stress terms. Using Smagorinskys model for subgrid scale stress terms, the Germano identity relates the anisotropic components of Leonard stress with the strain rate tensor as,

$$L^a_{ij} = L_{ij} - \frac{1}{3}\delta_{ij} L_{kk} = -2C_s^2 \left(\sqrt{g}\right)^{2/3} \left( \alpha \left| \tilde{\bar{S}} \right| \tilde{\bar{S}}_{ij} - \widetilde{\left|\bar{S}\right| \bar{S}_{ij}} \right) \tag{3.13}$$

$$L_{ij}^{a} = L_{ij} - \frac{1}{3}\delta_{ij}L_{kk} = -2C_s^2 M_{ij} \tag{3.14}$$

The Smagorinsky model constant is dynamically evaluated by,

$$C_s^2 = -\frac{1}{2}\frac{1}{\left(\sqrt{g}\right)^{2/3}}\frac{L_{ij}^{a}\cdot M_{ij}}{M_{ij}\cdot M_{ij}} \tag{3.15}$$

The negative value of $C_s$ can be physically interpreted as backscattering, which accounts for transfer of energy from smaller modeled scale to larger resolved scales. From numerical point of view allowance of backscattering lead to numerical instability, hence $C_s$ is restricted to positive values and smoothed over neighboring computational cells to avoid sharp spatial fluctuations (Tyagi and Acharya, 2005).

A block-structured body fitted grid is used to discretize the domain. Total of 1376 blocks were used. The grid size was selected based on a grid independent study that utilized three different grid levels, 2.5 Million (M), 4.5M and 8M mesh points . The 23% case was simulated on all three grids. The mean velocity profile at the bubble centerline for all the three grids was were compared for mesh independence and validated against experimentally measured velocity profile, and are shown in Figure 5.2.

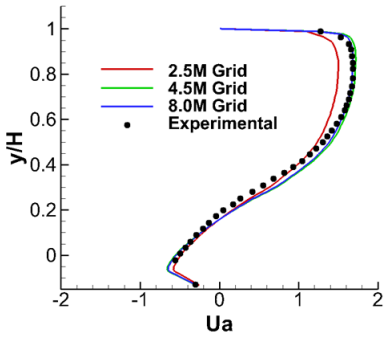


Figure 3.2: Grid Independence (23% case)

It can be seen that the mean velocity profile did not change significantly from 4.5M to 8M grid points . The mean velocity profile obtained on 4.5 and 8M grid also compared well with experimentally measured velocity profile (Anderson, 2011); hence the 4.5 M grid

was chosen for the final simulation. Also, the energy spectrum (at $x/H = 1.5$, $y/H = 0.5$) shown in Figure 3.3 for the 23% and 36% mass ratio case compared well with experimentally obtained spectra and follows the Kolmogorovs -5/3 law in inertial subrange.

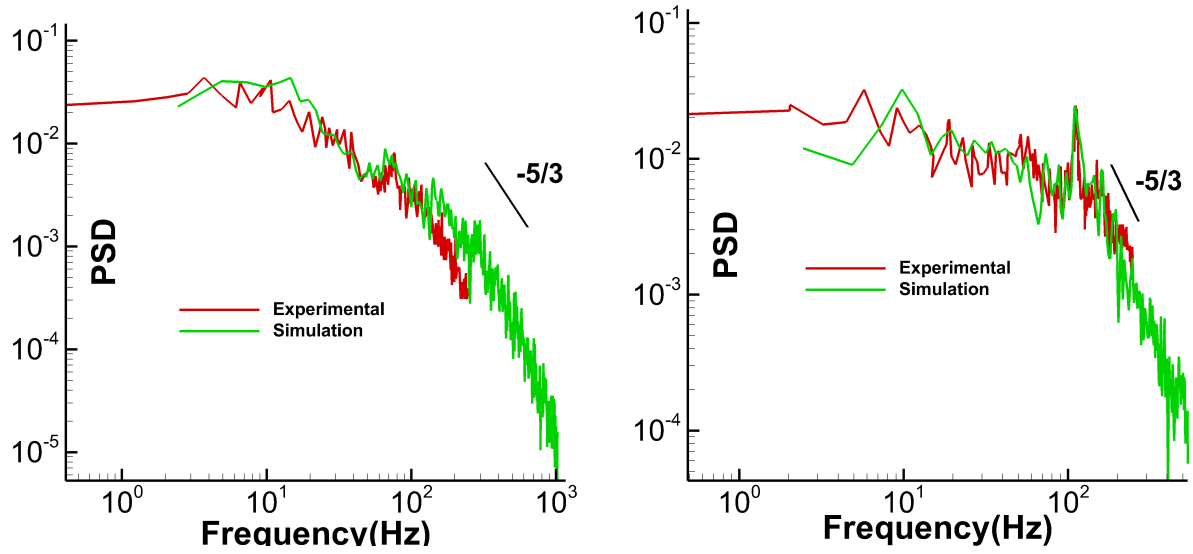


(a) 23% (b) 36%

Figure 3.3: Comparison of energy spectra with experiments

### 3.3 Results and Discussion

In this section we present the results for the three cases with 7.5%, 23% and 36% mass flow rate. In section 3.3.1, the mean flow characteristics results of for the 23% and 36% cases are compared with measured data (Anderson 2011). The 23% mass ratio represent the case before transition to global instability while for the 36% mass ratio case the flow is globally unstable. Investigation of the dynamical characteristics and transition to global mode presented in section 4.2, while analysis using the dynamic mode decomposition technique is discussed in section 4.3.

### 3.3.1 Mean flow characteristics

The experimental investigation for the 23% and 36% cases was were conducted by Anderson (2011). They measured the mean flow and turbulence characteristics on spanwise mid-plane using particle image velocimetry (PIV) technique. The velocity time signal was collected for spectral analysis using a hot wire at a location $x/H = 1.5$ and $y/H = 0.5$. An identical geometrical configuration was used in the present work and results obtained using LES. The time statistics are collected after 20 flow through times to allow the initial transients to wash away. All spatial dimensions are normalized with the channel height $H$. Mass averaged inlet velocity is used to normalize velocity and total turbulence.

In all the cases, the mean flow re-attaches within a distance of $2.5H$ from the edge of the splitter plate and the recirculation bubble is contained within the region of interest; therefore, the important dynamical features of secondary and primary jet interaction are captured in this region. In all the figures below, the region of interest (identified by the green shading in 3.1 ranges from the edge of the splitter plate $x/H = y/H = 0$ to 2.5 and $y/H = -1$ to1, spanning the entire primary channel region and the region below the secondary jet.

For the 7.5% mass ratio case results of simulations are presented and experimental data is not available. Mean velocity field and turbulence in Figure 3.4 shows negligible effect of counter flow in terms of mean flow acceleration is observed. In the shear layer between the primary and secondary jet two recirculation bubbles are formed with a stagnation point in between. A third recirculation bubble formed below the shear layer is due to the entrainment by the secondary jet from the region below. Normalized RMS velocity contours based are shown in Figure 3.4b. Higher turbulence levels are seen in the shear layer region and along the upper wall and marginal increase in turbulence levels observed in central region of primary jet.

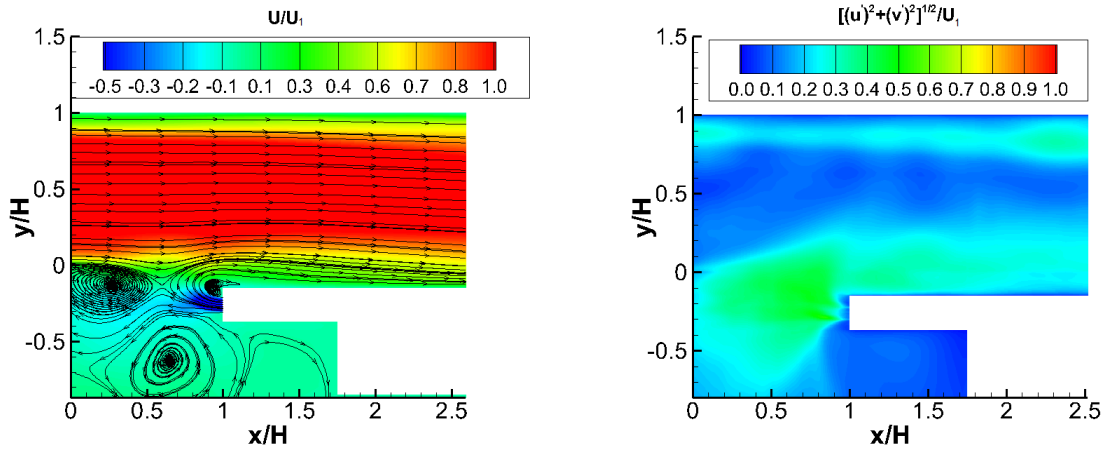


(a) (b)

Figure 3.4: Mean velocity field and turbulence field for 7.5% case

For 23% case simulation, Figure 3.5 shows the comparison between the predicted and measured mean streamwise velocity. A reasonable agreement is found between the measured and predicted velocity field. As the secondary jet velocity is increased ($U_1/U_2 = -0.32$), the mean behavior of the shear layer is altered significantly. The stagnation point is pushed closer to splitter plate and the recirculation bubble at the splitter plate end (observed in 7.5% case) is vanished. Increased shear magnitude $\propto |U_1 - U_2|$ causes roll up of secondary jet and a larger recirculation bubble is formed in the main jet region. The primary jet is accelerated due to the presence of recirculation bubble and maximum mean velocities increased by $\approx 50\%$ of primary jet velocity. The size of the recirculation bubble in simulation is found to be $0.522H$ $(10.44mm)$ in height, which compares well with the measured value of $0.52H$ $(10.4mm)$. The streamwise location of center of the recirculation bubble is found at $x/H = 1.0$ that matches the experimentally reported value. Figure 3.9a shows excellent agreement between mean velocity profile at the center of recirculation bubble from simulation and experiments.

The normalized RMS velocity contours, based on cross stream and streamwise velocity components, is compared with measurements (Figure 3.6). A marked increase in turbulence levels ($> 100\%$) in the shear layer in and above the stagnation region and secondary jet is observed. The over all in excess of 30% increase in turbulence levels in primary jet region

is observed. Figure 3.10 shows the agreement between measured and predicted cross-stream averaged turbulence levels for 23% case. The contribution of spanwise RMS component to cross stream averaged turbulence is found to be $\approx 10\% - 15\%$ indicating the increased three dimensionality of the flow field.

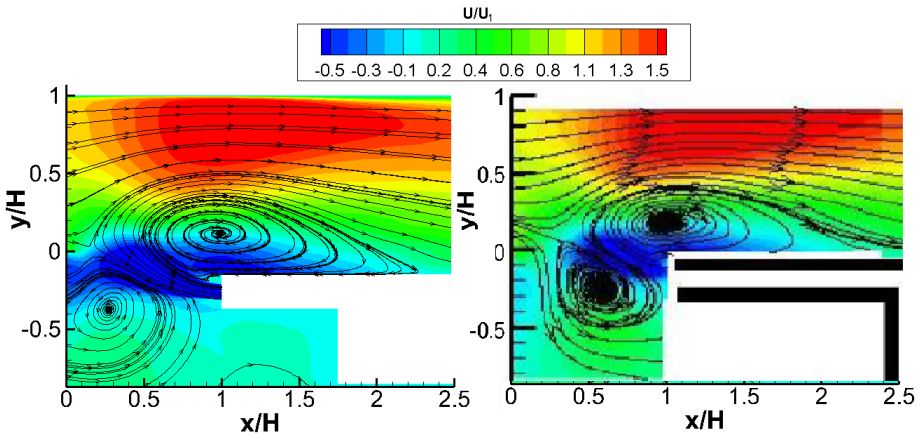


Figure 3.5: Mean velocity field comparison (23% case)

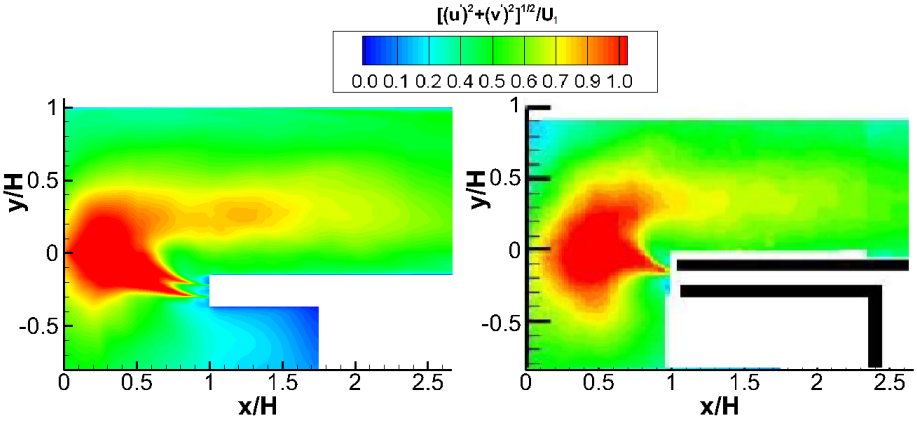


Figure 3.6: Turbulence comparison (23% case)

For case of 36% mass flow rate case, mean velocity field (Figure 3.7) show a similar behavior to 23% case. Due to increased secondary jet velocity ($U_1/U_2 = -0.21$) the stagnation point moves very close to splitter plate tip. The accelerated mean flow increased streamwise velocity peak levels by more than 100% in the region between recirculation bubble and upper wall. The height of the recirculation bubble increased by about 18% to $0.617H$ ($0.61H$

reported experimentally). The streamwise length did not alter compared to 23% case. The center of the recirculation bubble is found to be at 0.87H and compares well with measured value of $0.85H$. The agreement between the measured and predicted bubble centerline streamwise velocity profile is found to be excellent (Figure 3.9b)

Turbulence levels for 36% shown in Figure 3.8 are increased in excess of 100% over large part of primary jet region unlike 23% case where only the jet interaction region witnessed higher turbulence levels. Cross-stream averaged turbulence quantities show higher degree of three dimensionality of the flow field with $\approx 20\%$ contribution of spanwise RMS velocity to total turbulence over entire region of interest.

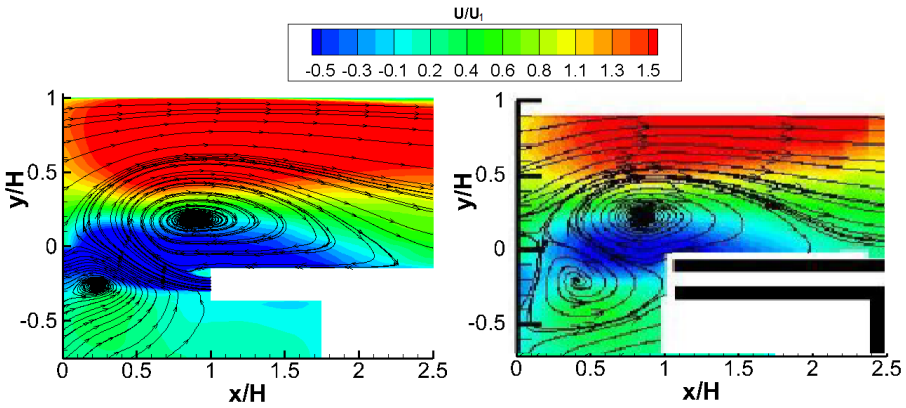


Figure 3.7: Mean velocity field comparison (36% case)

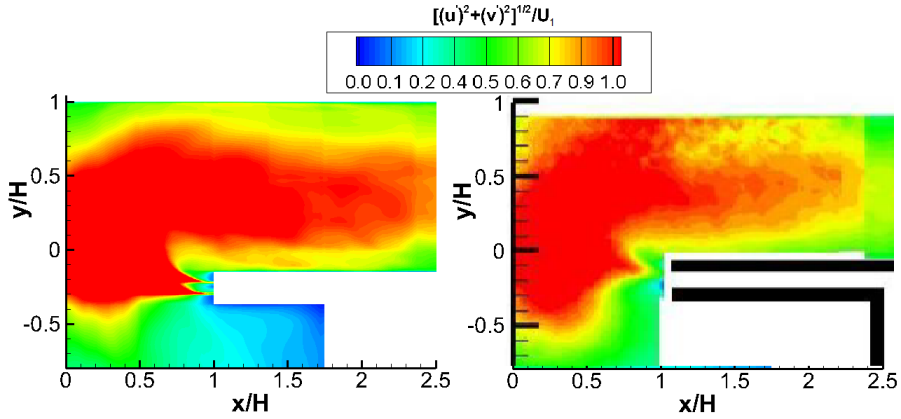


Figure 3.8: Turbulence comparison (36% case)

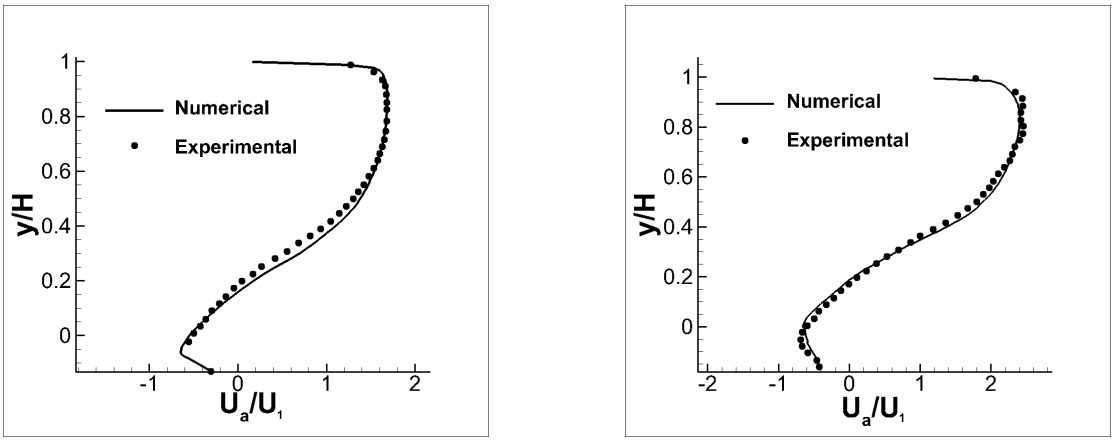


(a) 23% case (b) 36% case

Figure 3.9: Agreement between measured and predicted bubble centerline velocity profile

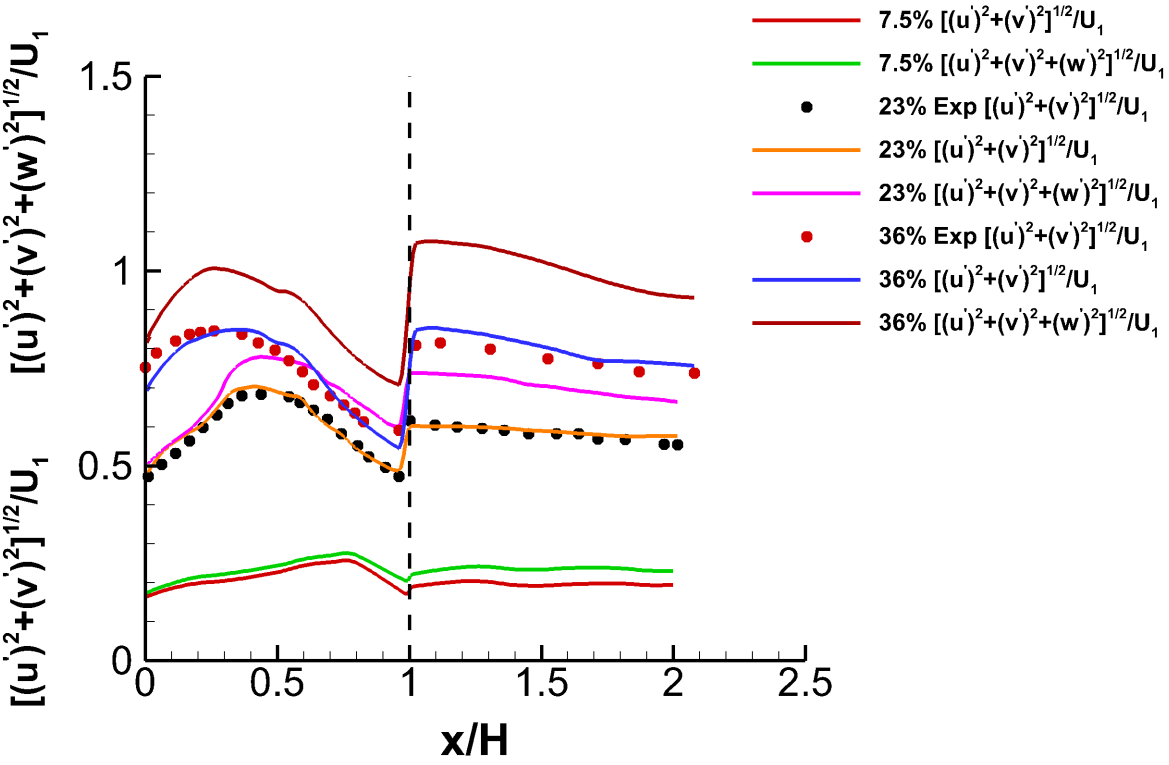


Figure 3.10: Cross-stream averaged turbulence for all mass ratios

In a nutshell, the mean flow and turbulence characteristics of primary jet were significantly influenced as the secondary jet velocity was increased. Two transition like phenomenon were observed, (*i*) appearance of a primary recirculation bubble as secondary jet

velocity was increased and significant increase in local turbulence levels, ($ii$) drastic increase in turbulence levels throughout the primary channel region and beyond recirculation bubble / shear layer. Such a drastic increase in turbulence levels is a typical indication of fundamental change in shear layer dynamics and possible on-set of self-excited oscillations that will be explored further in this paper.

### 3.3.2 Shear layer dynamics

The fundamental idea behind the momentum driven countercurrent shear was to create spatially developing shear layer with two parallel streams of primary and secondary jets. The mean velocity contours and streamlines indicate the complete rollup of the secondary jet and formation of the recirculation region in the primary channel. The oscillatory nature of the secondary jet (discussed in section 4.2.1) along with rollup, periodically switches the nature of entire upper shear layer between counter-flowing and co-flowing shear layers. Therefore, there exists no region in the shear layer that remains in countercurrent configuration at all the times. We observe that the shear layer remains in countercurrent configuration for a certain time and the rapid growth of shear layer vortices having pressure minima at the center pulls the jet, and eventually rolling up completely in the primary channel region. This will be shown in subsequent section for all mass ratio cases. With use of spectral information, complete three dimensional stability analysis and flow visualization, an attempt is made to understand the dynamical behavior for shear layers.

#### 3.3.2.1 Preliminary observations and spectral analysis

In order to characterize the shear layer formed by primary and secondary jet, time signal of streamwise velocity was collected at $x/H = 0.075, 0.15$ and $0.30$ and $y/H = 0.04$, a location in immediate downstream of splitter plate, shown in Figure 3.11a schematically. The time series data is collected for $4.1s$ of physical time after the initial transients are allowed to wash away with about(takes about 20 flow-through times).The collection of time signal data

collected thus constitutes nearly 82000 time steps, and a Fourier analysis is performed by segmenting the velocity signal in 6 blocks of 12288 data points each and taking the average in the frequency domain to minimize the variance. The resulting power spectral distribution in at all aforementioned locations is shown in Figure 3.11b. A typical time series signal of streamwise velocity at $x/H = 0.075$ and $y/H = 0.04$ is shown for all three mass ratios in Figure 3.11c; note the identical scale for streamwise velocity.

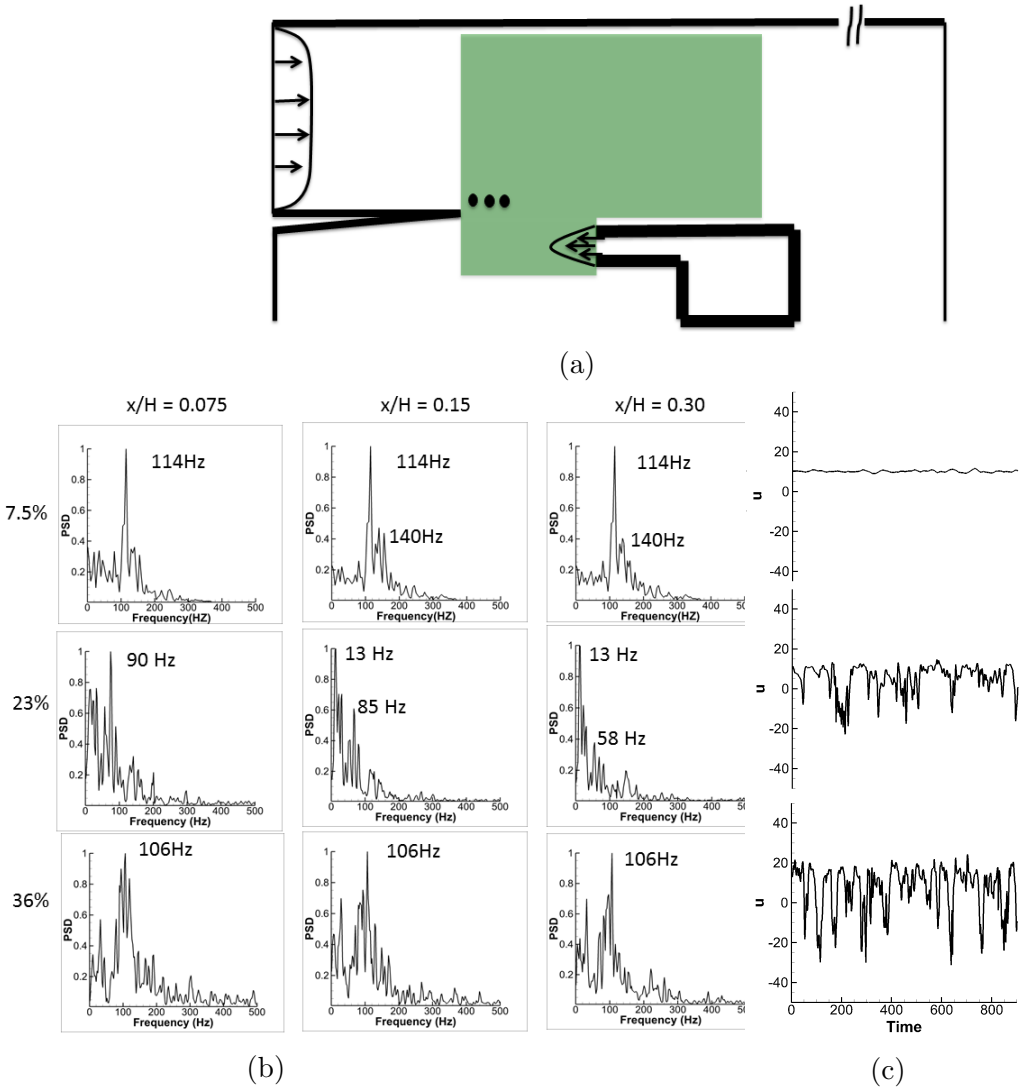


Figure 3.11: ($a$) Location of streamwise velocity spectra, ($b$) Spectra of streamwise velocity component, ($c$) Velocity signal at $x/H = 0.075$ for three different mass ratio

Additional time series data is probed in spanwise direction at $z/H = \pm 1$ from the

spanwise mid-plane and in the downstream neighborhood of splitter plate $x/H = 0.075$ and $y/H = 0.04$. For all three mass ratios the the frequency spectrum is obtained similar to the spectrum obtained at the spanwise mid-plane at identical streamwise and cross-stream location reported in Figure 3.11. The representative spectra at $x/H = 0.075$, $y/H = 0.04$ and $z/H = -1.0$ is shown in Figure 3.12. The peak frequency found for all mass ratio compares with corresponding spanwise mid-section data indicating that the time scales of flow oscillations at the splitter plate tip are largely uniform in spanwise direction.

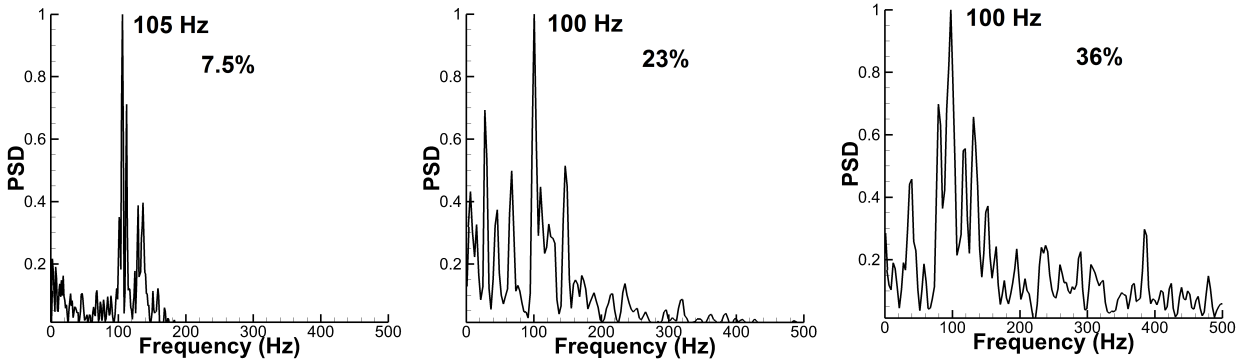


Figure 3.12: Spanwise spectra at $x/H = 0.075$, $y/H = 0.04$ and $z/H = -1.0$ for all mass ratios

For 7.5% case, the streamwise velocity power spectrum show a sharp peak at $114Hz$ with two nominal peaks at $140Hz$ for $x/H = 0.15$ and $x/H = 0.3$. A single peak of the velocity power spectra is indicative of a highly periodic oscillations of streamwise velocity. However, the corresponding velocity signal show low amplitude oscillations with no reversal in streamwise velocity component. The identification of the flow pattern corresponding to peak frequency is done by visualizing instantaneous velocity and vorticity contours over a frequency cycle of $114Hz$ on spanwise mid plane, shown in Figure 3.13. The splitter plate is marked with black/white line. The streamlines and vorticity indicated by arrow #1, show the roll up of vorticity from primary jet boundary layer at the splitter plate edge. The secondary jet is completely rolled up position (arrow #2) with a stagnation point between splitter plate and secondary jet. The growth of the vortex at the splittter plate edge pushes

the stagnation point towards the secondary jet, until the secondary jet is flipped below the growing vortex indicated by arrow #3. The flipping of secondary jet below the vortex forms a counter flowing streams across the clockwise rotating vortex and under the action of secondary jet, the center of the vortex is advanced towards the secondary jet (arrow #4) until it is directly on top of secondary jet. The pressure minima at the vortex core causes the secondary jet roll up in the primary jet and a new vortex begin to shed at the splitter plate edge indicated by arrow #6. The process of vortex shedding and jet rollup is observed to synchronized and periodic with frequency of $114Hz$. The vortex evolution and shedding is seen at the three query points hence the similarity in spectral response.

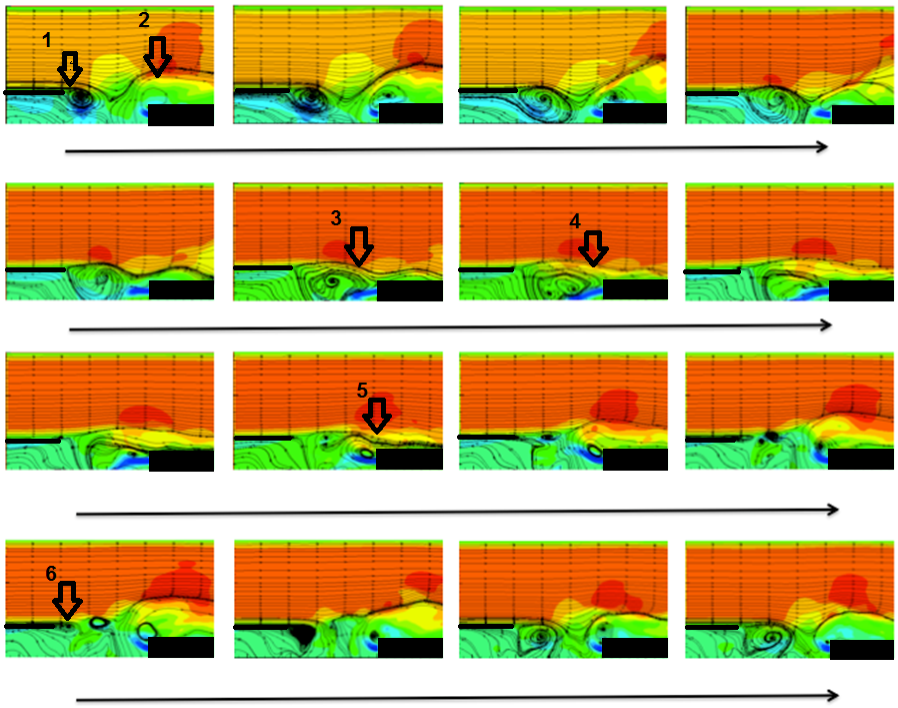


(a) Streamwise velocity contours

Figure 3.13: Velocity contours on spanwise mid plane (7.5% case)

Figure 3.14 shows instantaneous flow structures ($\lambda_2$ criterion Jeong and Hussain (1995)) visualized at a time during vortex shedding from splitter plate. The flow structures are colored with streamwise velocity contours. A greater degree of spanwise two-dimensionality of the vortex developing from the splitter plate is evident. However, the region over the

secondary jet assembly witness complex three dimensional flow with signatures of spanwise and streamwise vortices. However, these flow structures affect flow field only locally while rest of the flow in primary region remain relatively unperturbed as observed in mean flow characteristics.

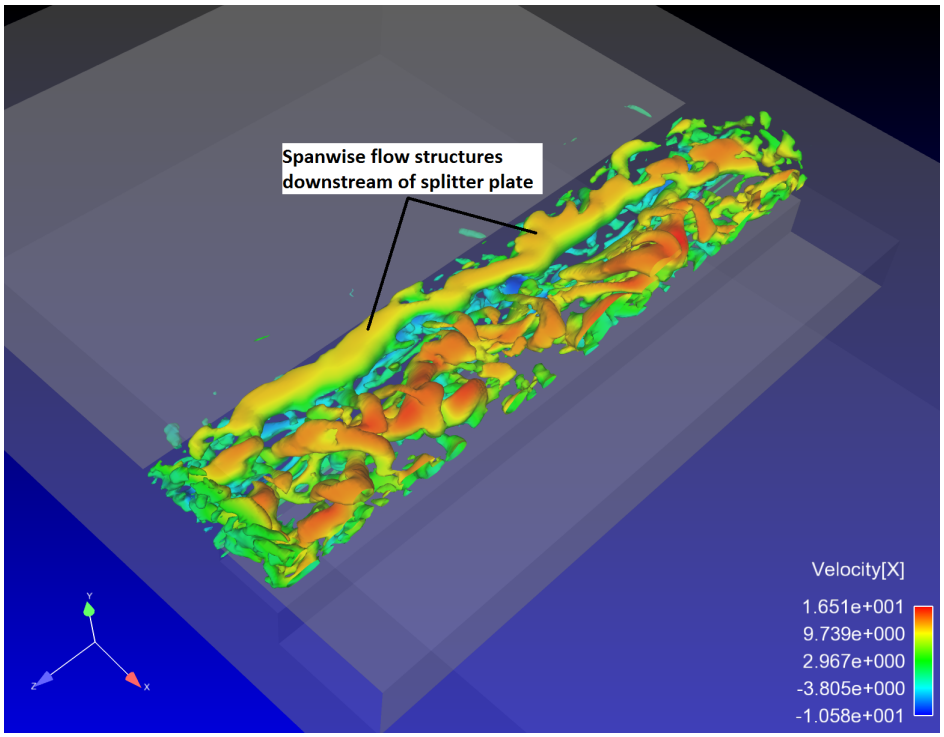


Figure 3.14: Instantaneous flow structure for 7.5% case

In 23% case, higher interaction of primary and secondary jet is observed in mean flow characteristics. The spectral response at $x/H = 0.075$ show a dominant frequency of $90Hz$ however, low frequency modes in the range of $10 - 20Hz$ are emerged. The trace of these low frequency modes are also seen at $x/H = 0.075$. At $x/H = 0.15$ the low frequency mode of $13Hz$ is amplified and emerges as dominant mode and dominant mode from previous location is attenuated and $85Hz$ secondary peak is observed. While dominant mode remains at $13Hz$ at $x/H = 0.3$ a weaker secondary mode is observed at $58Hz$. The spectral response at $x/H = 0.3$ is observed to be similar to spectral response at $x/H = 1.5$ and $y/H = 0.5$ in Figure 3.15 with a primary peak in the range of $10 - 20Hz$ and secondary peak at $65Hz$. The velocity signal at $x/H = 0.075$ shows stronger oscillations where streamwise velocity

fluctuates from $+10m/s$ to $-15/-20m/s$. The average velocity of the secondary jet for this case is about $22m/s$. The negative velocity peaks observed in the instantaneous velocity signal indicate the instantaneous presence of jet.

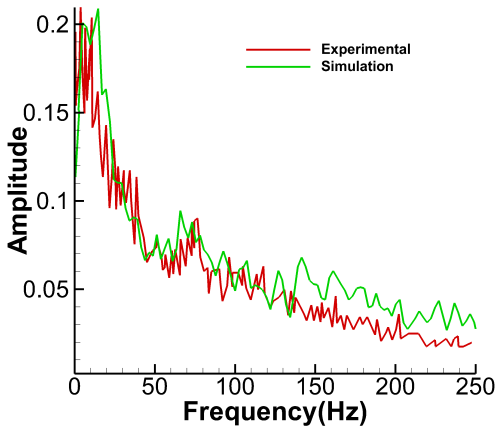


Figure 3.15: Velocity power spectra at $x/H = 1.5$ and $y/H$=0.5

For further investigations the streamwise velocity contours and streamlines are visualized in Figure 3.16, over a $20Hz$ frequency cycle. A $20Hz$ cycle is chosen since the dominant frequency at two streamwise locations down stream the splitter plate and at $x/H = 1.5$ and $y/H = 0.5$ (in the bulk of the flow) is found in the range of 10-20Hz. In the first instance, the secondary jet is rolled up completely in the primary channel and a large recirculation bubble is formed( indicated A-1 in Figure 3.16). The initiation of vortex shedding from boundary layer vorticity at the splitter plate edge is observed. In next instances, the center of recirculation bubble moves in streamwise direction and vortex at the splitter plate tip grows in size until a stagnation is formed at an instance indicated by A-4. The jet is then flipped downward and the recirculation bubble completely convects away establishing the channels flow at an instance indicated by B-3. The secondary jet and primary channel flow are observed to be anti-parallel at an instance (B-4), in the next instance the jet begin rolling upward due to counter shearing flow and vortex initiation directly above the secondary jet. This mechanism is very similar to 7.5% case however, in the present case the secondary jet penetrates more towards splitter plate and jet roll up results in much larger recirculation bubble and

causes flow oscillations over entire channel. It should be noted that this mechanism does not follow a strict periodicity,owing to multiple modes (frequency peaks) simultaneously and resembles a strange attractor reported in Bradstater and Swinney (1987). The details of three dimensionality of the flow field and large scale structures will be discussed later to provide a perspective of the flow field at higher velocity ratios.

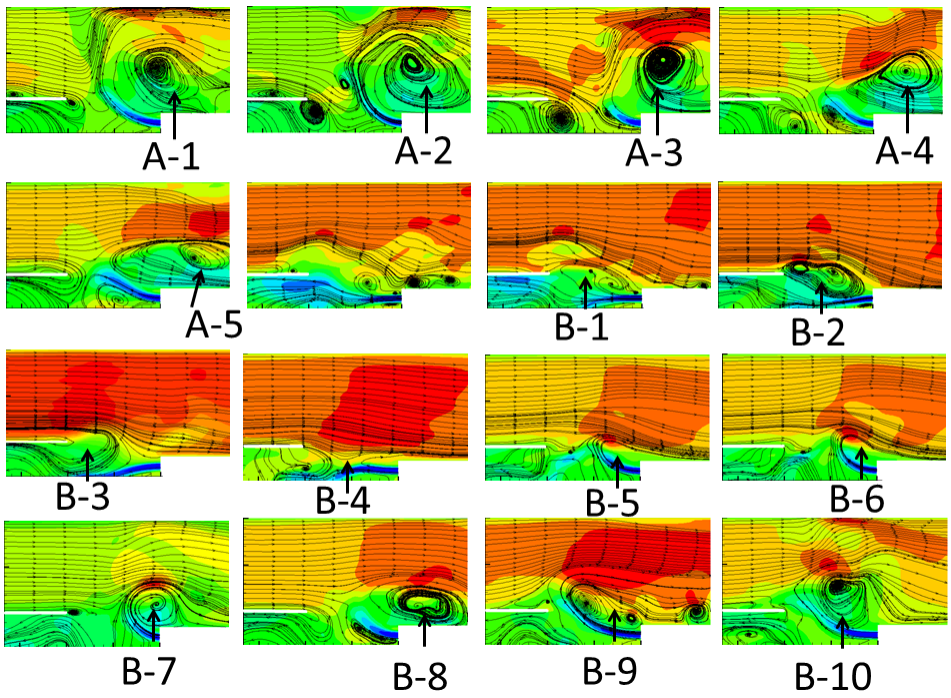


Figure 3.16: Streamwise velocity contours and streamlines on spanwise mid plane over $20Hz$ cycle (23% case)

For highest mass ratio case (36%) the velocity power spectra show a dominant mode at $106Hz$ consistently at all locations under consideration. The overall nature of the spectral peak is broadband, with much of flow energy associated with the modes around $106Hz$. In comparison with 23% case the spectral records indicate reorganization of the flow oscillation at 36% mass ratio. A low frequency mode is also observed at around $40Hz$ and no other distinct peaks are observed however, only the emphasize is given only on dominant peak where most of the flow energy is associated. The estimation of bulk flow frequency though a frequency spectra at $x/H = 1.5$ and $y/H = 0.5$ (Figure 3.17) shows the dominant peak

at $109Hz$ is observed indicating the synchronized flow oscillations. The velocity signal at $x/H = 0.075$ show larger flow amplitudes of oscillations ($\pm 20m/s$). Indicating presence of secondary jet at monitoring location; a greater periodicity is observed compared to 23% case. Evidence of local flow acceleration at $x/H = 0.075$ and $y/H = 0.04$ is observed in the streamwise velocity signal with positive peaks of oscillation reaching $15m/s$ to $20m/s$.

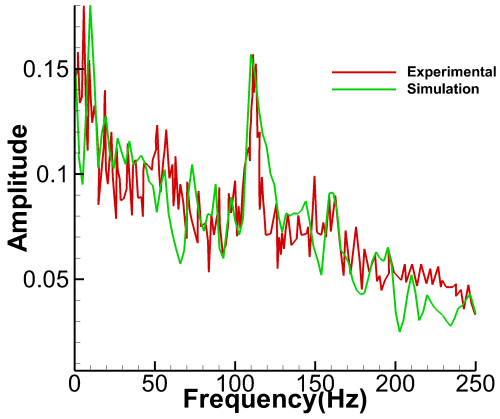


Figure 3.17: Velocity power spectra at $x/H = 1.5$ and $y/H$=0.5

Streamwise velocity contours and streamline is visualized in Figure 3.18 over a frequency cycle of $106Hz$. In the first instance (A-1), the secondary jet is rolled up in primary channel forming a recirculation bubble similar to a bubble observed in previous cases. The stronger secondary jet pushes the instantaneous stagnation point well inside the primary channel above the splitter plate and the splitter plate tip vortex is pushed below it. The main channel flow bifurcates upon the stagnation point and a stream is formed between the rolled up secondary jet and splitter plate. This forms a counter current shear layer under the secondary jet with a vortex within it counter balancing the upward pull due to the larger recirculation bubble above the secondary jet. The jet begins flapping downward, moving the instantaneous stagnation point near the tip of the splitter plate.However, due to stronger counter flowing shear, a vortex is almost immediately initiated as the jet flaps horizontal arresting the downward motion and rolling it again in the primary channel. It is interesting to observe that recirculation in the primary channel does not completely convect away at

any instant of time and the bubble oscillations appear to be synchronized with the secondary jet.

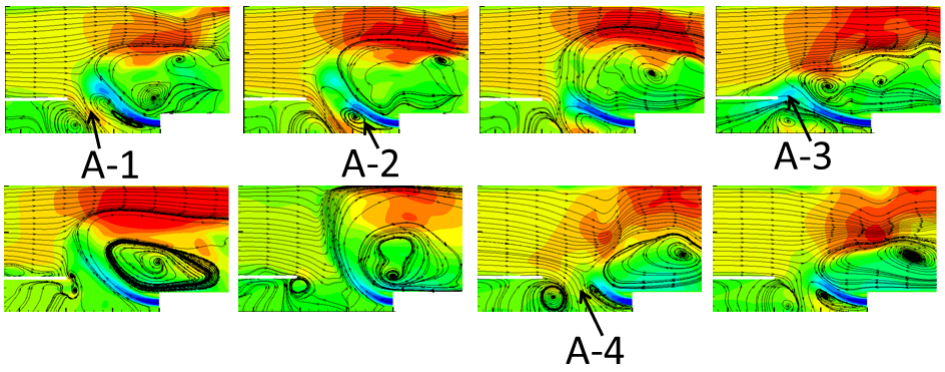


Figure 3.18: Streamwise velocity contours and streamlines on spanwise mid plane over $106Hz$ cycle (36% case)

Preliminary observations of the counter flowing shear layer show, vortex shedding at the splitter plate tip is due to Kelvin Helmholtz instability mechanism. A second mechanism is found to be secondary jet oscillation due to competition in recirculation bubble formed in jet roll up and vortex shed at the tip of splitter plate. A third mechanism of merging spanwise vortices (Elliptic instability) is observed however, no attempts are made for its quantification in this study. The schematic of instability mechanisms are shown in Figure 3.19.

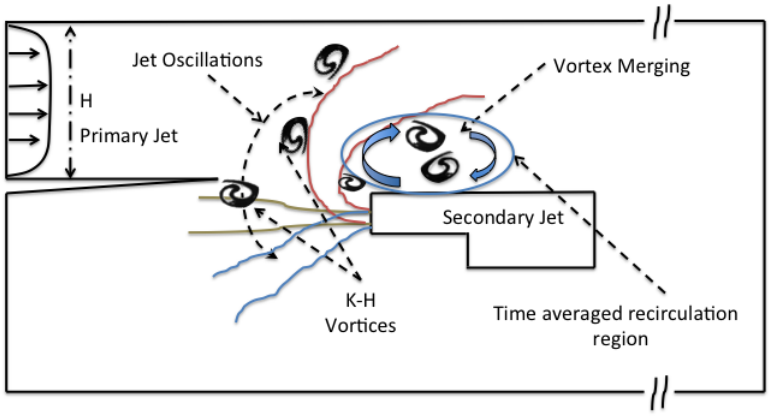


Figure 3.19: Schematic of instability mechanisms

A snapshot of the instantaneous 3D flow structures for 36% case is shown in Figure 3.20. Instantaneous 3D flow structures for 23% and 36% case are found to be qualitatively

very similar. Two types of vortical structures observed ($i$) Spanwise and ($ii$) Streamwise oriented. The evolution of spanwise vortex is due to primary K-H instability that occurs immediately downstream of the splitter plate. The higher level of turbulence spanning most of the domain is attributed to the large unsteadiness created by jet oscillation and streamwise aligned vortical structures. The combination of spanwise and streamwise aligned vortical structures give rise to highly three dimensional flow field. We discuss the nature of these flow structures and their dynamical characteristics in section 3.4.1.

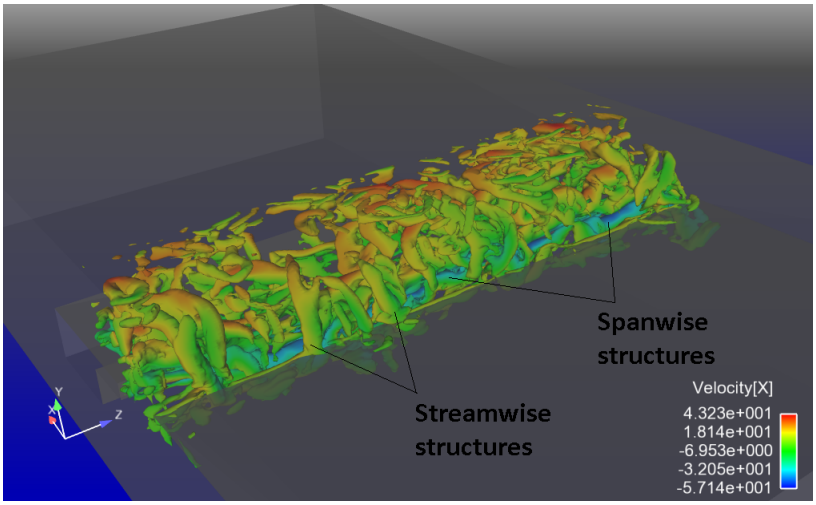


Figure 3.20: 3D Flow structures at 36% case

#### 3.3.2.2 Primary Instability Unstable velocity profile

Although phenomenological explanation is provided of secondary jet behavior and flow oscillation in order to quantify the primary instability at the tip of the splitter plate the 7.5% mass ratio case is reconsidered. In 7.5% case, the vortex shedding at the splitter plate is relatively unperturbed, as a spatial separation is observed between the spanwise two dimensional vortex and three dimensionality due to secondary jet roll up. From a series of instantaneous flow fields taken at spanwise mid-section, a instant of time just before the formation of vortex at the splitter plate tip. At such instant the counter flowing shear layer is parallel and the flow field is locally, two dimensional. The velocity profile at the tip of splitter plate is shown in Figure 3.21.

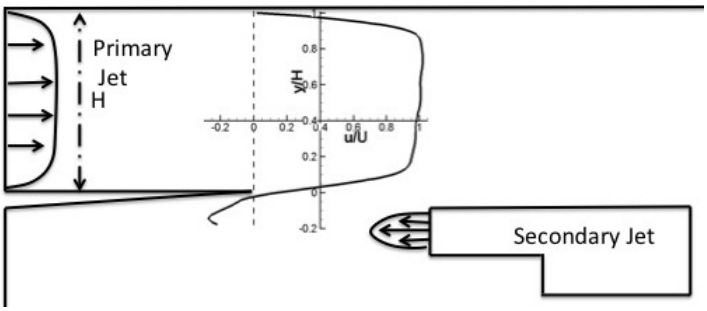


Figure 3.21: Instantaneous velocity profile before the onset of vortex evolution at the edge of splitter plate

The stability of the scaled velocity profile U is analyzed by solving Orr-Sommerfeld equation Drazin and H. (1981) for a generic perturbation $\phi$ and wavenumbers $\alpha$.

$$\phi^{iv} - 2\alpha^2\phi^{ii} + \alpha^4\phi = i\alpha Re\left\{\left(U - \frac{\omega}{\alpha}\right)\left(\phi^{ii} - k^2\phi\right) - U^{ii}\phi\right\} \tag{3.16}$$

with boundary conditions,

$$\begin{aligned} \phi\left(\frac{-1}{2}\right) &= 0 \qquad & \phi\left(\frac{1}{2}\right) &= 0 \\ \phi'\left(\frac{-1}{2}\right) &= 0 \qquad & \phi'\left(\frac{1}{2}\right) &= 0 \end{aligned} \tag{3.17}$$

The Orr-Sommerfeld equation is solved using finite difference method; a second order accurate finite difference discretization was used. The Reynolds number was set to, $Re = 14700$ corresponding to the main channel flow.

Figure 3.22 shows the growth rate vs. wavenumber. The highest growth rate of most unstable mode was found to be at wavenumber $\alpha = 3.83$. The most unstable mode at wavenumber $\alpha = 3.83$ was found at $\approx 101Hz$. This frequency is found in good agreement with the frequency of primary (Kelvin-Helmholtz) instability found though spectral content. This agreement establishes, that primary instability (K-H mode) arises through instability of counter flowing shear layer velocity profile at nominally reverse velocity and the time scale of this instability did not change with increased secondary flow as seen though spectral content.

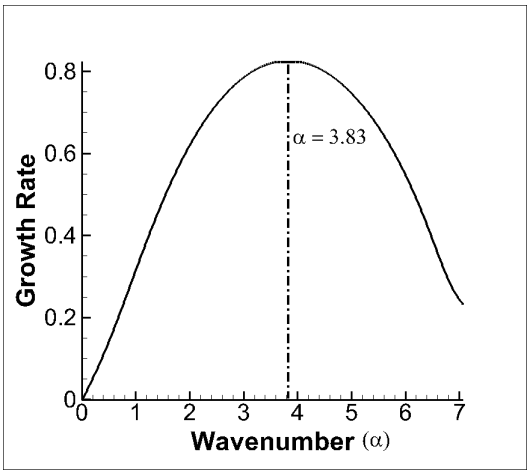


Figure 3.22: Growth rate vs. Wave number ($\alpha_{max} = 3.83$)

### 3.4 Global stability analysis

The verification of onset of global mode in Strykowski and Niccum (1991) is done by ($i$) spectral inspection to determine the limit cycle behavior, ($ii$) response to the low level external forcing to determine if the flow field is self-excited and ($iii$) verifying if the saturation amplitude of the perturbation satisfies the Landau equation a supercritical Hopf bifurcation. However the authors point out that these tests do not conclusively prove the existence of global mode. Nevertheless these methods were effectively used to show transition and onset of global mode in jet in cross-flow Davitian et al. (2010).

The increase in computational capability and availability of infrastructure has made computationally expensive approaches in global stability analyses of complex flows viable. Although the direct method is less attractive due to very large matrices arising in a practical / well resolved problem. In this direction, the numerical solution of temporal and spatial instability analysis by forming an algebraic eigen value problem arising from linearized N-S type equation was attempted bySuslov S. (2006). The linear stability analysis of Couette-Taylor flow was conducted (Edwards et al., 1994) by using implicitly restarted Arnoldi method. Dynamic mode decomposition is method similar to Koopman mode developed by Schmid and Sesterhenn (2009); Schmidt (2010). They showed that the method in case of

linearized flows leads to extraction of modes that are equivalent to modes of global stability analysis and in non-linear regime they are approximation of the dynamically dominant flow feature. In the present study, dynamic mode decomposition is used to identify dynamically significant modes corresponding flow structures and instability mechanisms.

### 3.4.1 Dynamic Mode Decomposition - a brief overview

Dynamic mode decomposition utilizes a series of instantaneous flow fields at regular temporal spacing $\Delta t$, termed as snapshots. The sequence of $N$ snapshots are arranged in matrix form $V_1$ and $V_2$,

$$\begin{aligned} V_1 &= [v_1, v_2, , v_{N-1}] \\ V_2 &= [v_2, v_3, , v_N] \end{aligned} \tag{3.18}$$

Generally $N$ is taken sufficiently large enough to assume further snapshots will be linearly dependent. Further a linear operator is $A$ defined such that it advances the flow field from one time level to next. For a linear process this matrix is uniquely defined whereas for a nonlinear process this amounts to locally linear approximation. With such an operator the snapshots can be written as,

$$V_1 = [v_1, A_1 v_1, A_2 v_1, , A_{N-1} v_1] \tag{3.19}$$

Similarly arranged snapshots are written as,

$$AV_1 = V_2 \tag{3.20}$$

where A is system matrix that governs the evolution of the flow field and eigen values of A yields the complete dynamical information of the system and corresponding modes (eigen vectors). Realizing the assumption that N vectors (snapshots) are linearly independent the

last vector can be expressed as linear combination of remaining vector in matrix form,

$$AV_1 = V_2 = V_1 S \tag{3.21}$$

where $S$ is companion matrix. Eigen values of $S$ are approximately equivalent to eigen values of A. $S$ can be then computed using QR factorization of $V_1$ resulting in,

$$S = R^{-1} Q^H V_2 \tag{3.22}$$

For more robust decomposition SVD is employed for decomposition $V_1 = U\Sigma W^H$. The approximation of S then can be expressed as, $S \sim U^H V_2 W^{-1}$. The eigen values of S then yield the dynamical information of system represented by $A$. For a more in-depth discussion on this method refer to Schmidt (2010). The eigen modes are then calculated by $\Phi = UE_v$ where $E_v$ is eigen vector matrix of $S$. The eigen values are given as $\lambda_i = (\sigma)_i/\Delta t$ where $\sigma_i$ is the computed Ritz value.

### 3.4.2 DMD of Countercurrent shear flows

In the present case DMD analysis is conducted over the domain of interest shown in Figure 3.1; entire spanwise length is considered.

This region selected for DMD contains the dynamics of secondary jet interaction and covers the entire streamwise length of recirculation bubble. The region of interest has total of 1.5 million grid points. Total of 1300 snapshots separated by $\Delta t = 1.0e-4s$ ate collected. The time step chosen satisfies the Nyquist criterion Schmidt (2010) $f_s \geq 3f$ where $f_s$ is sampling frequency and $f$ is the frequency of the dynamical process to be resolved. The computed Ritz values satisfy the convergence criterion $e_R < 1.0e^{-6} * norm(A)$ where $e_R$ is maximum error in Ritz values for all eigen modes.

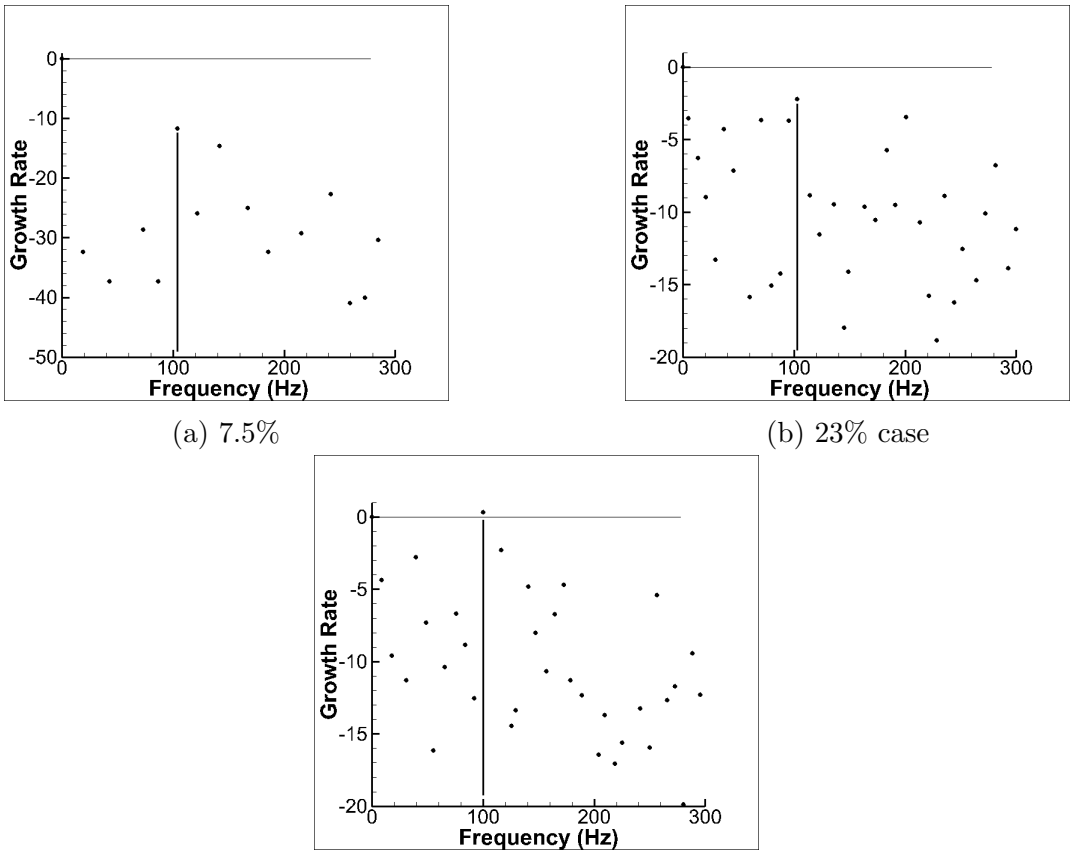


(a) 7.5%

(b) 23% case

(c) 36% case

Figure 3.23: DMD growth spectrum for all cases

Figure 3.23 shows the DMD spectrum for 7.5%, 23% and 36% mass ratios. In all three cases $\sim 100Hz$ mode is found to have highest growth rate that is consistent with spectral data at $x/H = 0.075$ and stability analysis using Orr-Sommerfeld equation. As mass ratio is increased the growth rate of $100Hz$ mode increases and at 36% case a positive growth indicates the transition in the dynamics from convective to self-excited global mode. The corresponding eigen mode of largest eigen value is visualized ($1^{st}$ DMD mode) for all mass ratio cases. The flow structures of corresponding modes are represented by $2^{nd}$ eigen value method of Jeong and Hussain (1995). Similar to instantaneous flow field two types of flow structures are found, ($i$) spanwise oriented and ($ii$) streamwise oriented overlapped onto spanwise structures. For clarity the streamwise and spanwise flow structures are separated.

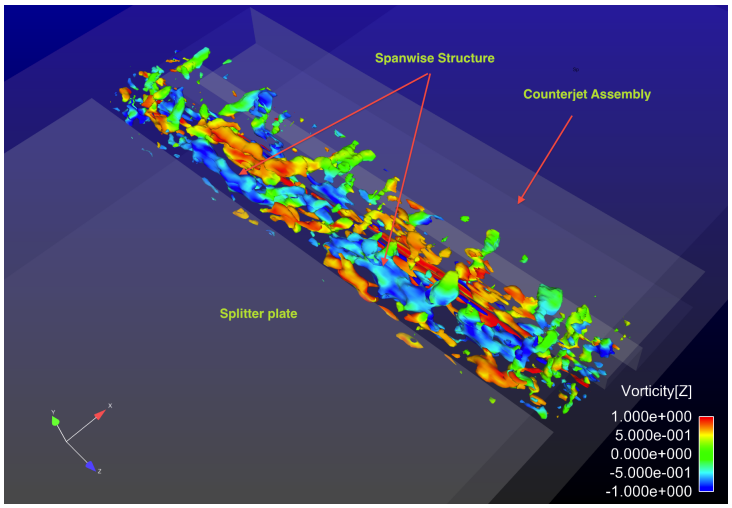


(a) 7.5%

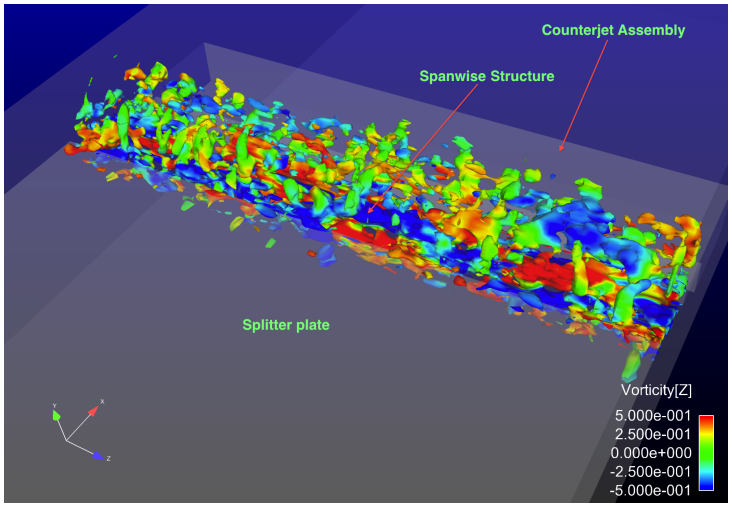


(b) 23%

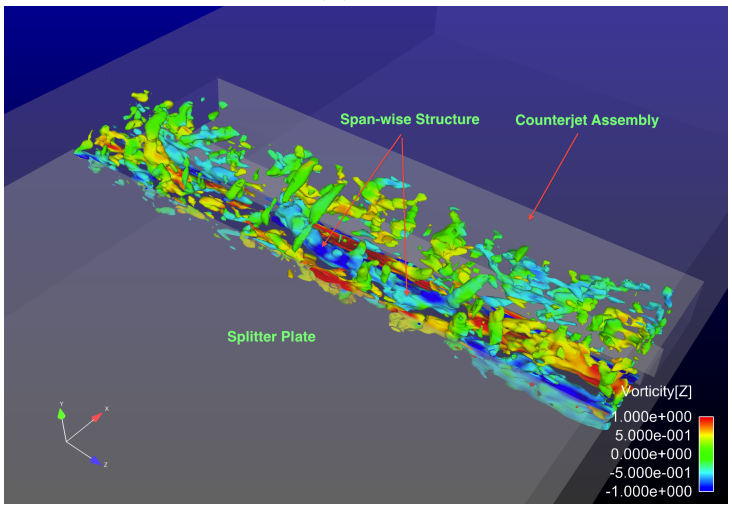


(c) 36%

Figure 3.24: Spanwise nature of most unstable mode ($\approx 100Hz$ DMD mode)

Figure 3.24a, 3.24b and 3.24c show the spanwise flow structure at the edge of the splitter plate. Contours of flow spanwise vorticity is plotted over flow structures (iso-surfaces of $\lambda_2$). In order to place the discussion in perspective, the similarities are drawn between the spanwise part of the most unstable DMD modes and spanwise nature of instantaneous flow structure for 7.5% case (Figure 3.14). The spanwise flow structures also observed instantaneously for higher higher secondary jet velocity; traces of spanwise structures are observed in Figure 3.20. However, the spanwsie structures are obscured by overlapping streamwise vortices. The spanwise vortex shedding at the end of the splitter plate is results of primary instability that was discussed earlier. The time scale of spanwise vortices are observed to remain almost invariant ($\sim 100Hz$) as depicted by the spectral characteristics in the downstream neighborhood of splitter plate tip. Instantaneous streamline plots for all mass ratios shown in Figure 3.13a,3.16 and 3.18 and the description of the jet oscillation over the time scale of $\sim 100Hz$ frequency cycle emphasizes the role of spanwise vortices in the secondary jet oscillation.

Figure 3.25 shows the streamwise flow structures associated with $1^{st}$ DMD (highest growth rate) mode for 23% and 36% mass ratio case colored with streamwise component of vorticity. They show the set of counter rotating streamwise vortex pairs originating from leading edge of the splitter plate and overlapping the recirculation region. Counter rotating streamwise vortex pairs are typical features associated with secondary instabilities (elliptic / vortex merging) in planar shear layers. The evolution of stream-wise vortices is due to two mechanisms. (I) Deformation of single spanwise vortex due to generic three dimensional perturbation in a shear field where the locally deformed part of vortex that encounters the local high velocity is advected quicker, leading to stretching and stream-wise alignment leading to counter rotating vortex pairs (Wu et al., 2006) ($ii$) Merging of span-wise vortices (Elliptic instability) The formation of streamwise vortices and associated 3D instability mechanism in merging of spanwise vortex (Bernal and Roshko, 1986; Lasheras and Choi, 1988). While both spanwise and streamwise flow structures have identical frequency, only the spanwise

flow structures are the consequence of primary instability mechanism and the streamwise flow structures are the outcome of secondary mechanisms as described earlier. Therefore, spanwise flow structures are only deemed as globally unstable in 36% mass ratio case.

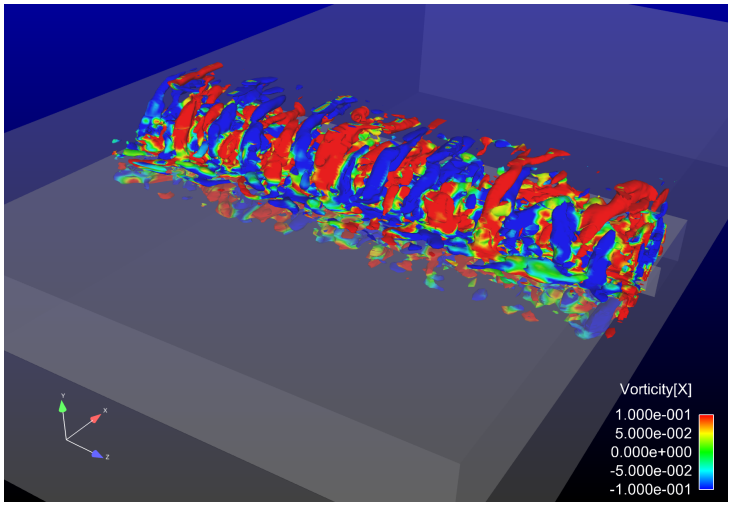


(a) 23%

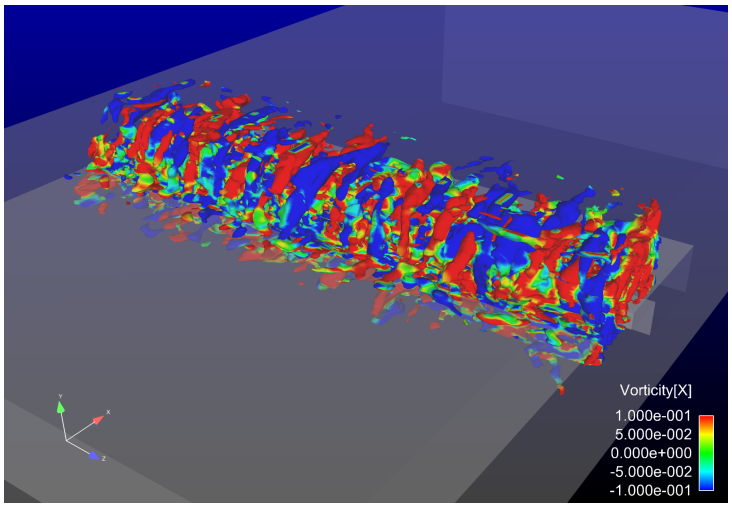


(b) 36%

Figure 3.25: Streamwise counter rotating pair of flow structures

#### 3.4.2.1 Global mode frequency synchronization (36% case)

Additional spectral information is obtained at locations $x/H = 0.075, 0.15$ and $y/H = 0.04, 0.85$ for points 1,2,5 and 6 and $x/H = 1.7, 2.0$ and $y/H = 0.04, 0.85$ for points 3,4,7 and 8 shown schematically in Figure 3.26. Monitor point 5,6,7, and 8 are located near the

upper wall and out of recirculation bubble and experience only the local flow acceleration and deceleration. Point 1 and 2 are located in the vicinity of splitter plate tip and experience jet oscillations and splitter plate tip vortex shedding. Point 3 and 4 are located within the time averaged recirculation bubble witness a complex unsteady flow as observed in Figure 3.18. The four separate locations experience a variety local flow conditions as elaborated. However, at all the locations the dominant mode is observed at $106Hz$ consistently. The self-excitation in 36% case triggers the frequency synchronization of dominant instability mode with other dynamical phenomenon leading to emergence of dominant frequency at multiple spatial locations (Huerre and Monkewitz, 1990). In the present case the synchronization is realized through coupling of primary instability mechanism and secondary jet oscillation.

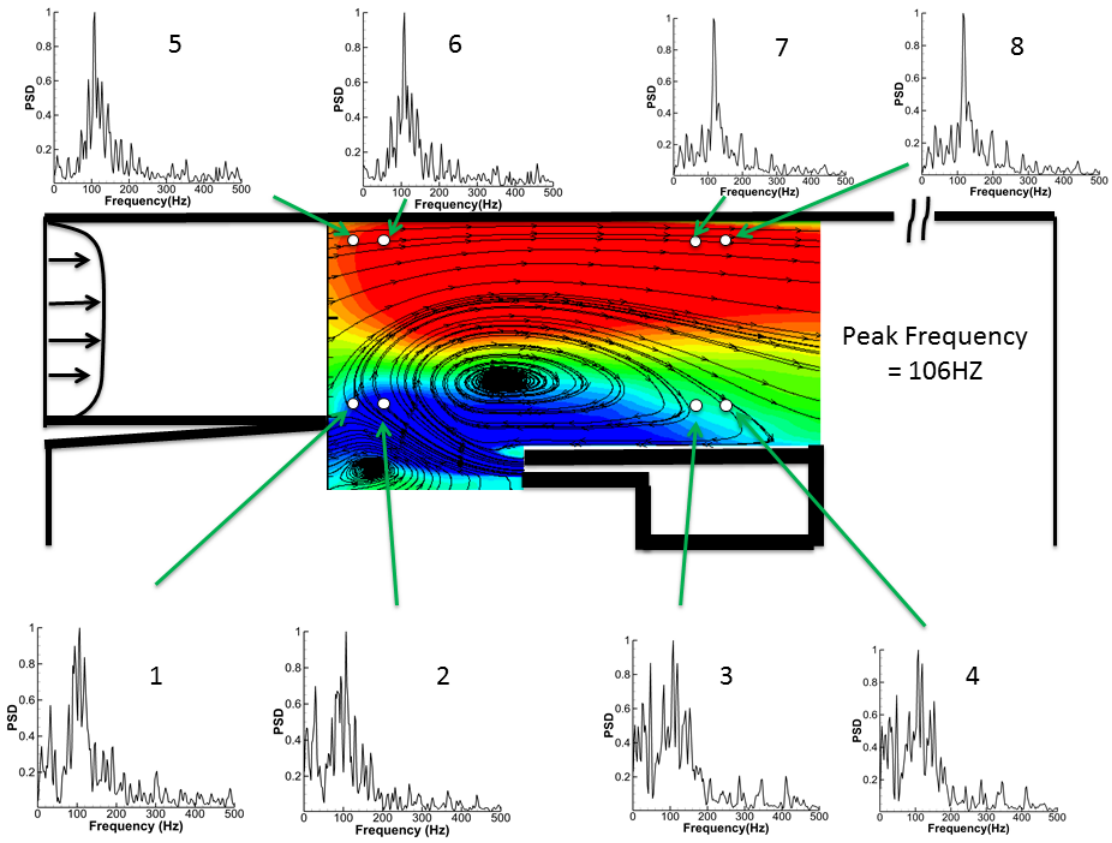


Figure 3.26: Frequency synchronization for 36% case (Peak frequency $106Hz$)

## 3.5 Concluding remarks

A momentum driven countercurrent shear flow is simulated using large eddy simulation for three mass ratios (7.5%, 23% and 36%). An excellent agreement is found in simulation and experiments in terms of mean flow characteristics and spectral content of velocity signal at specified location. The interaction of primary and secondary jet was analysed through spectral analysis and flow visualization technique. Three distinct instability mechanisms are observed, (*i*) Kelvin Helmholtz, (*ii*) secondary jet oscillation and (*iii*) elliptic instability of vortex merging. kelvin-Helmholtz mode was found to emerge from instability of a counter shearing velocity profile, verified by solving Orr-Sommerfeld equation for a generic perturbation. A three dimensional stability analysis was conducted using Dynamic mode decomposition method. The analysis showed, as velocity of secondary jet was increased, the primary instability mode transited to a global mode triggering synchronization in frequency of flow oscillation over entire domain. The reverse flow setup for 36% case was in excess of 30% of streamwise flow that satisfies the criterion for establishment of global mode (Hammond and Redekopp 1998). Although the reverse flow in 23% case appears to be instantaneously exceeding 30% of streamwise flow, the downward jet oscillation causes the convective nature of the flow and this is verified by the results of DMD analysis. The global mode at 36% case was found to be spatially synchronized with the secondary jet oscillation, flow acceleration in the upper region of primary flow and the recirculation bubble oscillations. The highly three-dimensional nature of the flow field at higher mass ratio cases was attributed to the counter rotating pairs of streamwise aligned secondary flow structures (due to secondary instability mechanism (vortex merging)) and non-uniform spanwise oscillations of secondary jet. This study shows that the turbulence in the primary channel of dump geometry can be controlled by using a secondary counter flowing jet. The high levels of turbulence and three-dimensionality of the flow field along with temporally sustaining recirculation bubble makes such flows an excellent candidate for potential mixing and combustion applications.

# Chapter 4
# Effect of Discrete Control Jets on Planar Countercurrent Shear Flows in Dump Geometry

## 4.1 Introduction

In the previous chapter the dynamics of planar momentum driven countercurrent shear flow in dump geometry was investigated for various secondary jet to primary jet mass flow ratios. The principal idea behind the momentum driven countercurrent shear layer was to excite and control the desirable flow dynamics by application of secondary control jet in the counter flowing configuration to the primary channel flow. The study revealed large scale oscillation of the free momentum driven jet coupled with Kelvin-Helmholtz mechanism. Large unsteadiness in the recirculation bubble due to secondary jet oscillation may potentially augment the fluctuations in heat release rate - a highly undesirable characteristic for flame stabilization/combustor applications.

The dynamic characteristics of the spanwise continuous secondary jet and mechanism of flow oscillations were detailed in previous chapter. For spanwise continuous secondary jet, the onset of Kelvin-Helmholtz vortex at the splitter plate tip was observed uniformly in spanwise direction. The counter flowing nature of the secondary jet (shear layer) augments the spanwise K-H vortex to form a larger recirculation above the secondary jet with pressure minima at the core. The pressure difference causes the rollup of secondary jet in the primary channel region. This schematic of this mechanism is shown in 3.19.

In order to mitigate the the effect of large secondary jet oscillations, a spanwise discrete secondary jet is proposed and studied in this chapter. The spanwise discrete nature is designed to achieve following objectives,

($a$) Disrupt the spanwise nature of Kelvin-Helmholtz vortex development at the tip of the splitter plate.

($b$) Allow entrainment of the fluid through the gap between the discrete jets to alleviate the pressure difference across the secondary jet in cross stream direction.

($c$) Retain the ability of countercurrent shear to maintain higher turbulence levels.

### 4.1.1 Case matrix and parameters

The schematic of the discrete secondary jet configuration is shown in Figure 4.1. The base geometry and flow conditions used for the study of discrete secondary jets is identical to the previously investigated configuration of spanwise continuous secondary jet for 36% case.

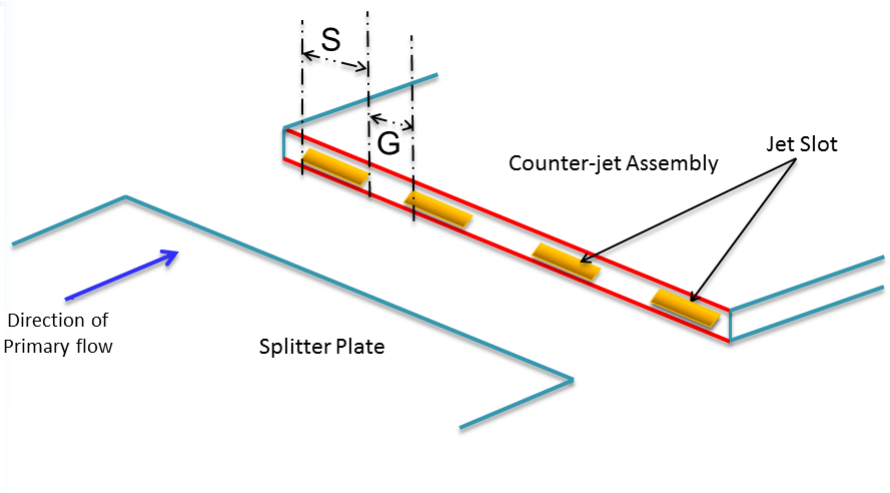


Figure 4.1: Schematic of discrete secondary jet

The width of individual discrete jet (S) and gap between the two successive jets (G) are chosen as parameters controlling the discreteness of the secondary jet. The choice of jet width is based on the length scale of spanwise modulations of continuous jet in the base configuration. Figure 4.2 shows the spanwise variation of coefficient of cross correlation of

spanwise velocity component at $x/D = 0.0$, $y/D = 0.0$ and $z/D = 4$ along the spanwise direction for 36% case. The coefficient of cross correlation is observed to have modulations of $8mm$-$20mm$ in the spanwise direction. These modulations are indicative of

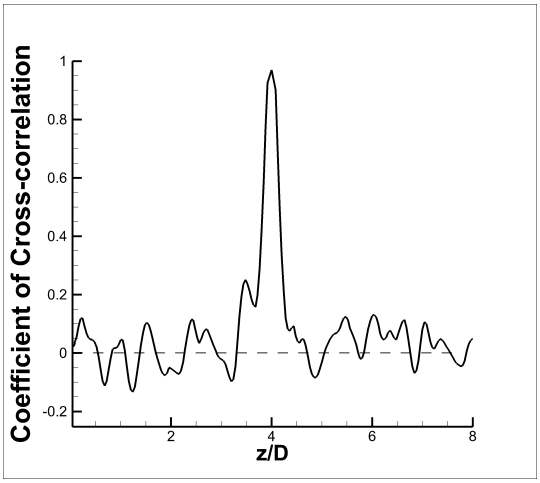


Figure 4.2: Cross-correlation of spanwise velocity component

Based on this estimate of spanwise modulations of continuous secondary jet the following case matrix is designed where, the gap between the jets is arbitrarily chosen.

Table 4.1: Discrete jet case matrix

| Case name | Jet width (S mm) | Gap width (G mm) |
|---|---|---|
| S4G4 | 4 | 4 |
| S8G4 | 8 | 4 |
| S16G4 | 16 | 4 |

## 4.2 Results and Discussion

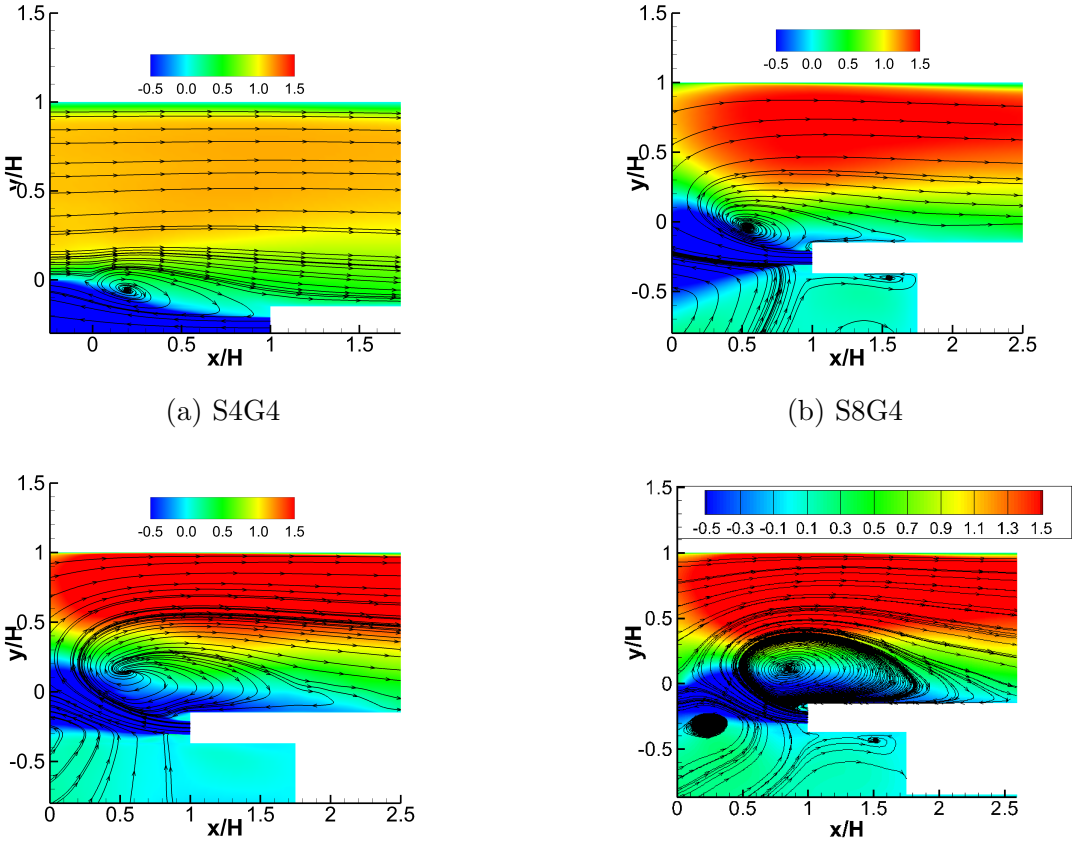


(a) S4G4

(b) S8G4

(c) S16G4

(d) Spanwise continuous jet

Figure 4.3: Streamwise normalized velocity contours and streamlines at spanwise center of discrete jet and spanwise continuous jet

Figure 4.3 show the time averaged velocity streamwise velocity contours, streamlines and Figure 4.4 shows normalized total turbulence (based on three components of velocity fluctuation) on a spanwise normal plane passing though the center of the discrete jet. For case S4G4 the recirculation bubble is observed in shear layer region immediate downstream region of splitter plate. No acceleration in the mean flow filed was observed due to shear layer interaction. The total turbulence levels (Figure 4.4a) of about 50% seen only in shear layer region and lower region of primary channel. Absence of turbulence in upper half of primary channel suggests the influence of shear layer interaction are limited to a region in vicinity of

shear layer.

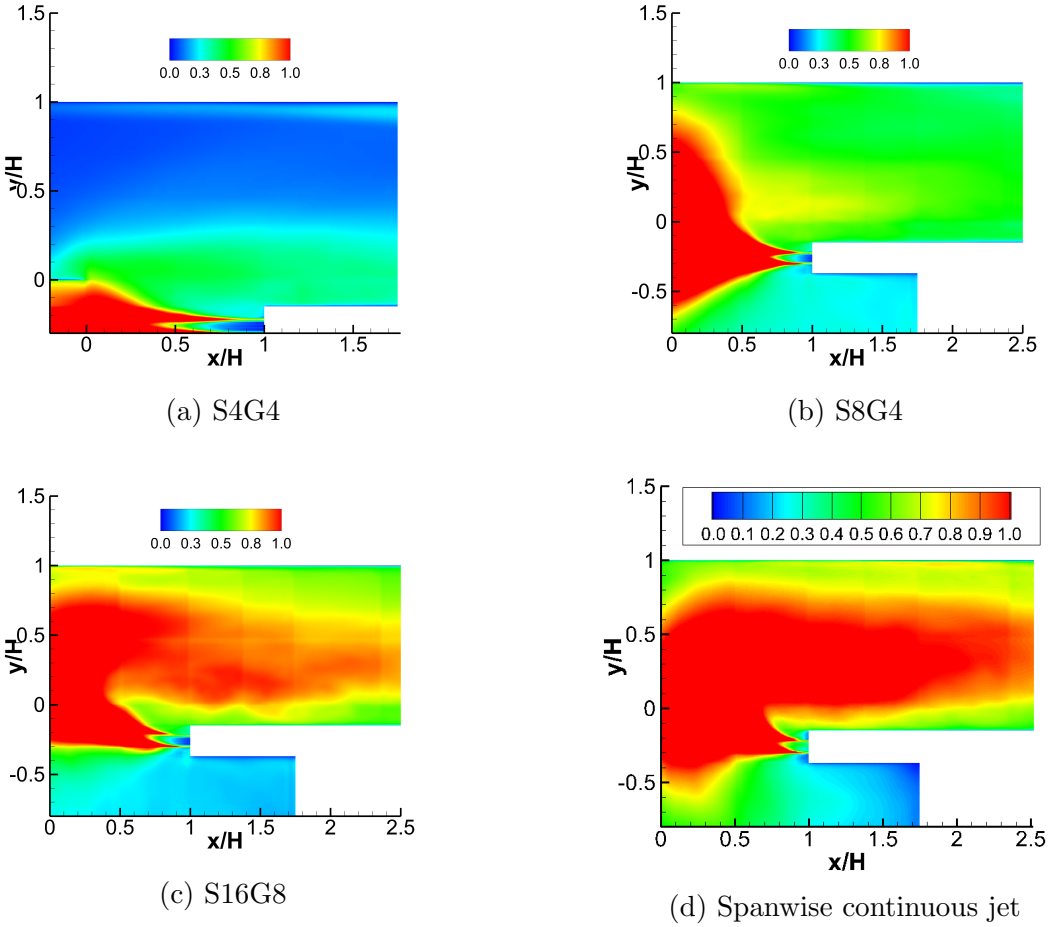


(a) S4G4

(b) S8G4

(c) S16G8

(d) Spanwise continuous jet

Figure 4.4: Total turbulence contours at spanwise center of discrete jet and spanwise continuous jet

However, as the width of discrete secondary jet in increased to $8mm$ (case S8G4), a bifurcated stream from secondary jet is seen rolled up in the main channel region. The dark blue region shows the increased spreading of secondary jet compared to case S4G4. The primary channel flow is accelerated by the shear layer interaction to $\approx$ 150% of primary channel inlet velocity. The turbulence levels Figure 4.4b show increase in turbulence levels in excess of 50% over entire primary channel region. The highest levels in excess of 100% turbulence is observed in secondary jet spread region. For jet width of $16mm$ (case S16G4), a significantly large recirculation bubble is observed with secondary jet roll up in the primary

flow region. The flow field accelerated to about 180% of primary channel inlet velocity. About 100% increase in turbulence levels was witnessed in the primary channel. As the width of the discrete jet is increased, the mean and turbulence flow field approaches that of continuous jet, indicating the spanwise dimension of the jet plays a critical role in dynamics of discrete secondary jets.

Therefore, the velocity and turbulence field in the gap between the discrete jets is shown in Figure 4.5 and 4.7. The comparison of mean velocity field in the primary channel appeared in Figure 4.3a and 4.5a indicates the spanwise uniformity except in the shear layer region where nor recirculation bubble is observed in the gap between the jets. For case S8G4 (Figure 4.5b) a small recirculation bubble is observed over the secondary jet assembly. The bubble size increased for secondary jet width of $16mm$ (case S16G4). The acceleration in the mean velocity field is observed similar to central region discrete jet. However, the marked distinction in the mean flow field at center of the discrete jet and in the gap between them, is the entrainment of the fluid below the secondary jet region into the the primary stream. The fluid entrainment alleviate the pressure differential setup across the secondary jet in cross stream direction. For larger jet width the increased separation of entrainment regions at the spanwise end of the discrete jet does not allow sufficient fluid entrainment therefore achieving the condition of spanwise continuous jet. For shorter jet width, the entrainment appears to be sufficient to reduce the pressure difference significantly and the jet roll up is completely absent (case S4G4).

The turbulence field between the discrete jets is shown in Figure 4.7. For discrete jet width of $8mm$ (case S8G4) the the highest turbulence levels are observed in the shear layer interaction region, however, the increase of 50% turbulence level observed at central region of discrete jet is maintained. Indicating the consistent increase of turbulence levels in spanwise direction. However, for $16mm$ jet width, the higher turbulence levels are observed in a central region above the recirculation bubble. This is indication that locally higher turbulence levels in the central region of discrete jet is a consequence of secondary jet rollup that was not

observed in smaller secondary jet widths.

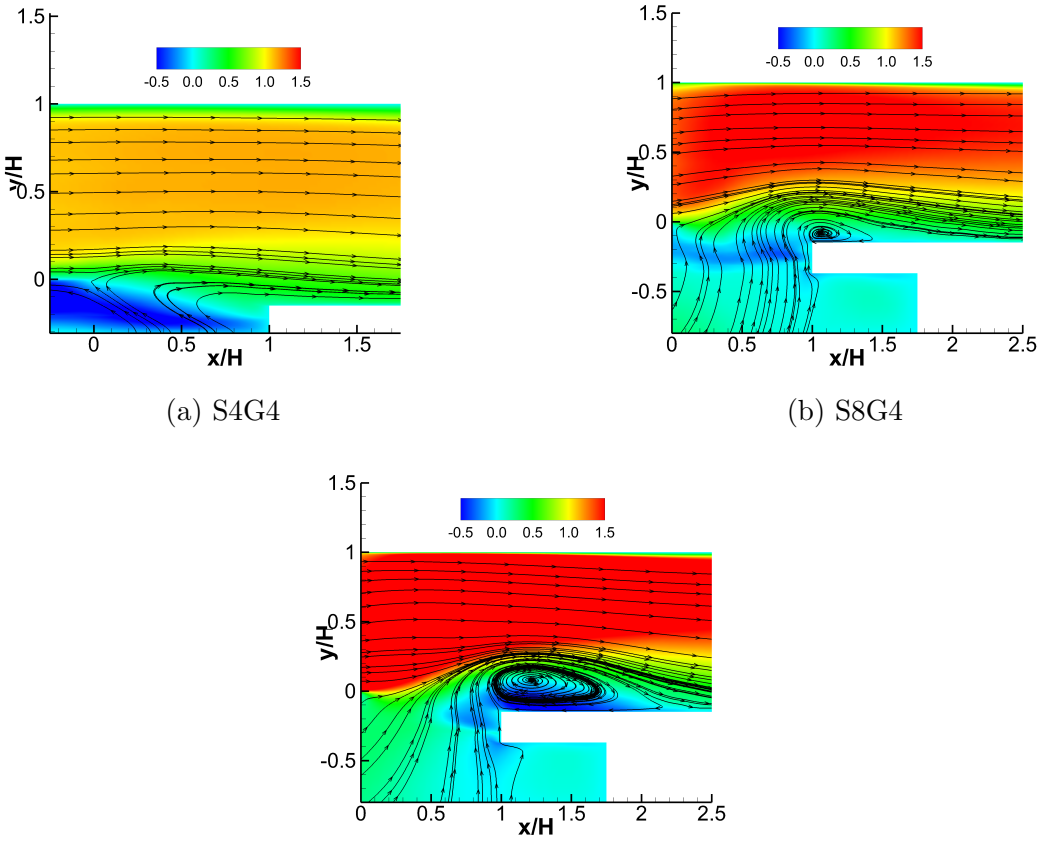


(a) S4G4

(b) S8G4

(c) S16G4

Figure 4.5: Streamwise normalized velocity contours and streamlines at spanwise section between the discrete jets

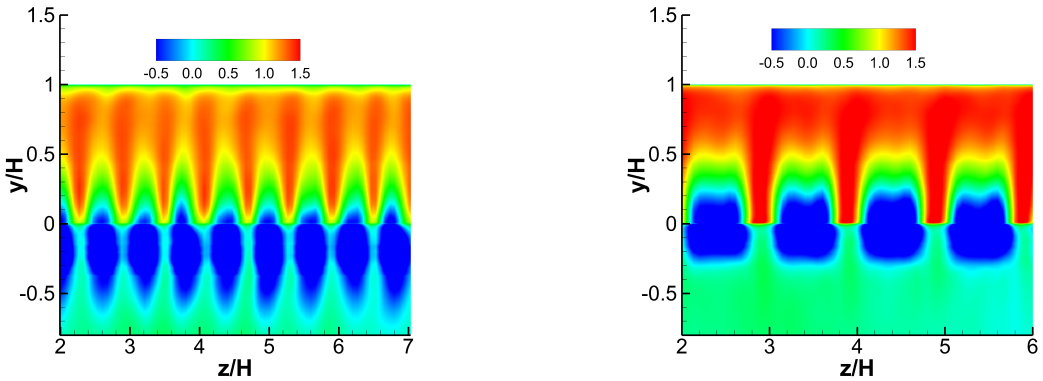


(a) S8G4

(b) S16G4

Figure 4.6: Streamwise velocity contours at streamwise normal section ($x/H$=0.0)

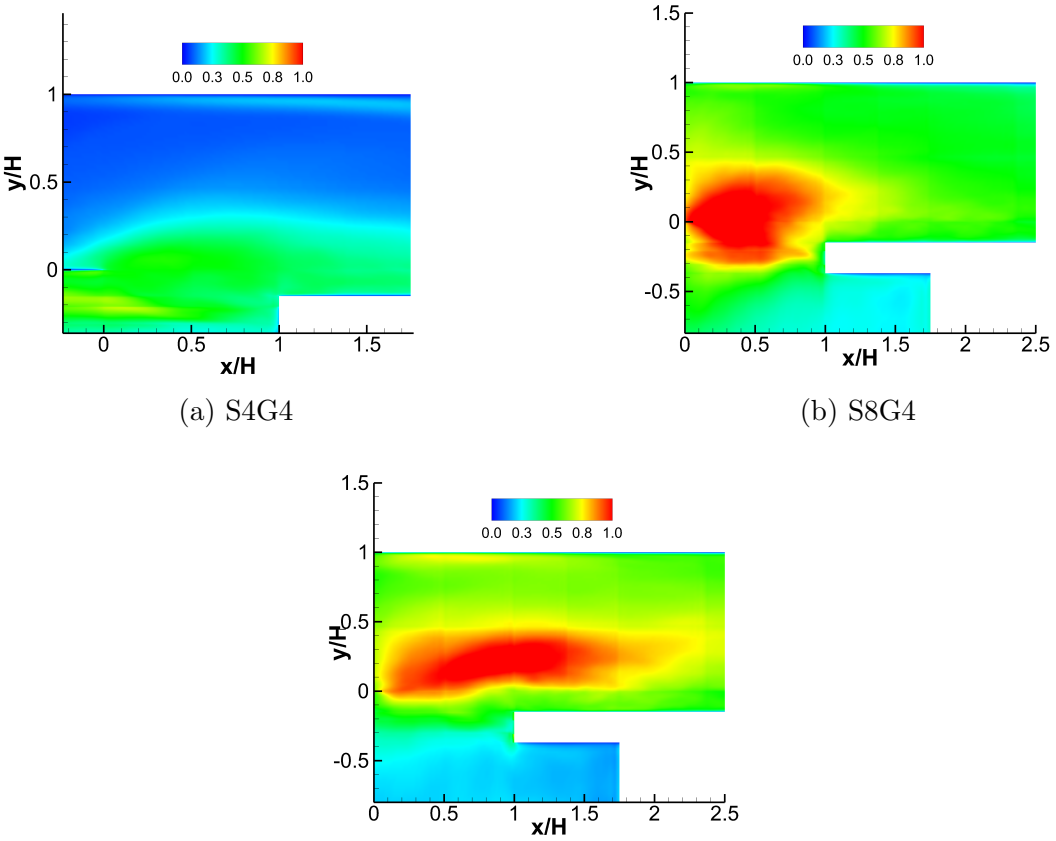


(a) S4G4

(b) S8G4

(c) S16G4

Figure 4.7: Total turbulence contours at spanwise section between the discrete jets

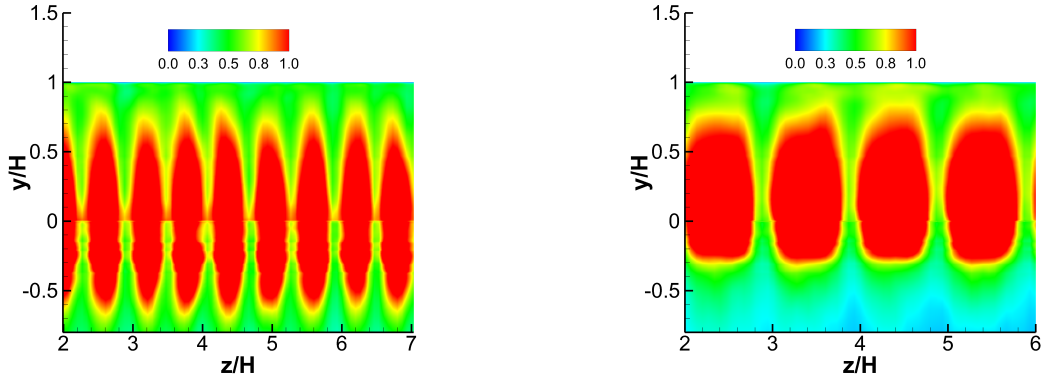


(a) S8G4

(b) S16G4

Figure 4.8: Total turbulence contours at streamwise normal section ($x/H$=0.0)

The streamwise velocity contours on a spanwise normal plane at the tip of the splitter

plate ($x/H = 0.0$) is shown in Figure 4.6 for cases S8G4 and S16G4. The dark blue region shows the secondary jet. Splitter plate is located at $y/H = 0.0$. The spanwise pockets of low velocity region indicate the interaction region of secondary jet and primary stream. In addition to fluid entrainment from a region below the splitter plate the gap between the discrete jets allows a the stream of fluid (as seen in Figure 4.6), aids entrainment of fluid from lateral direction in the recirculation behind the jet.

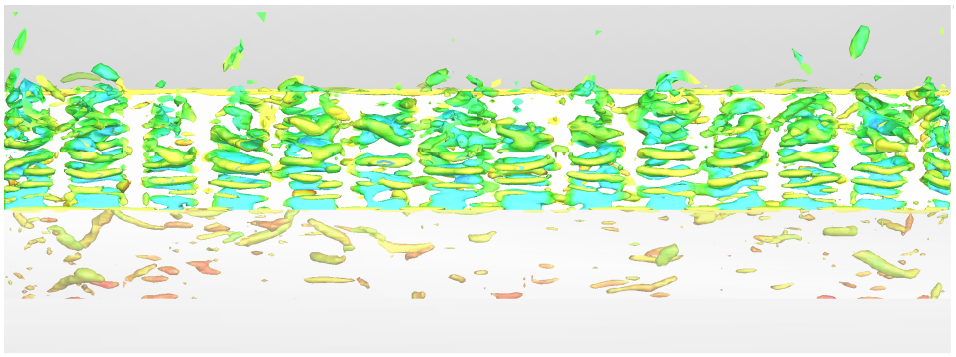

(a) Spanwise discrete shear layer vortices

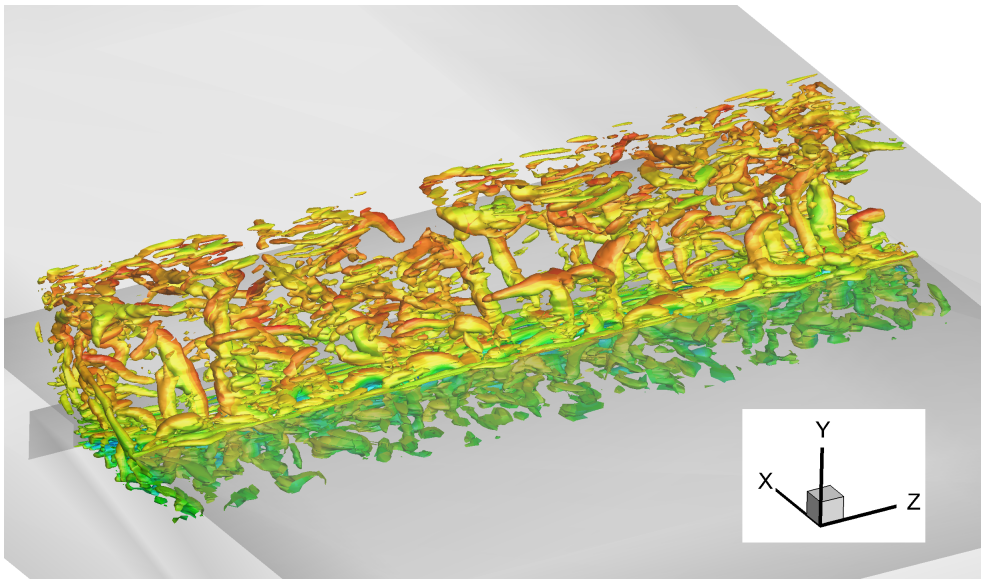


(b) Flow structures behind the secondary jet

Figure 4.9: 3D flow structures ($\lambda_2$ iso-surface) for case S8G4

The flow structures in the shear layer formed by secondary jet and primary stream are shown in Figure 4.9a. The flow structures are observed only in the shear layer formed by secondary jet and primary stream (position of discrete jet is clearly marked by the train of

vortex structures). The spanwise discrete nature of shear layer vortices allow the entrainment of the fluid from lateral ends into low pressure region at the vortex core. The cross stream pressure difference driving the secondary jet oscillations is significantly reduced by entrainment effect therefore, large oscillations of secondary jets are eliminated for shorter jet widths.

The substantial turbulence levels throughout the primary jet region in case of S8G4 is attributed to the greater degree of three dimensionality instigated behind the secondary jet. Figure 4.9b shows the flow structures behind the secondary jet spanning throughout spanwise and cross stream direction. It should be noted that these flow structures are formed only due to shear layer interaction and partial rollup of the secondary jet, unlike the case of spanwise continuous jet.

## 4.3 Concluding remarks

The effect of discrete secondary jet on countercurrent shear flows in investigated for various jet widths. The mean flow characteristics are investigated and correlated with the charcteristics of spanwise continuous secondary jet. The recirculation regions and jet rollup are significantly affected by the width of secondary jet. For shorter widths (S) the flow entrainment from the gap below the the secondary jet and main stream completely negates the jet rollup and jet is observed to be always countercurrent configuration. The primary stream is minimally influenced in terms for mean flow acceleration and turbulence. As the secondary jet width is increased higher degree of jet rollup is observed, mimicking the spanwise continuous jet. Among the secondary jet width studied, $8mm$ (case S8G4) is found to be optimal where, the jet rollups are related large flow oscillations are alleviated to a grater degree while maintaining reasonable levels (higher that 50%) of turbulence through entire primary channel region achieving all the three objectives of this study. Further study is suggested to understand the detailed dynamics of secondary jet.

# Chapter 5
# Film Cooling Flows

**Abstract**

Thermal and hydrodynamic flow field over a flat surface cooled with a single round inclined film cooling jet and fed by a plenum chamber is numerically investigated using Large Eddy Simulation (LES) and validated with published measurements. The calculations are done for a free stream Reynolds number $Re = 16000$, density ratio of coolant to free stream fluid $\rho_j/\rho_\infty = 2.0$ and blowing ratio $B.R. = \rho_j V_j/\rho_\infty V_\infty = 1.0$. A short delivery tube with aspect ratio $l/D = 1.75$ and $35^0$ inclination is considered. The flow physics is investigated through a detailed flow visualization study. The evolution of the Kelvin-Helmholtz (K-H), hairpin and Counter-Rotating Vortex Pair (CVP) vortical structures are discussed to identify their origins and draw similarities and distinctions with previously publlished work.

## 5.1 Problem Setup

A $12.7mm$ round jet with $35^\circ$ inclination angle discharging into a crossflow over a flat plate is under consideration. The schematic flow configuration is shown in (Figure 5.1). This configuration was designed for the study of film cooling applications of gas turbine blades and experimentally investigated for thermal and hydrodynamic flow field by Sinha et al. (1991). The jet is formed out of a low aspect ratio ($l/D = 1.75$) delivery tube fed with a plenum chamber that concurs with the realistic geometrical configuration of a turbine blade cooling hole. In present computational model the origin of the coordinate system is placed at the

leading edge of the film cooling hole with positive $x$ axis aligned with streamwise direction, wall normal direction with positive direction of $y$ axis and $z$ being spanwise direction. The domain spans $21D$ in streamwise direction with $7D$ upstream from origin for development of crossflow boundary layer. Flow field after jet is discharged in crossflow is studied over $15D$ streamwise length. The separation between spanwise boundaries is set to $1.48D$ symmetrically on either side of center plane, consistent with spanwise separation between array of film cooling hole in (Sinha et al., 1991). An orthorhombic plenum with plenum dimensions $8D$ in streamwise direction, $4D$ height $2.6D$ in spanwise direction and delivery tube entrance placed symmetrically at the center of top surface is considered. The dimensions are large enough to avoid any influence of plenum geometry other than entrance effects for inclined delivery tube. Crossflow is an incoming boundary layer flow with free stream velocity 20m/s and uniform temperature at $300K$. The inlet boundary layer profile is specified as,

$$u = U_\infty \left(\frac{y}{\delta}\right)^{1/5} \tag{5.1}$$

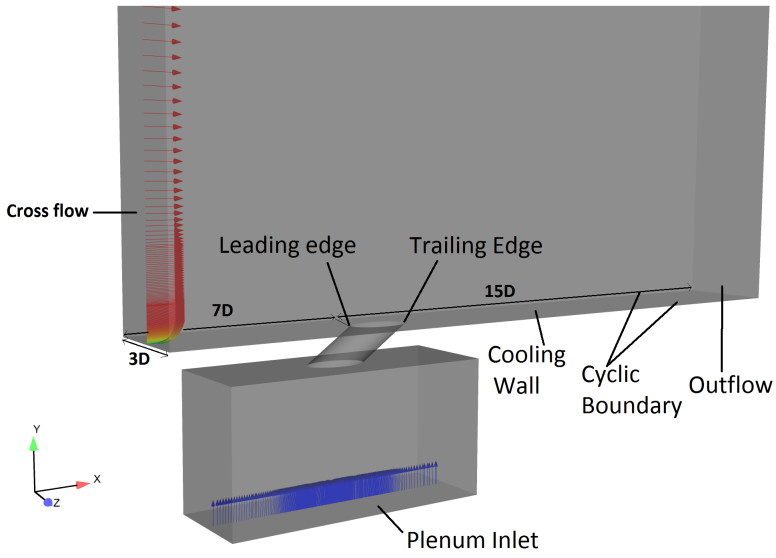


Figure 5.1: Schematic of the domain

where boundary layer thickness $\delta$ is chosen such that the boundary layer profile at one

diameter upstream of jet hole matches with measurements. Jet fluid enters plenum inlet at uniform velocity of $0.338m/s$ and $150K$ temperature. An average condition of velocity ratio $V.R. = U_j/(U_\infty) = 0.5$ and density ratio $D.R. = \rho_j/(\rho_\infty) = 2.0$ (blowing ratio $B.R. = (\rho_j V_j)/(\rho_\infty V_\infty) = 1.0$) is maintained at the jet exit. Flow exits domain through a streamwise normal boundary at $x = 15D$. A non-reflecting outflow boundary condition is applied to the exit plane such that it satisfies,

$$\frac{\partial u_i}{\partial t} + U_c \frac{\partial u_i}{\partial x} = 0 \tag{5.2}$$

Top boundary of domain is considered as free stream boundary for the crossflow whereas, lateral boundaries are treated as cyclic boundary condition. All wall boundaries are treated as no slip adiabatic walls.

## 5.2 Numerical Method and Grid independence

The numerical tool used for simulation is an in-house developed parallel CFD code for compressible flows in generalized curvilinear coordinate system. A finite volume discretization over a body fitted block structured grid is employed. A $5^{\text{th}}$ order accurate WENO (weighted, essentially non oscillatory) scheme is used to discretize convective terms. A standard second order accurate central difference scheme is used to discretize viscous terms. A second order implicit temporal discretization is used with pseudo time stepping at each physical time step. Incompressible flows at relatively low Reynolds numbers are handled with a low Mach number pre-conditioner. The code is parallelization using MPI (message passing interface) and scalability of the code is tested up to 1000 processors on HPC facilities at LSU, LONI and XSEDE (San Diego supercomputing facility). Turbulent flows are handled with large eddy simulation technique. A dynamic Smagorinsky eddy viscosity model given by following expression,

$$\mu_t = C_s^2 \bar{\rho} \Delta^2 \left( |\widetilde{S}| \right)^2 \tag{5.3}$$

is used to eddy viscosity to model subgrid scale eddies. Dynamic procedure to evaluate model constant $C_s^2$ is similar to procedure used in (Tafti, 2005). Only positive values of $C_s^2$ are considered neglecting the back scattering effects and volume averaged local smoothening procedure is employed for smoother distribution of eddy viscosity to avoid numerical instability.

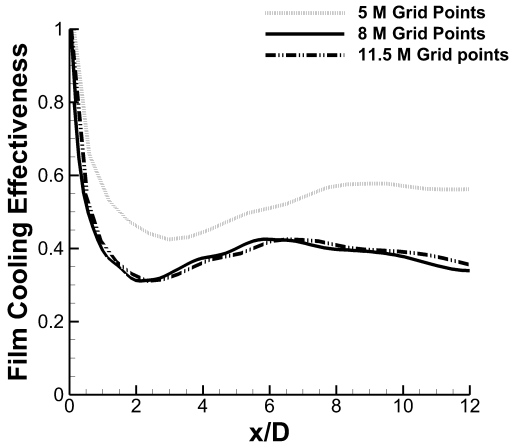


Figure 5.2: Grid independence

Final computational grid is chosen based on a grid independence study, where grid sizes from $5M - 11.5M$ are tested. Figure 5.2 shows the centerline adiabatic film cooling effectiveness for aforementioned mesh sizes. Grid independence is achieved at $8M$ grid points therefore this grid is used for final simulation. Mesh spacing parameters for final grid, near cooling wall were $y+ \approx 0.36$, $x+ \approx 5$ and $z+ \approx 11$ based on $\partial u/\partial y$ at a location $x/D = -1.0$. A adjacent cell height ratio of 1.4 was used in $y$ direction for grid clustering near wall film cooled wall.

A physical time step of $\Delta t U_\infty/D = 3.14 \times 10^{-3}$ is used which is smaller than Kolmogorov time scale $\Delta t_k U_\infty/D = 7.87 \times 10^{-3}$. The residuals at every time steps are allowed to fall by 2 orders of magnitude using 20 pseudo time steps. Courant, Friedrich and Levy $CFL$ of 0.6 is used based on smallest grid size. Simulation is run sufficiently to convect away all the initial transients over time period $(T_i U_\infty)/D = 60$ thereafter relevant statistics collected over a time period of $(T_{stat} U_\infty)/D = 120$ until they render steady.

### 5.3 Validation

Time averaged results from the simulation are compared with experiments conducted by Sinha et al. (1991). Figure 5.3 and 5.4 show agreement of streamwise and wall normal components of mean velocity RMS velocity with experimental data at measurement stations $x/D = 1.0, 3.0, 5.0$ and 10.0. The mean velocity at all the station show a typical shear layer profile formed by the low velocity jet and high velocity crossflow ($v_j/v_\infty = 0.5$). Distinct existence of shear layer is observed until $x/D = 5.0$ and considerable jet spreading until $x/D = 10.0$. The profile of turbulent fluctuations in streamwise and wall normal component show very good overall agreement except at $x/D = 1$ and $y/D > 0.5$. It should be noted that measurement station $x/D = 1.0$ is directly over the jet exit and influenced by the boundary layer turbulence of incoming crossflow and wake within the delivery tube. Attributed to the geometry, the advected wake turbulence from delivery tube influences turbulence levels below $y/D = 0.5$ resulting in elevated turbulence levels in agreement with experiments. Low levels of turbulence above $y/D = 0.5$ is attributed to lack of turbulent scales in crossflow boundary layer. No information of turbulent length, time scales and intensity was provided at the crossflow inlet as, very low levels ($< 1\%$) turbulent intensity was measured experimentally.

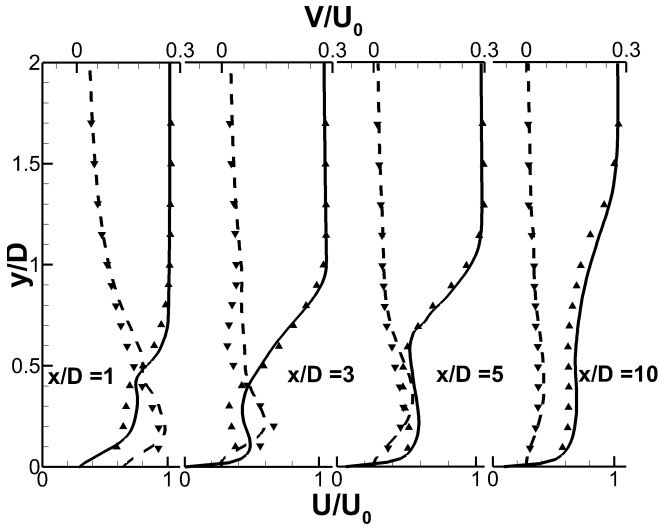


Figure 5.3: Mean velocity profiles ($\blacktriangle U/U_0(exp), \blacktriangledown V/U_0(exp)$), $-U/U_0(sim)$,- -$V/U_0(sim)$

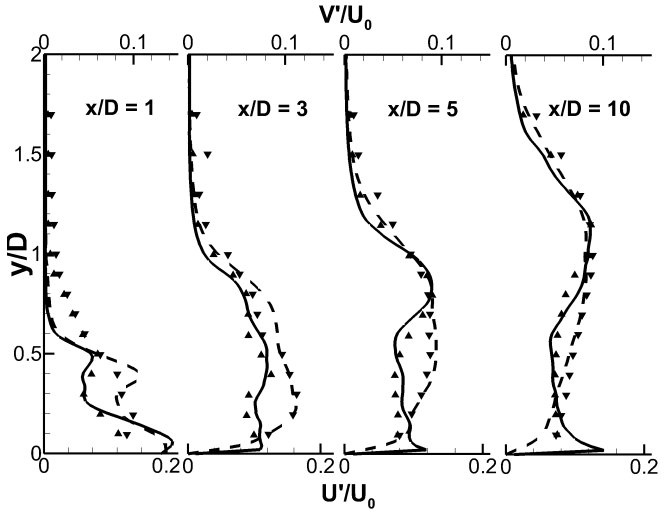


Figure 5.4: RMS velocity profiles
($\blacktriangle U'/U_0(exp), \blacktriangledown V'/U_0(exp)), -U'/U_0(sim), \text{- -}V'/U_0(sim)$

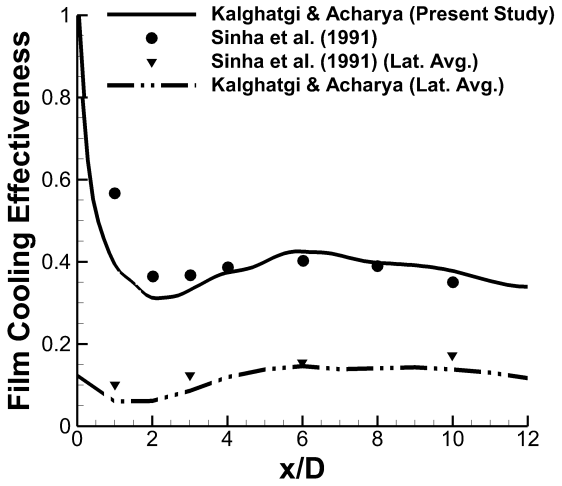


Figure 5.5: Validation of adiabatic film cooling effectiveness

It should be noted that non-specification of information of turbulence scales at the inlet not only negates the effect of incoming scales but also results in non-development of turbulence due to boundary layer instability. However, the contribution of inlet turbulence seems very marginal at downstream locations after $x = 1D$ as seen at other measurement station. Figure 5.5 shows the agreement of centerline and laterally averaged adiabatic film cooling effectiveness with experimentally measured data. The origin ($x/D = 0$) in this plot

is placed at trailing edge of the jet exit cross section. The centerline profile of adiabatic film cooling effectiveness show rapid decline until $x/D = 2.0$, a characteristic of jet liftoff. A partial re-attachment of jet after $x/D = 2.0$ results in marginal gain in adiabatic film cooling effectiveness until $x = 6.0D$ and steadily declines thereafter. Agreement between laterally averaged film cooling effectiveness leads to the conclusion that the spreading of the jet on the cooling wall was captured accurately.

### 5.4 Jet in Crossflow background

Fundamental configuration of film cooling flows is that of jets in crossflow (JICF). Study began as an investigation of chimney plumes (1932) and smoke dispersion from industrial smoke stacks. Later applications were developed in in later half of 1940s mainly for military applications of JICF, such as V/STOL, combustor cooling and thrust vectoring system. A summary of work before 1993 is presented by Margason (1993) in his famous paper 50 years of jet in crossflow research. Post 1993 a number of experimental and computational studies devoted for identifying dynamic mechanisms responsible for genesis of coherent structures in JICF. A representative list of such studies is, (Sykes et al., 1986; Andreopoulos and Rodi, 1984; Coelho and Hunt, 1989; Krothapalli et al., 1990; Fric and Roshko, 1994; Kelso and Smits, 1995; Kelso et al., 1996; Haven and Kurosaka, 1997; Yuan et al., 1999; Lim et al., 2001; Sau and Mahesh, 2008; Ilak et al., 2012). Collective focus of all these studies was on four basic flow structures viz. (i) counter rotating vortex pair (kidney pair), (ii) Kelvin-Helmholtz shear layer structures, (iii) horse shoe vortex and (iv) wake vortices (tornado like structures). These flow structures interact with another that give rise to a highly three dimensional flow and making conclusive observations a challenging task. As a result several theories about initiation mechanism of these structures were proposed. Although there is general consensus about multiple initiation mechanisms for all four fundamental vortical structures of JICF, the topic remains an active area of research.

In this monograph we study a particular application of an inclined JICF applied to film

cooling of gas turbine blades. The characteristic vortical structures and their initiation mechanism is investigated and put in perspective of fundamental flow physics investigations from literature to seek similarities and differences.

## 5.5 Flow physics of inclined jet film cooling flow with density variation

In this section we discuss coherent flow structures and the underlying mechanisms of inclined film cooling jet. A broader perspective of coherent structures in film cooling flow at an arbitrarily chosen time instant is provided in Figure 5.6(a) and (b). The flow structures are visualized with iso-surfaces of $\lambda_2 < 0$ due to Jeong and Hussain (1995) and contours of temperature. Similar to the observations of (Fric and Roshko, 1994), shear layer (Kelvin-Helmholtz) vortices, horse shoe vortex and hairpin vortex structures, counter rotating vortex pair (not seen in figure) are observed in the flow field. Tornado like wake vortices are not present as jet discharges coolant fluid in crossflow at an acute angle with the purpose of keeping it attached to the cooling wall.

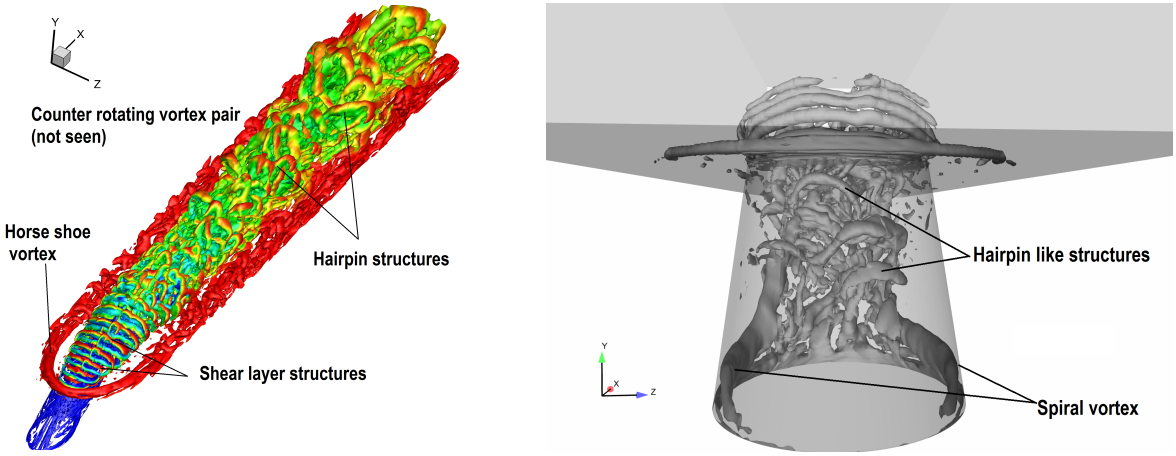


(a) (b)

Figure 5.6: Perspective of flow structures in film cooling flows

### 5.5.1 Horseshoe vortex structure

Horseshoe vortex structure in jet in crossflow configuration is similar to the usually encountered flow past a wall mounted bluff body. Figure 5.73 (a) and (b) show the horse shoe vortex visualized on spanwise plane of symmetry and by iso-surface of second eigen value $\lambda_2$ criterion, for an arbitrarily chosen time instant. Consistent with the observations made by Kelso and Smits (1995) a primary triple vortex system is seen upstream of the film cooling hole. This system is found to be steady, i.e. no significant oscillations leading to coalescence of triple vortex are observed as reported by Kelso and Smits (1995).

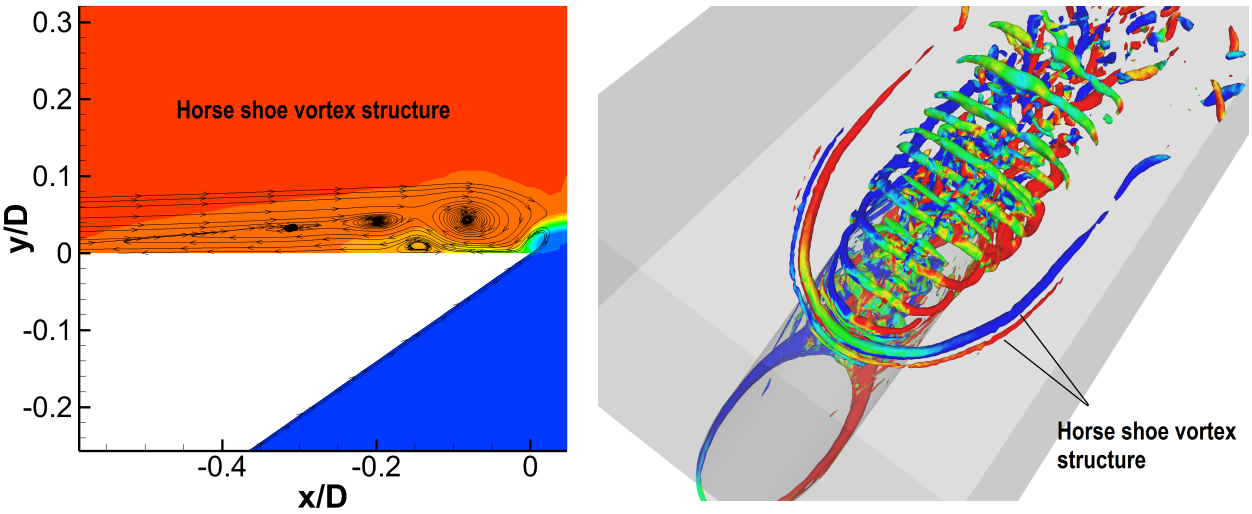


(a) (b)

Figure 5.7: Horseshoe vortex structure

However, the interaction of leading vortex of horse shoe vortex system and boundary layer from the delivery tube causes streamwise oscillations horse shoe vortex. The amplitude of this oscillation does not have impact on horse shoe vortex system to the extent where the topological changes are instigated. We discuss this interaction in detail in following section in context of shear layer vortices. Beside aforementioned role the effect of horseshoe vortex, no other significant interaction is observed in the flow field.

### 5.5.2 Shear layer vortices

Shear layer vortices are prominent vortical structures in jet in crossflow. Shear layer vortices are similar to ring vortex structures in free jets. Kelvin-Helmholtz mechanism is widely accepted as the mechanism responsible for genesis of these structures. Before we proceed with the analysis of shear layer structures in present case, an important distinction between present case and classically conducted jet in crossflow studies must be noted. Majority aforementioned JICF studies that investigated the coherent flow structures and mechanism of their genesis, conducted respective studies for velocity ratio greater than unity and density ratio of unity; the control parameter $r$ reduced to $(\rho_j V_j^2)/(\rho_\infty V_\infty^2) = V_j/V_\infty > 1$ for all of the studies.

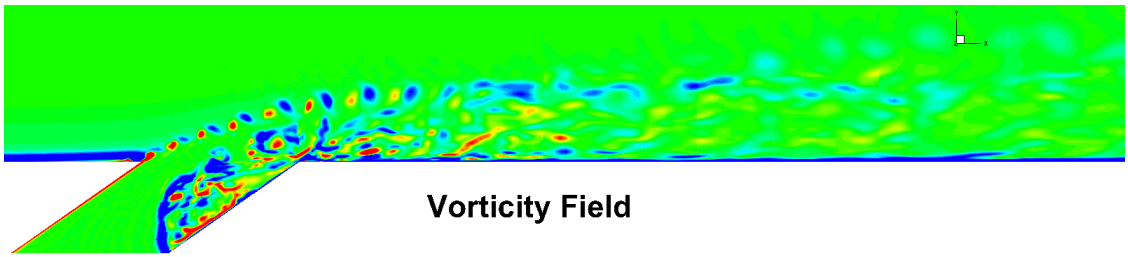


(a)

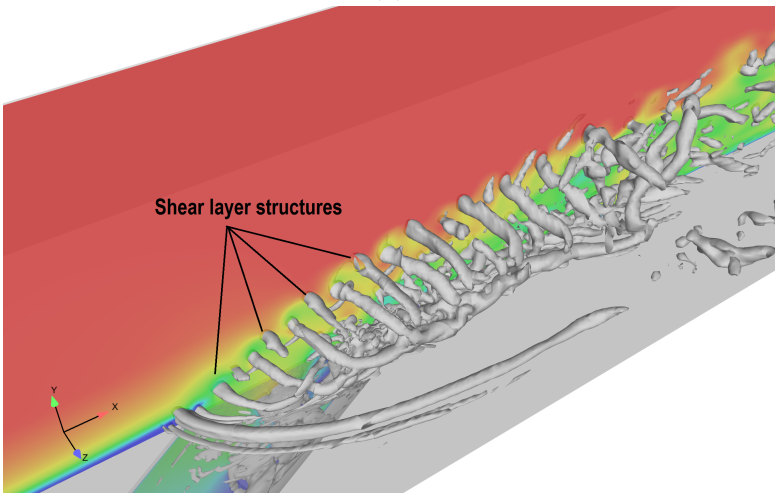


(b)

Figure 5.8: Shear layer flow structures

However, the present case scenario is a realistic condition for film cooling application

with blowing ratio $B.R. = (\rho_j V_j)/(\rho_\infty V_\infty) = 1.0$ as control parameter and density ratio $D.R. = \rho_j/\rho_\infty = 2.0$. This leads to a low velocity jet and high velocity crossflow ($V.R. = V_j/V_\infty = 0.5$) resulting in a windward shear layer has anti-parallel vorticity compared to JICF studies previously conducted with $V_j/V_\infty > 1$ and $\rho_j/\rho_\infty = 1.0$. This distinction cited further to explain dynamics of shear layer vortices in comparison with previous studies later in this section.

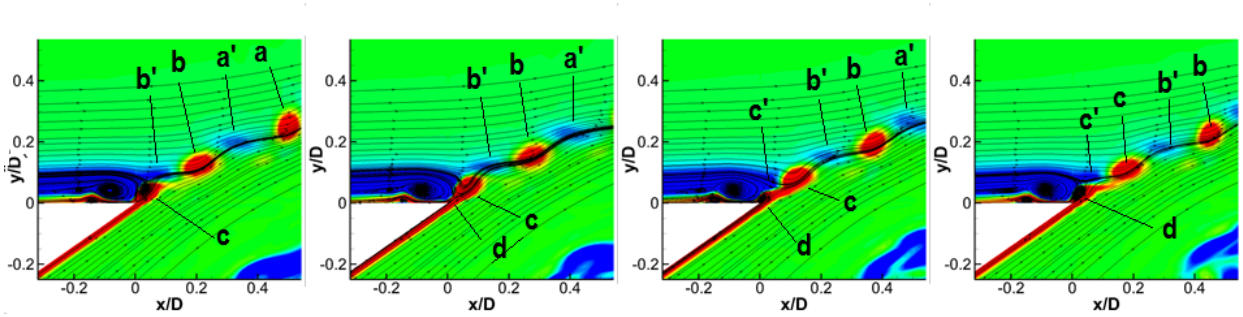


(a) Snapshot $\Delta t = 0.8\mu s$

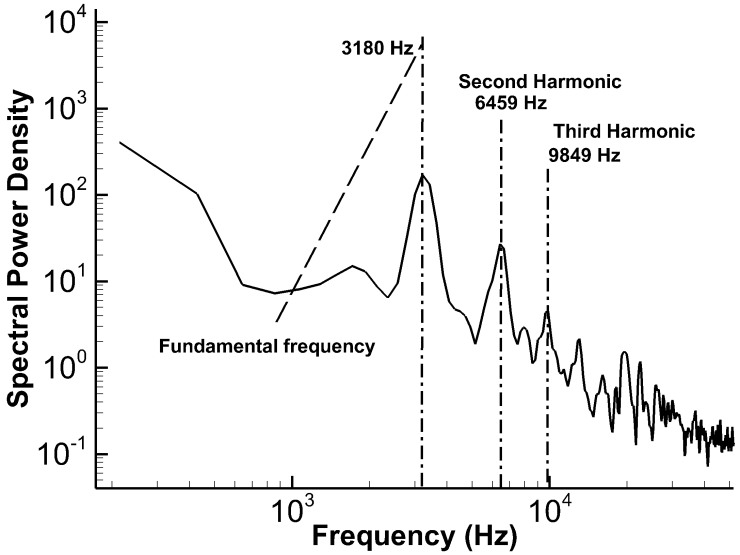


(b) Vortx shedding frequency

Figure 5.9: Karman type vortex shedding

Figure 5.8a shows the spanwise vorticity contours on the spanwise plane of symmetry. Discrete blobs of positively and negatively oriented vorticity are observed in the windward shear layer formed by jet and crossflow. A three dimensional perspective of shear layer

vortices visualized using $\lambda_2$ criterion and shear layer itself is visualized with streamwise velocity contours on the spanwise plane of symmetry (Figure 5.8b).

A closer view of the vortex initiation region of shear layer vortices is provided in Figure 5(a). Four snapshot provided are $0.8\mu s$ apart spanning over one complete frequency cycle of $3180Hz$. It is observed that the interaction between horseshoe vortex and vorticity from the boundary layer within delivery tube leads to a Karman type vortex shedding at upstream edge of film cooling hole, where discrete blobs of anti-clockwise (positive vorticity) vorticity are shed from boundary layer from delivery tube and clockwise (negative vorticity) vortices are shed from boundary layer vorticity of crossflow. The time scale of the shear layer vortices is determined using spectral decomposition of a single point velocity signal obtained at a location $(x/D = 0.1, y/D = 0.1, z/D = 0.0)$, in the immediate neighborhood of leading edge of film cooling hole (Figure 5.9b). Highest spectral energy is found at $3180Hz$ ($St_\theta = 0.125$, $\theta$ is momentum thickness at $x/D = -1.0$).

#### 5.5.2.1 Role of Kelvin-Helmholtz mechanism

The street of Karman like vortices shed is convected along the shear layer formed by the jet and crossflow. Orientation of these vortices and mean velocity profile of the shear layer at downstream edge of film cooling is shown in Figure 5.10a. It is interesting to observe that anti-clockwise vortices (positive vorticity) decay as they are convected along the shear layer while, clockwise vortices grow. The explanation to this observation is provided further.

In Kelvin Helmholtz mechanism the vorticity vector discrete rolled up are consistent with the direction of vorticity vector of the mean shear layer. Rollup of perturbed vorticity sheet in the shear layer starts on the side of high velocity stream and the direction is consistent with vorticity vector of the shear layer. Such a rollup process catastrophically form a discrete vortex form a continuous sheet of vorticity. Therefore, in an uncontaminated Kelvin-Helmholtz mechanism the direction of vorticity vector of all discrete vortical structures are identical. However in the present case, both positive and negative vortex blobs are observed due to

Karman type vortex shedding at the beginning of shear layer formation.

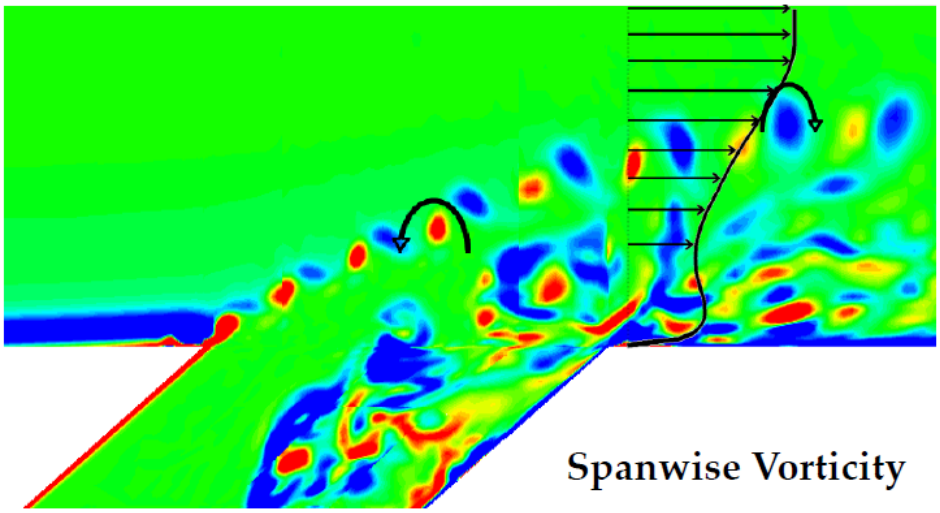


(a)

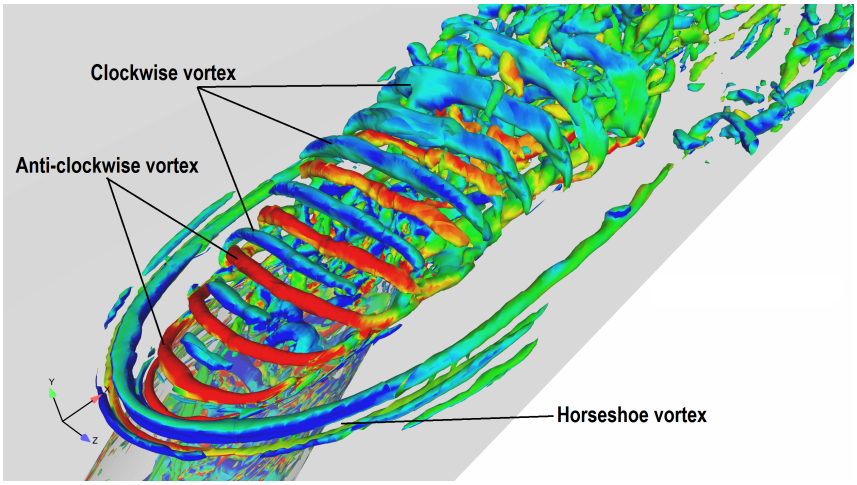


(b)

Figure 5.10: Growth and Decay of shear layer vortices

Due to anti-parallel orientation of vorticity with the mean shear layer, anti-clockwise vortex undergo a cancellation of vorticity hence decay progressively. This phenomenon along with Karman like shedding is a major distinction between present case shear layers and shear layers in classical jet in crossflow where only Kelvin-Helmholtz mechanism is dominant and cause of discrete roll up of identical vortical structure. Figure 5.10b shows the decay and growth of aforementioned vortical structures visualized in three dimensions.

### 5.5.3 Counter rotating vortex pair

Counter rotating vortex pairs (CRVP) are widely recognized and prominent feature of entire class of jets in crossflow. Upon formation CRVP grow in size and entrains large amount of crossflow fluid. Significantly higher mixing observed in jets in crossflow is attributed to counter rotating vortex pairs. Jet trajectory can be significantly influenced by controlling the characteristics of CRVP through shaped exits (Haven and Kurosaka, 1997) of jets and pulsation (Cortelezzi and Karagozian, 1999). For the same reason, role of CRVP is critical in film cooling applications since jet liftoff and crossflow entrainment can lead to significant degradation of film cooling performance. Although several initiation mechanisms are proposed for counter rotating vortex pair, three widely accepted. First was mechanism proposed by Sykes et al. (1986) and Kelso et al. (1996) through experimental study, attributes the initiation of CRVP to the alignment of leeward arms of shear layer vortices. In the purview of observations made by Kelso et al. (1996) evidence of an additional mechanism of hanging vortices was produced by Yuan et al. (1999) through computational study. They showed the shearing action of the jet and crossflow interface leads to formation of two vortex streaks on either side of jet that is rolled up inward on the lee-side of the jet. Third mechanism was proposed by Andreopoulos and Rodi (1984) and Haven and Kurosaka (1997) in which they proposed the initiation of CRVP is due to the realignment of side wall vorticity of the hole passage in the streamwise direction under the influence of crossflow. This view was proposed as early as in 1958 by Scorer (1958). However, it is interesting to note that the Kelvin-Helmholtz mechanism remains as a fundamental mechanism for hanging vortex initiation and shear layer vortices (ring vortex) as well that constitute first two of the proposed mechanisms.

In present case Figure 5.11a and 5.11b shows time averaged counter rotating vortex pair at $x/d = 1.78$ and $x/d = 4.78$ symmetrically placed around $z = 0$. Almost two fold increase in the size of CRVP is observed within streamwise distance of three hole diameters. Corresponding entrainment of crossflow fluid in the jet region is also evident in reduction of

jet core temperature and increase in jet width indicated by temperature contours. CRVP is attributed for majority of crossflow entrainments and lead to significantly higher mixing of jet and crossflow fluids.

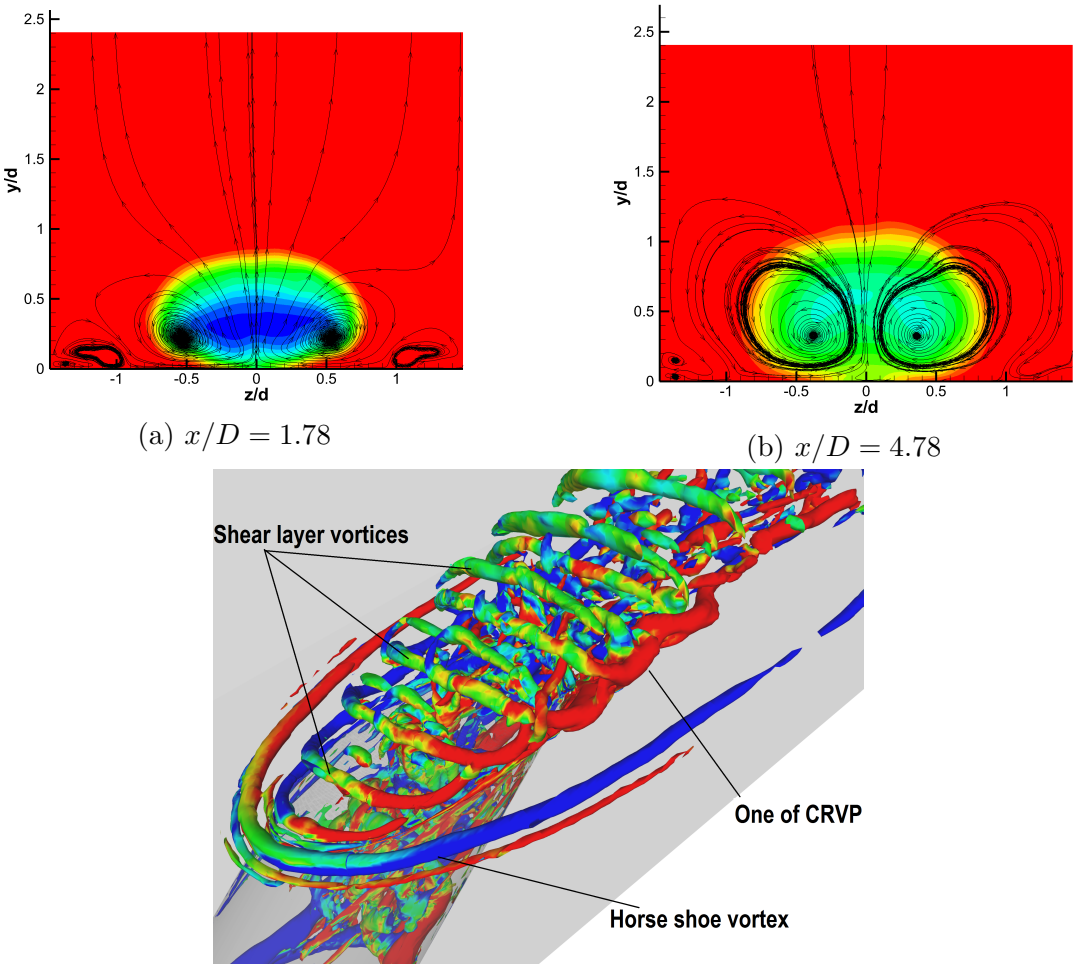


(a) $x/D = 1.78$

(b) $x/D = 4.78$

(c)

Figure 5.11: Structure of counter rotating vortex pair

It is observed that anti-clockwise vortex has arc like shape dictated by the hole shape (visible in Figure 5.10b) while clockwise vortex shed from crossflow boundary layer initiated at the upstream edge only. The side arms of the anti-clockwise vortex are swept in streamwise direction giving rise to counter rotating pair of vortices on either side of the jet. Anti-clockwise vortices are shed through Karman type vortex shedding is essentially the spillage of vorticity from the boundary layer within delivery tube over the edge of film cooling

hole. Further, through coalescence of discrete side arms of multiple anti-clockwise vortices strengthen the CVRP to from a continuous pair of counter rotating vortices in the near field region, downstream of film cooling hole. These observations are consistent with CRVP initiation mechanisms proposed by Haven and Kurosaka (1997).

### 5.5.4 Other mechanisms contributing to CRVP

#### 5.5.4.1 Flow field inside delivery tube

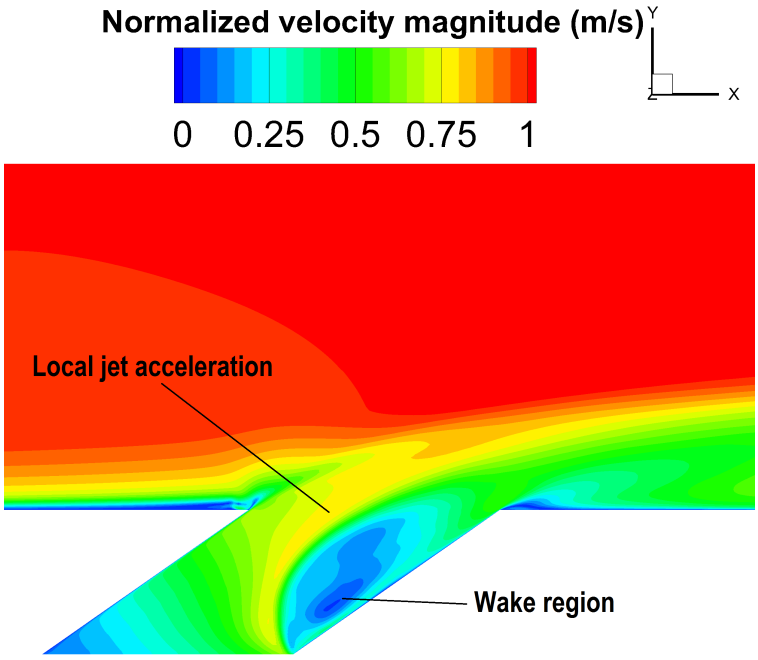


Figure 5.12: Velocity field in delivery tube

Flow field in delivery tube is of particular importance in film cooling flows where an inclined jet is fed by a plenum. Figure 5.12 shows the velocity field inside the delivery tube. As coolant fluid enters delivery tube in a direction normal to cooling wall (positive direction of y-axis), flow separates to form a wake region on leeward side and locally accelerates on the windward side.

The length of delivery tube also plays an important role in determining the jet trajectory. (Sinha et al., 1991) showed for same mass flux ratio, low aspect ratio delivery tube enhances

jet liftoff behavior due to local jet acceleration on windward side of the jet causes high local momentum ratio and increased jet penetration. This behavior can lead to significant loss of film cooling performance, particularly in near hole field.

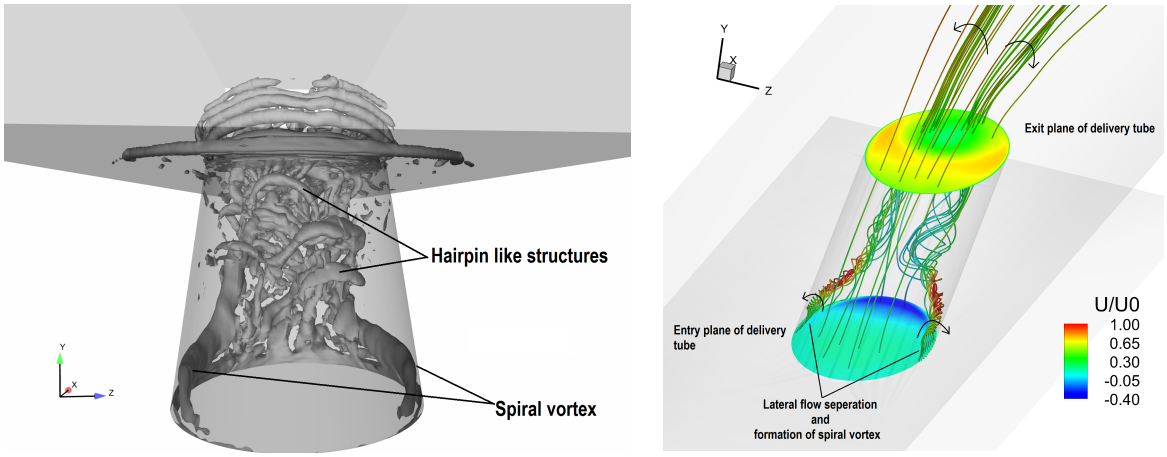


(a) (b)

Figure 5.13: Flow field inside delivery tube

Instantaneous vortical structures visualized inside delivery tube are shown in Figure 5.13. Two types vortical structures are observed in wake region, (*i*) Spiral vortices at the spanwise lateral edge of delivery tube entrance, (*ii*) Hairpin type flow structures riding atop spiral structures. Spiral structures originate through flow separation at lateral edge of delivery tube entrance and get swept throughout the length of delivery tube. Wake region and local jet acceleration is evident through velocity distribution on exit plane of delivery tube as shown in Figure 5.13b. Also the bundles of streamlines originating from each spiral vortex remain distinct even after the jet exits in the crossflow. Orientation of vorticity in spiral vortices is consistent with the counter rotating vortex pair and advected vorticity from spiral vortices merge with CRVP originated from boundary layer vorticity from delivery tube edge as shown by visualizing time averaged flow structures in Figure 5.14.

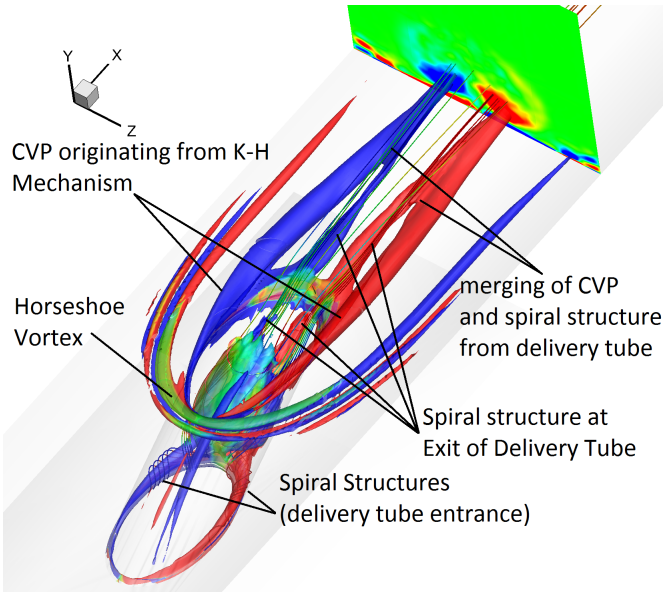


Figure 5.14: Time averaged flow structures in delivery tube

#### 5.5.4.2 Hairpin vortices: Interaction of Anti-clockwise and clockwise shear layer vortices

Hairpin vortex structures are characteristic of jet in crossflow and largely studied in the perspective of film cooling flows. This is due to the fact that hairpin vortices are prominent at low momentum ratios that are customary to film cooling applications. Ilak et al. (2012) through stability analysis established that hairpin vortices are consequences of instability of jet shear layer downstream of the jet at velocity ratio r=0.675 with a limit cycle characteristic of Hopf bifurcation. Formation of hairpin vortex was investigated at velocity ratio r=1.0 by Sau and Mahesh (2008). Both studies were conducted for vertical jets at low Reynolds number, showed the hairpin vortices arise through instability of leeward shear layer downstream of film cooling hole. The mechanism of hairpin vortex formation is given based on the fact that vorticity cancellation of the windward side jet shear layer by opposite vorticity imposed by crossflow boundary layer. This leads to formation of incomplete vortex ring which is advected as hairpin vortex (Sau and Mahesh, 2008).

In the present case of inclined jet the phenomenon of vorticity cancellation is completely

absent and additionally leeward shear layer is replaced by a complex wake structure from delivery tube. The vortex shedding phenomenon from upstream edge of film cooling hole sheds both anti-clockwise and clockwise vortices as discussed previously and shown in Figure 5.10b. However, as the both type vortices are convected downstream, clockwise vortex grow in spanwise direction to form an arc like shape.

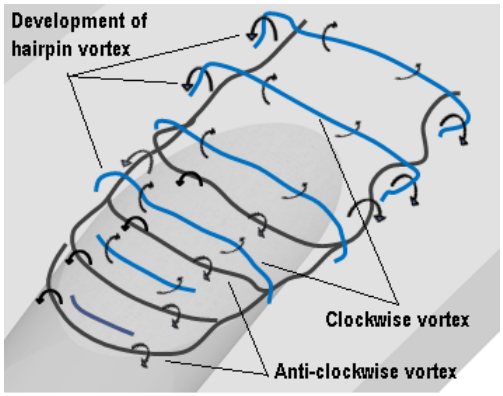


(a)

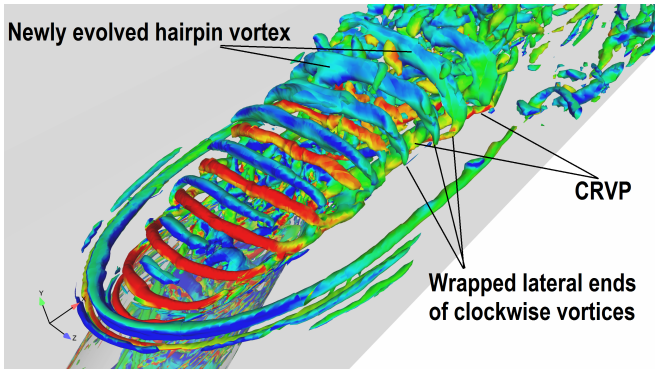


(b)

Figure 5.15: Evolution of hairpin vortex

Figure 5.15a shows the schematic of evolution of hairpin vortices. As clockwise vortices feeds on shear layer vorticity they grow in spanwise direction and approximately assume jet curvature. During this development, the lateral edges of clockwise vortices wrap onto counter rotating vortex pair formed by lateral swept arms of anti-clockwise vortices. At this stage the head of the clockwise vortex is advected at the mean streamwise velocity of the windward shear layer, however, the later ends lag due to their vicinity to the wall and resulting low advection rate. This leads to reorientation of lateral ends of clockwise vorticity

in the streamwise direction parallel to vorticity of counter rotating vortex pair resulting in formation of hairpin vortex. Figure 5.15b clearly shows evolution of such a hairpin vortex.

## 5.6 3D Visualization of flow structures

Figures in this section are anaglyph 3D images of flow structures for vided for clearer visualization of flow structure topology and their relative placement in three dimensional space. The images can be viewed in easily available Cyan-Red anaglyph 3D goggles.

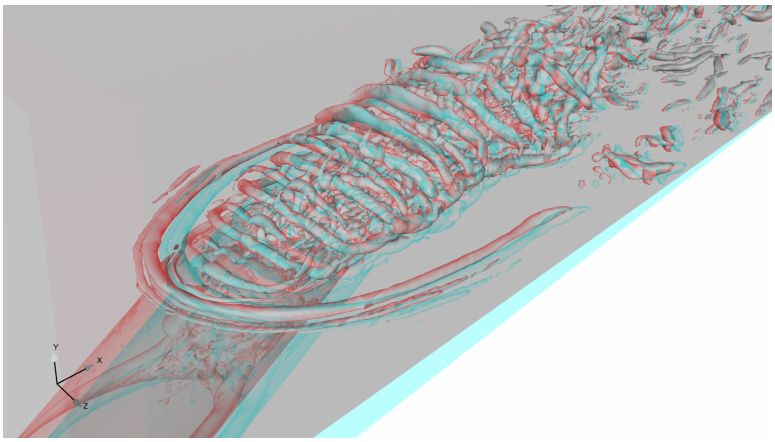

Figure 5.16: Shear layer vortical structures

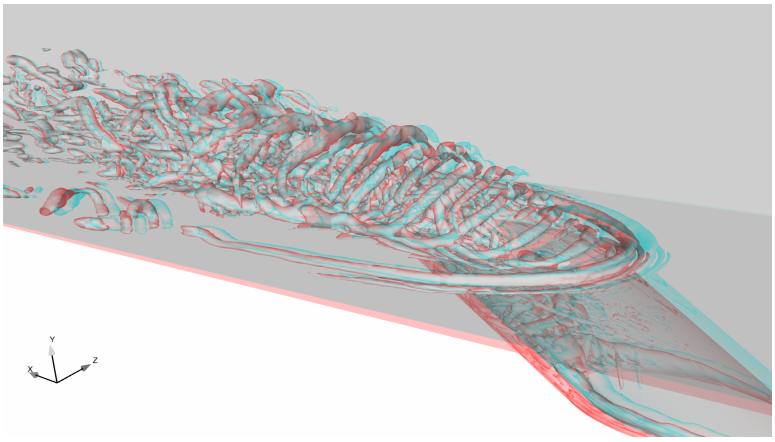

Figure 5.17: Shear layer vortices and CRVP

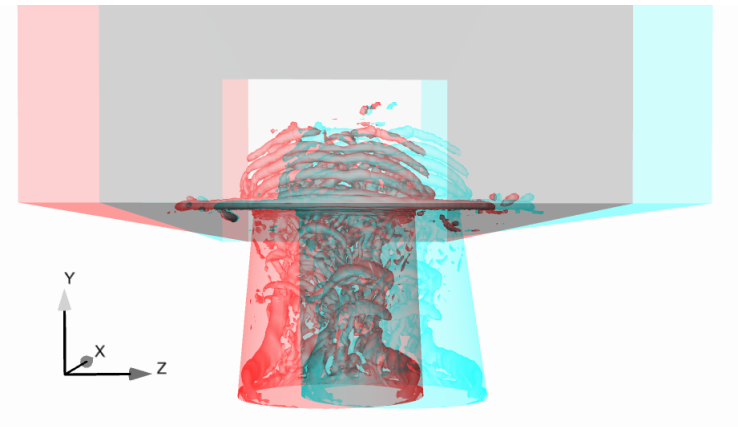


Figure 5.18: Flow structures inside delivery tube

## 5.7 Conclusion

Modal analysis of LES results for an inclined film cooling jet are undertaken for Reynolds number, $Re = 16000$, $l/D = 1.75$, $B.R. = 1.0$ and $D.R. = 2.0$. Excellent agreement between experimental and simulation results are obtained for both the hydrodynamic (first and second order quantities) and thermal (film cooling effectiveness) data. The evolution of the Kelvin-Helmholtz vortices, the origin and mechanisms associated with the counter rotating vortex pair and the transition of the Kelvin-Helmholtz vortices to hairpin vortices is investigated through extensive flow visualization.

# Chapter 6
# Modal Analysis of Inclined Jet Film Cooling Flows with Density Variation

**Abstract**

Dynamic Mode Decomposition (DMD) technique. The modal frequencies are identified, and the specific modal contribution towards the cooling wall temperature fluctuation is estimated on the film cooling wall. The low and intermediate frequency modes associated with streamwise and hairpin flow structures are found to have the largest contribution (in-excess of 28%) towards the wall temperature (or cooling effectiveness) fluctuations. The high frequency Kelvin-Helmholtz mode contributes towards initial mixing in the region of film cooling hole away from the wall. The individual modal temperature fluctuations on the wall and their corresponding hydrodynamic flow structures are presented and discussed. Modal analysis is conducted using the data obtained by LES simulation described in Chapter 5.

## 6.1 Modal Analysis

The analysis of the large data sets emerging from DNS and LES, and the understanding of the complex dynamical features present unique challenges. Modal analysis provides a more quantitative description of the larger dynamical flow structures, and the flow physics can be understood through the corresponding low-dimensional representation enabled by the modal analysis. For example, Proper Orthogonal Decomposition (POD) (Berkooz et al.,

1993; Lumley, 1970) techniques have been commonly employed to study turbulent flows (Berkooz et al., 1993; Meyer et al., 2007). However, POD suffers from loss of dynamical information when the auto-correlation matrix (second order statistics) is constructed and the energetic modes may not provide a sufficient criterion for the low-dimensional representation (Schmidt, 2010) of the flow. The Dynamic Mode Decomposition (Schmidt, 2010) approach yields information about all the flow modes and their growth rates akin to the stability analysis approaches in simplified flows. It should be noted that (Bagheri et al., 2009) are amongst the only ones who have used the DMD approach to understand the behavior of the dynamically significant modes in a JICF. They have however focused their attention on a vertical JICF with jet to crossflow velocity ratio of 3.0 and investigated the global modes exhibiting self-sustained oscillations. No studies using DMD have been reported for a realistic film cooling configuration of an inclined jet. Such an analysis will allow us to understand the role of the different modes on the development of the various flow features and on the surface temperature distributions in a film cooling jet. In the present study we use the DMD approach to conduct a modal analysis of film cooling flow data obtained from LES of an inclined round film cooling jet over a flat surface. Results are obtained for a realistic Reynolds number of 16000 based on the coolant hole diameter. The goal is to identify the key flow modes that influence the surface temperature or cooling effectiveness, and the dynamics associated with these modes. This paper represents the first effort at a modal analysis of an inclined film cooling jet, and is the first comprehensive study that combines both the hydrodynamic and thermal fields.

## 6.2 DMD-Algorithm

A brief over view of DMD algorithm is provided in this section. Dynamic mode decomposition was first proposed by Schmid and Sesterhenn (2009) and Schmidt (2010). It has been applied to jet in crossflow, (Bagheri, 2010), turbulent flow over a square cavity (Seena and Sung, 2011). A comprehensive account of theory and various application may be found in (Chen

et al., 2012). In this monograph we use the algorithm proposed reported in (Bagheri, 2010). Typically in any of the aforementioned algorithms total of N snapshots of complete three dimensional flow field over the region of interest are collected at regular time interval $\Delta$t are arranged in matrix form $V_1^{N-1}$ and $V_2^N$,

$$V_1^{N-1} = \{v_1, v_2, ..., v_{N-1}\}$$

$$V_2^N = \{v_2, v_3, ..., v_N\}$$

where $v_i$ a column vector representing is i$^{\text{th}}$ snapshot. The number $N$ is large enough, such that the $N^{\text{th}}$ snapshot can be represented as a linear combination of preceding $N-1$ snapshots.

$$v_N = c_1 v_1 + \ + c_{N-1} v_{N-1} + r \tag{6.1}$$

Similarly, if a matrix operator $A$ is devised such that,

$$v_{i+1} = A v_i \tag{6.2}$$

$$AV_1^{N-1} = \{Av_1, A^2 v_1, , A^{N-1} v_1\} = V_2^N \tag{6.3}$$

then, $A$ would be equivalent to the coefficient matrix operator formed of governing equations that governs the spatio-temporal evolution of field variables. Therefore, the Eigen values of A would provide the characteristic information of the system. However, formulation of such an operator is computationally demanding. Recent works of (spectral paper and global stability) using Koopman mode analysis based on Arnoldi type algorithm used a similar method for stability analysis of the flow. In (Bagheri, 2010) an alternative approach is used to form a companion matrix from coefficient of linear combination in Eq. 6.1 and use the fact that $V_1^{N-1}$ and $V_2^N$ differ by only $N^{\text{th}}$ snapshot. Hence writing Eq. 6.3 in the

following form,

$$V_2^N = AV_1^{N-1} = V_1^{N-1}C + I_r \tag{6.4}$$

and $c_i$ are arranged as companion matrix $C$,

$$C = \begin{bmatrix} 0 & & \dots & 0 & c_1 \\ 1 & \ddots & & \vdots & c_2 \\ 0 & \ddots & \ddots & & \vdots \\ \vdots & & 1 & 0 & c_{N-2} \\ 0 & \dots & 0 & 1 & c_{N-1} \end{bmatrix} \tag{6.5}$$

The properties of $C$ now are equivalent to that of $A$ and therefore the eigen values of $C$ would contain the characteristic information of the underlying dynamic system represented by the ensemble of snapshots. Dynamic modes are then the projection of the instantaneous flow field onto the basis (Eigen vectors) of C. The growth rate and frequency of a dynamic mode are given as real and imaginary values of $\lambda_i = (\log \sigma_i)/(\Delta t)$. Positive and negative growth rates indicate the growing and decaying modes in the flow field with their corresponding angular frequencies. Thus, DMD procedure enables to conduct eigenvalue analysis by constructing a companion matrix $C$ the Eigen values and Eigen vectors that are equivalent to eigen values and eigen vectors of $A$, avoiding the reconstruction of entire system matrix.

### 6.3 DMD Analysis

DMD analysis of velocity and temperature field is conducted simultaneously. As the flow is convection dominant effect of thermal diffusion are minimal as indicated by high Peclet number $Re_D Pr = 14400$, the spectral characteristics of temperature field is closely related to that of velocity field. A single point time series signal of streamwise velocity and temperature field is obtained at a location $(x/D = 0.1, y/D = 0.1, z/D = 0.0)$. Corresponding spectral decomposition of temperature and velocity signal is shown in Figure 6.1. Highest dominant

frequency of $3180Hz$ and subsequent second and third harmonics at $6459Hz$ and $9849Hz$ is observed in both temperature and velocity spectra. Spectral information obtained is used for deciding temporal spacing between consecutive snapshots in accordance with Nyquist criterion (Schmidt, 2010) and validating the spectral information obtained from DMD analysis. The sub-domain used for DMD analysis shown in Figure 6.2 extends $-2.4 \leq x/D \leq 15$

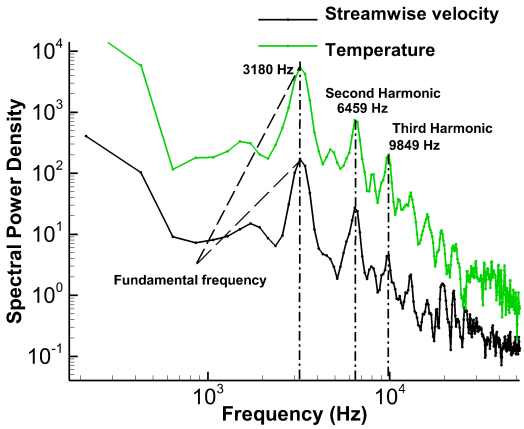


Figure 6.1: Spectral power density of streamwise velocity and temperature at $(x/D = 0.1, y/D = 0.1, z/D = 0.0)$

in streamwise direction, $0 \leq y/D \leq 2.3$ in wall normal direction and covers entire spanwise direction $-1.5 \leq z/D \leq 1.5$. Total of 100 snapshots are collected over 0.5 flow through time period ($\approx$ 2000 physical time steps) at time interval of $\Delta t = 4 \times 10^{-5}s$. Eigen values of dominant modes were found steady and had no-impact after considering additional snapshots beyond 100. Convergence criterion for evaluation of Ritz values Ritz vectors set to $e_R \leq 1.0 \times 10^{-5}$ for each Eigen mode. Two distinct ranking criterion may be chosen for ranking of DMD modes. First and unique to DMD technique is the growth rate information of the modes and second by evaluating the energy content of the modes as evaluated by second norm of individual mode $\|DM_i\|_2$. Frequency content of individual modes may be used as the independent variable in each of the cases mentioned before. Second criterion provides additional flexibility of evaluating energy content of modes in restricted spatial regions to evaluate local dominance of the modes. This information may be valuable for evaluation of modal contribution to a localized phenomenon.

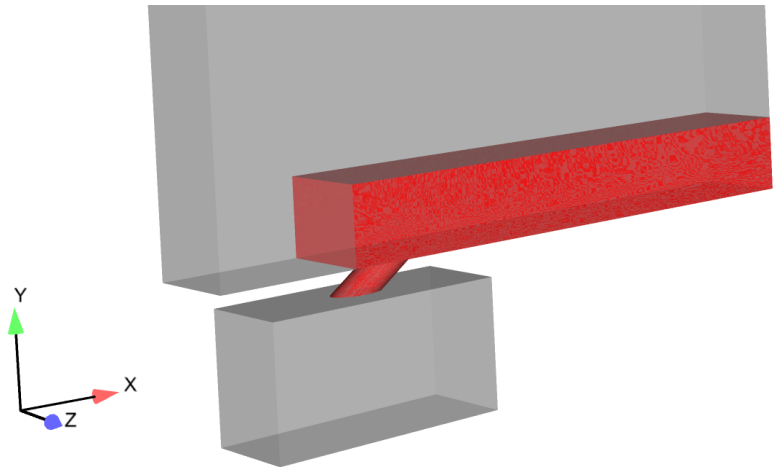


Figure 6.2: DMD-Domain D(shown in red)

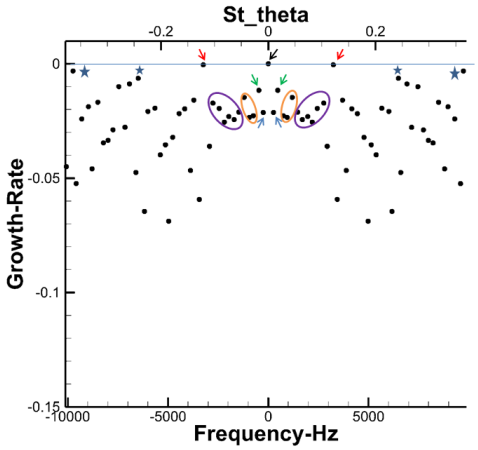


Figure 6.3: DMD-growth spectra

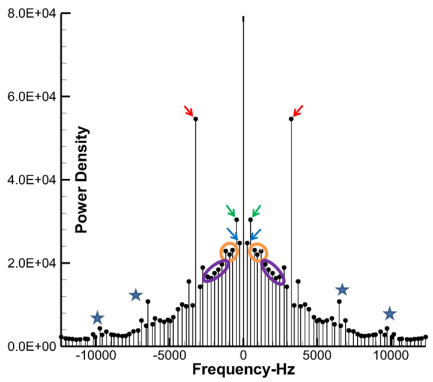


(a)

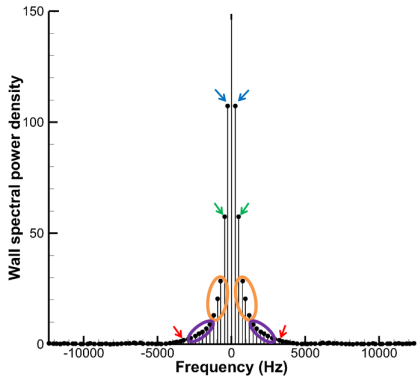


(b)

Figure 6.4: DMD spectral power distribution (a)$\|DM_i\|_2 \forall$ D (b) $\|DM_i\|_2 \forall$ cooling wall

Following this idea, we rank the extracted DMD modes of temperature fluctuation according to (*i*)growth rate, (*ii*) spectral power density on entire domain and (*iii*) spectral power density only on film cooling wall. This enables to determine dynamically significant modes, most energetic modes over entire domain and modes contributing to wall temperature fluctuation. Figure 6.3 shows the the growth rate of various modes at discrete frequencies. The centrally located zero frequency and zero growth rate mode corresponds to the mean flow field based on the snapshots used for modal decomposition. The mode with highest growth rate is found at $3180Hz$ corresponds to fundamental frequency of shear layer mode observed in spectral decomposition of a single point velocity signal mentioned earlier. Second and third harmonics of shear layer found at $6455Hz$ and $9849Hz$ (marked $\star$) have highest growth rate after the fundamental mode. Other modes that are marked/grouped are ranked according to their spectral power density and discussed next.

Figure 6.4a shows the spectral power distribution of temperature modes over entire domain $D$ and only on cooling wall Figure 6.4b respectively. Shear layer structures at $3180Hz$ are found to have highest power spectral density among all modes over the entire domain marked in red arrow. Second and third harmonics (marked $\star$) although have distinct energy levels in the respective frequency neighborhood, contain small fraction of energy relative to the low frequency modes distinctly marked in Figure 6.4a. However, the spectral energy distribution on film cooling wall shown in Figure 6.4b indicates, the shear layer structures have minimal influence on the temperature fluctuations on film cooling wall as they contain negligible energy. The most energetic modes on film cooling wall are the low frequency modes and the energy content decays exponentially as frequency increases. Frequency content of the marked modes is provided in Table 7.1.

Table 6.1: Mode tag and frequency

| Mode Tag | Frequency ($Hz$) |
|---|---|
| Blue ArrowB | 258 |
| Green Arrow (G) | 465 |
| Orange Circle-1 (O-1) | 750 |
| Orange Circle-2 (O-2) | 942 |
| Orange Circle-3 (O-3) | 1208 |
| Purple Circle -1 (P-1) | 1474 |
| Purple Circle -2 (P-2) | 1707 |
| Purple Circle -3 (P-3) | 1973 |
| Purple Circle -4 (P-4) | 2191 |
| Purple Circle -5 (P-5) | 2448 |
| Purple Circle -6 (P-6) | 2762 |
| Red Arrow (R) | 3180 |

Before we focus on the modal contributions towards temperature fluctuation on cooling wall, we take note of topological nature of the selected modes to emphasize the nature of coherent structures of various modes. This will enable to describe a complete picture of modal contributions and underlying mechanisms of temperature fluctuation on film cooling wall. Figure 6.5 show the topology of selected modes. Low frequency modes in Figure 6.5a ($258Hz$) and Figure 6.5b ($465Hz$) show streamwise structures pertaining to CRVP structures. It should be noted that, due to high Reynolds number flow, in instantaneous sense CRVP in far field location from film cooling hole does not exist as a single large structure. Instead, it is made up of numerous small streamwise vortices that are discrete in streamwise direction and appear to be chaotic in nature. At higher frequency a transition from streamwise structures to hairpin like structures is observed in Figure 6.5c ($1707Hz$). At highest dominant frequency shear layer structures are observed. A comparison of Figure

6.5c and Figure 6.5d indicates the near hole region is dominated by shear layer structures and further downstream the evolution of hairpin structures dominate the flow field.

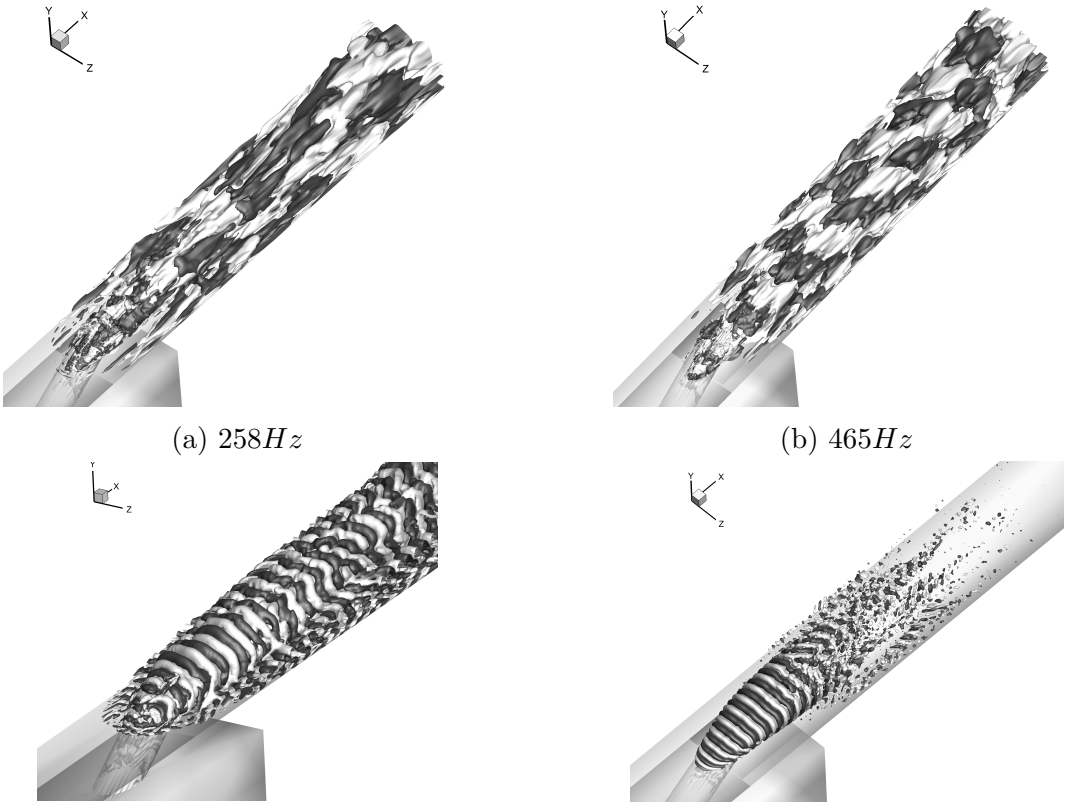

(a) $258Hz$ (b) $465Hz$

(c) $1707Hz$ (d) $3180Hz$

Figure 6.5: Topological structures of selected DMD modes

Figure 6.6 shows the modal temperature variation on film cooling wall surface due to few selected DMD modes. The scale represents non-dimensional temperature $\eta$ (film cooling effectiveness); contour levels are adjusted for clarity. Note that modal decomposition is akin to triple decomposition of the fluctuating field with each mode representing the periodic process of a discrete frequency. The detailed discussion is provided in appendix. The second norm $||DM_i(x,y,z)|| \equiv |DM_i(x,y,z)|$ is the local amplitude of $i^{th}$ mode akin to the Fourier amplitude (mean subtracted DMD is equivalent to discrete Fourier transform Chen et al. (2012)).

Considering the levels of temperature fluctuations on film cooling wall, the cooling region is divided in two categories, $(i) 0 \leq x/D \leq 3D$ and $(ii) x/D > 3D$. First region witness a

rapid decline in film cooling effectiveness due to jet lift off and experiences high degree of unsteadiness in cooling wall temperature. A high modal contribution of modes over a wide range of frequencies is observed in this region. The second region however, has source of temperature variation largely in low and intermediate frequency modes. In order to put forth a perspective in the discussion, the percentage modal variation in temperature, reported henceforth, is calculated with reference value of $\eta = 0.4$. This value corresponds to maximum mean film cooling effectiveness in downstream region of film cooling hole beyond the initial jet liftoff region.

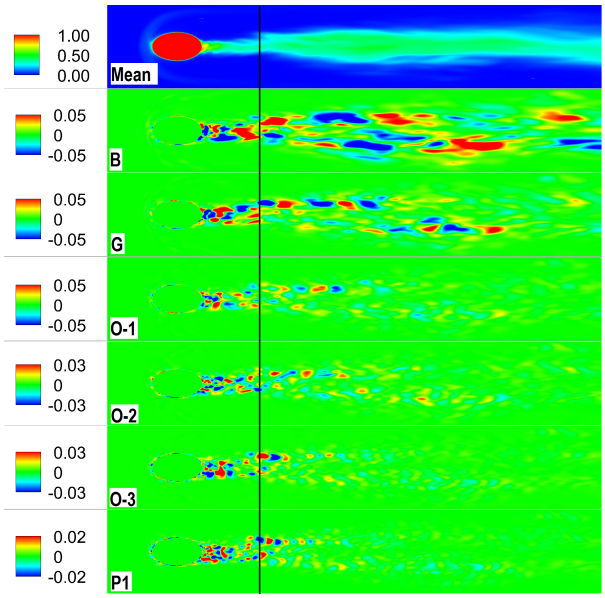


Figure 6.6: Modal contribution to wall temperature fluctuation

On over all film cooling region the largest fluctuation of temperature ($\approx$ 37%) about mean value is caused due to low frequency modes $B$ and $G$. The topological structure visualized for mode $B$ indicates corresponds CRVP structures. Intermediate modes $O$-2, $O$-3 and $P$-1 contribute about $\approx$ 28% variation of temperature over film cooling wall. These modes are associated with hairpin type flow structures shown in Figure 6.5c. Shear layer modes has direct contribution of $\leq 5\%$ toward wall temperature variation. CRVP enhances jet and crossflow mixing by entrainment and draws crossflow fluid directly under the jet. The fluctuations are dominant at the spanwise edge of the cooled area of the wall indicat-

ing unsteadiness associated with crossflow entrainment associated with CRVP and hairpin structures consistent with the mixing front formed due to entrainment.

## 6.4 Modal reconstruction and time stepping

Low dimensional reconstruction of the flow field from DMD modes may be done with following expression (Chen et al., 2012),

$$v_j = \sum_{i=1}^{m} \sigma_i^j DM_i \tag{6.6}$$

where $m = N - 1$ is number of extracted modes from $N$ snapshots used for DMD. $\sigma_i$ and $DM_i$ are $i^{th}$ Ritz value and Ritz vector. A reduced order representation may be constructed using only a subset of extracted modes $m < N - 1$. Additionally, this expression allows to generate the instantaneous flow/temperature field at arbitrary time instant. The reduced order representation may also be constructed by considering single or selected modes to evaluate instantaneous contribution to fluctuations that can be advanced through time (equation 6.6). Employing this technique to generate instantaneous snapshots, a complete reconstruction of the temperature field is done considering all 99 modes extracted. Figure 6.7 shows the comparison of centerline and laterally averaged film cooling effectiveness obtained from time averaged results of simulation and reconstructed from DMD modes.

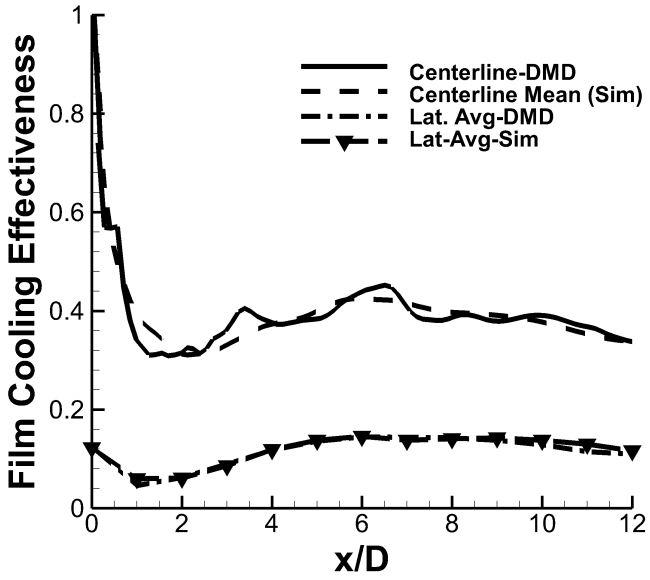


Figure 6.7: Verification of reconstruction of DMD

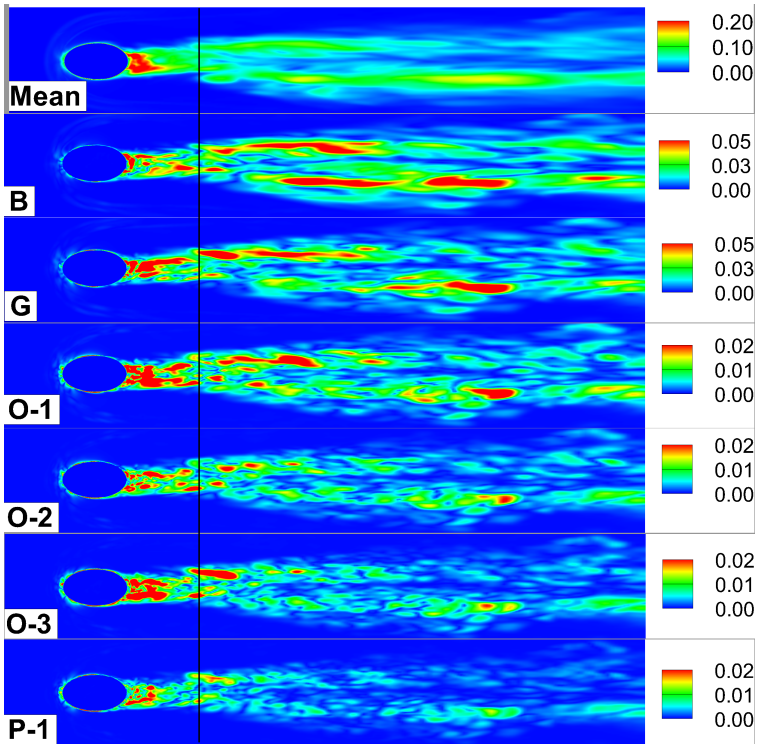


Figure 6.8: RMS of Modal temperature fluctuation

Figure 6.8 shows RMS of the modal temperature fluctuations in comparison with the mean obtained over identical set of snapshots used for modal decomposition. Maximum

variation in the range of 35%-40% is seen in region before $x/D \leq 3.0$ for mode $B$, $G$ and $O$-1. In the region beyond $x = 3D$ the RMS values are of the order of 16% to 18% for modes $B$ and $G$. 5% to 8% RMS is observed for modes $O$-1, $O$-2, $O$-3 and $P$-1.

## 6.5 Conclusion

The modal analysis is conducted using the dynamic mode decomposition (DMD) technique. The modal contributions towards the wall temperature fluctuation is calculated using the $2^{nd}$ norm of the various modes on the film cooled wall. The low frequency, predominantly streamwise oriented modes are found to contribute more towards wall temperature (cooling effectiveness) fluctuation. Of these, the modes B ($258Hz$) and G ($465Hz$ corresponding to the CVP) are found to be active over the entire span of film cooled area with a maximum of 16% contribution to film cooling effectiveness variations beyond $x/D = 2$, and these fluctuations increase to nearly 35% near the film cooling hole. These modes are attributed to the CVP (mode G) and near wall streamwise structures (mode B). The 'O' and 'P' modal contributions (750 Hz-2762 Hz) are found to contribute in the range of (RMS) 5% - 8% towards film cooling effectiveness, The contributions diminish with increasing frequency with the highest frequency K-H mode contributing only in the immediate vicinity of the film-cooling hole. Hairpin type flow structures are associated with modes at multiple frequencies. The modal analysis is also shown to capture the evolution of CVP in the near hole region and the transition of clockwise K-H vortices to hairpin like structures.

# Chapter 7
# Mixing characteristics of Inclined Jet in Crossflow

**Abstract**

General mixing chartacteristics and modal analysis of macro (resolved) and micro (subgrid) scale scalar dissipation rates in an inclined low temperature jet in crossflow are studied using large eddy simulation (LES) data. An inclined JICF is setup with a short delivery tube with aspect ratio $l/D = 1.75$ and 35° jet inclination, conducive to film cooling application. LES is performed for free stream Reynolds number $Re_D = 16000$, blowing ratio $B.R. = (\rho_j V_j)/(\rho_\infty V_\infty) = 1.0$ and density ratio $\rho_j/\rho_\infty = 2.0$. Simulation results are validated with experimental data in literature for hydrodynamic flow and thermal field. General mixing characteristics of cold and hot fluid streams are discussed using jet centerline decay of scalar concentration, crossflow entrainment, resolved and subgrid scalar dissipation rates. Further, modal analysis of macro and micro scale scalar dissipation rate (SDR) is conducted using Dynamic Mode Decomposition to reveal the role of individual modes in mixing process. Streamwise variation of modal energy is computed for selected SDR modes. The formation of shear layer vortices is associated with highest SDR over the jet region till $x/D \approx 3.0$ and decay thereafter. Counter rotating vortex pair and hairpin vortices dominate SDR further downstream region beyond $x/D \approx 3.0$.

## 7.1 Introduction

Jets in cross flow (JICF) are central to numerous engineering applications such as film cooling of turbine blades, air-fuel pre-mixers / fuel injection in air-breathing engines, dilution holes of turbine combustors, V/STOL aircrafts, and pollution dispersion from chimney stacks. Mixing of jet and crossflow fluids and jet trajectory are of interest in a typical JICF application. Application specific objective of JICF may vary from attenuating to enhancing mixing along with jet trajectory control e.g. air-fuel pre-mixers vs. film cooling jets. Mixing of smoke plumes and pollutant dispersion from chimney stacks are first reported jet in cross flow study dated back to (Sutton, 1932; Bosanquet and Pearson, 1936). Predicting flow patterns and correlation for pollutant dispersion away from chimney stacks was primary objective of the study. A comprehensive review of jets in cross flow work until early 1990s is found in (Margason, 1993). A number of studies are devoted to dynamical and structural investigations of the jet in crossflow to reveal the mechanism of origin and evolution of coherent structures in a typical vertical jet in crossflow,(Andreopoulos and Rodi, 1984; Fric and Roshko, 1994; Kelso and Smits, 1995; Kelso et al., 1996; Haven and Kurosaka, 1997) to name a few. Origin and evolution of important coherent flow structures viz. ($i$) shear layer structures, ($ii$) counter rotating vortex pair, ($iv$) wake vortices and their effect on jet trajectory was the collective focus of aforementioned studies. Although mixing of jet and crossflow is a central issue in any jet in crossflow, majority of detailed studies focused on mixing processes in jets in crossflow were reported recently (Smith and Mungal, 1998; Muppidi and Mahesh, 2006; Shan and Dimotakis, 2006; Muppidi and Mahesh, 2008). Smith and Mungal (1998) studied mixing in transverse jet with increasing velocity ratio and Reynolds number and putforth three scaling parameters $D$, $rD$ and $r^2D$. The jet centerline concentration near hole field is found to decay as $s^{(-1.3)}$(higher compared to free jets) and as $s^{(-2/3)}$ (lower compared to free jets) in downstream region, where $s = rD$ is a scaling parameter.The spatial location of the transition point scaled with $r^2D$ and consistently found at $s/r^2D = 0.3$. Effect of Reynolds

number on mixing, in the range of $1k$ to $20k$, was experimentally studied by Shan and Dimotakis (2006). They reported increased mixing with Reynolds number and highly anisotropic scalar field attributed to large scale vortical structures. Passive scalar mixing study using direct numerical simulation was performed by Muppidi and Mahesh (2008) for $Re = 5k$ and velocity ratio $r = 5.7$. They observed entrainment predominantly in downstream region due to a negative pressure gradient setup across the jet. All studies related to mixing looked at passive scalar issuing from a vertical round jet with no density difference between crossflow and jet fluid.

In the context of inclined jet in crossflow relevant to turbine cooling application, mixing of jet and crossflow fluid was studied by Tyagi and Acharya (2003); Renze et al. (2006). Tyagi and Acharya (2003) studied the effect of hairpin structure on macro mixing processes and entrainment rates due to a single hairpin vortex and quantified in terms of geometric properties of mixing interface. Renze et al. (2006) briefly addressed the role of counter rotating vortex pair entrainment process of crossflow fluid in jet region. In present case we focus on analysis of mixing mechanisms in inclined jet in crossflow based on modal analysis of scalar dissipation rate $\chi$ and quantify spatial contribution and time scales of various coherent flow structures of the flow field.

A significant Inclined jets in crossflow applicable to turbine cooling flows Computational approach in film cooling flows has substantially contributed in past decade, particularly application of large eddy simulation to high Re film cooling flows (Iourokina and Lele, 2005, 2006b,a; Pete and Lele, 2008; Rozati and Tafti, 2008a,b) and Renze et al. (2008a,b).

The LES data set used for this analysis is identical to previously descibed in Chapter 5

## 7.2 Mixing characteristics

Homogeneous mixtures of two miscible fluids can only be formed through molecular mixing. Stirring of fluid due to convective large eddies in unsteady/turbulent flows only induces large scalar gradients facilitating molecular mixing through Fickian diffusion. Therefore

mixing in turbulent environment occurs only at smallest length scales while the role of large structures is to induce large variance of scalar and creating 'mixing fronts' with large surface area. Simulation of mixing processes using large eddy simulation technique needs additional attention, as often smallest resolved scales are larger than Kolmogorov scales and rest are modeled through eddy viscosity type closure similar to equation 5.3. It follows that subgrid scale scalar transport needs similar closure to take account of scalar transport due to unresolved scales. The closure is obtained by calculating subgrid scale turbulent scalar diffusivity through dynamic procedure similar to (Moin et al., 1991) or by assumption of turbulent schmidt/prandtl number ($Sc_t/Pr_t$).

Mixing rate of two fluids may be quantified using scalar dissipation rate (SDR). SDR represents the rate of decay of scalar fluctuations or dissipation of scalar energy $0.5\Phi^2$ and given as, $\chi = \bar{\rho}\alpha(\Phi_j\Phi_j)$. $\alpha$ is molecular diffusivity $\bar{\rho}$ is average density at the mixing interface. In the context of laminar flows and direct numerical simulations, expression for $\chi$ is directly applicable for evaluating SDR. However, in case of large eddy simulation following the distinction between resolved and subgrid scale, evaluation for resolved SDR $\widetilde{\chi}$ would be $\widetilde{\chi} = \bar{\rho}\alpha(\widetilde{\Phi_j}\widetilde{\Phi_j})$ where $\widetilde{\Phi}$ represents resolved scalar field not taking into account the contribution of smaller scaled (modeled) eddies where majority of mixing takes place. In the work by Moin and Pierce (1999); Girimaji and Zhou (1996) a model proposed for subgrid scale scalar dissipation rate as $\chi_{sgs} = \bar{\rho}\alpha_t(\widetilde{\Phi_j}\widetilde{\Phi_j})$ where $\alpha_t$ is turbulent diffusivity for scalar and $\alpha_t$ is obtained from dynamic eddy diffusivity model similar to the one used for velocity field or assuming constant turbulent Schmidt or Prandtl number and dynamically evaluated momentum diffusion coefficient. Therefore the total scalar dissipation rate is given as, $\chi_{tot} = \bar{\rho}(\alpha + \alpha_t)(\widetilde{\Phi_j}\widetilde{\Phi_j})$. Scalar dissipation rate expressed as $\chi_{tot}$ have spatio-temporal variation associated with dynamics of underlying hydrodynamic flow structures therefore follow similar spectral energy distribution (Girimaji and Zhou, 1996).

In this paper, mixing processes in the flow field is studied based on fluid temperature as scalar. However, temperature in the simulation is a thermodynamic property and fluid

properties are treated as temperature dependent. Therefore, temperature is an active scalar as opposed to passive treatment customary to incompressible formulations of JICF. Figure 7.1a shows the time averaged temperature field and jet centerline streamline. The potential core of jet penetrates the crossflow quickly aligns with the cross stream flow dissipating rapidly. Figure 7.1b shows the decay of temperature along the jet center streamline in comparison with scalar concentration decay rate for vertical jet in crossflow (Muppidi and Mahesh, 2008). It is interesting to note that centerline scalar concentration decay begins at $s/D \approx 1.0$ compared to $s/D \approx 2.0$. This is attributed to early development of mixing layer formed in jet and crossflow interaction combined with immediate development of CRVP from the boundary layer issuing from the delivery tube similar to the mechanism due to Haven and Kurosaka (1997). Due to relatively delayed initiation of CRVP in case of veritical jet case of (Muppidi and Mahesh, 2008) with density ratio of unity and high momentum flux ratio $r = 5.7$, the potential core is maintained until $x/D \approx 2.0$ along the jet trajectory. However, centerline scalar concentration in case of vertical jets decays almost twice the rate of inclined jet. The decay rate for inclined jets are compared to the far field decay rates of jet in crossflow reported by Smith and Mungal (1998). Also the rate of concentration decay for inclined jet is less than $s^{-1}$ (for free jets) over the entire streamwise distance with no transition behavior observed similar to Smith and Mungal (1998) over streamwise distance of $12D$.

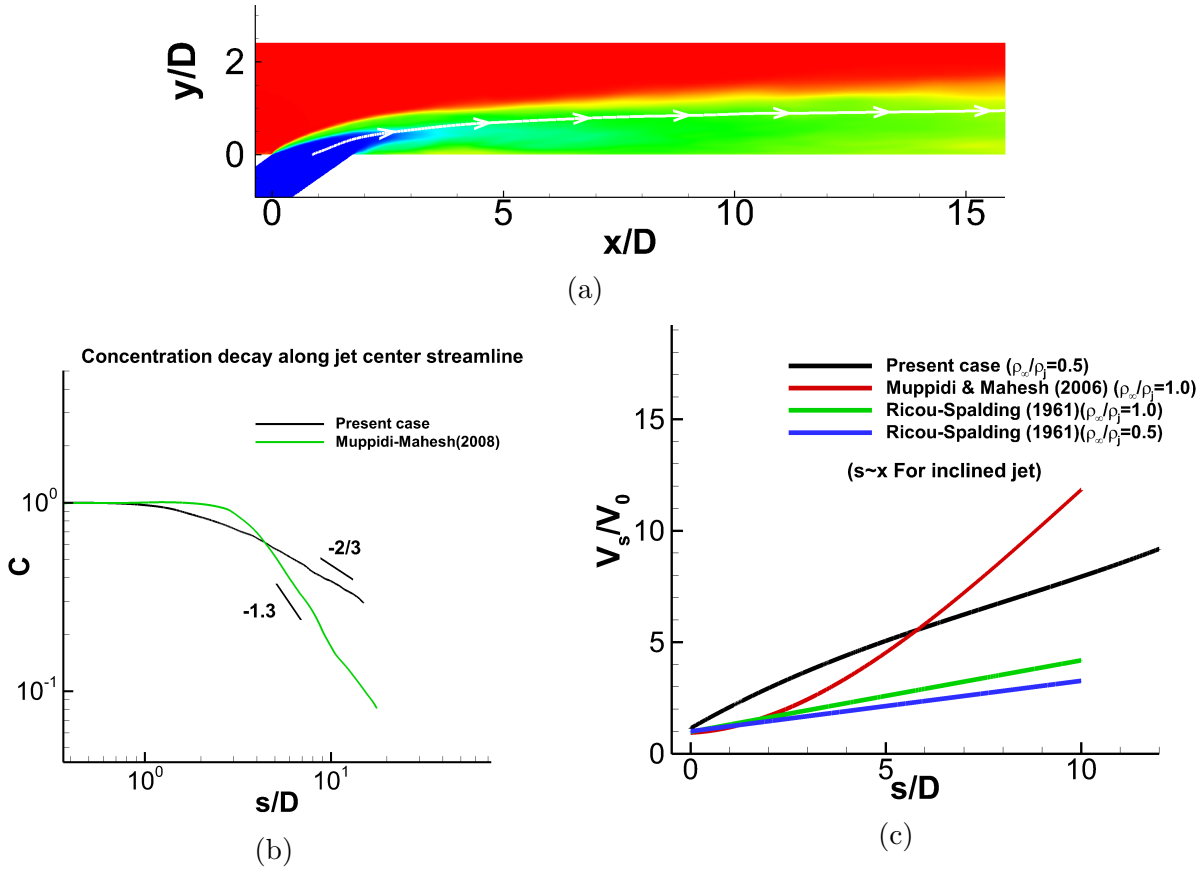


Figure 7.1: (a) Jet centerline streamline and temperature field, (b) Decay of scalar concetration along the jet centerline streamline compared with vertical jets, (c) Volume flux of the scalar carrying fluid compared with vertical and axisymmetric round jets

Figure 7.1c shows the volume flux of scalar carrying fluid normalized by jet volume flux for present case compared with (Muppidi and Mahesh, 2008) and Ricou-Spalding correlation for axisymmetric co-flowing jet with density ratio of unity and 0.5. Threshold limit used to identify the scalar carrying and non-scalar carrying fluid has is a subjective matter. No convergence was found in the low value of threshold limit similar to Muppidi and Mahesh (2008). Identical to them a threshold limit of 1% scalar concentration is used to mark scalar carrying fluid in the present case for comparison purposes.

Volume flux of scalar carrying fluid for inclined jet is seen higher compared to vertical jet until $x/D \approx 6.0$. The early entrainment is attributed to shear layer mixing due to windward shear layer and initial development of CRVP. Figure 7.2 shows a streamwise normal

section at $x/D = 0.25$ from downstream edge of the jet exit. The mixing due to shear layer formed by crossflow and jet is apparent above the potential core of the jet. While a pair of counter rotating vortex on the lateral boundaries of jet potential core are seen entraining crossflow fluid directly underneath jet and inside. It is interesting to note that, inclined jets in crossflow entrains large amount of fluid compared to regular axisymmetric jets despite of lower centerline decay rate due to distinct CRVP feature. Since vertical jet entrains large amount of surrounding fluid as it bends in the crossflow, attributed to development of windward shear layer and CRVP in downstream region as described by Yuan and Street (1998), centerline concentration decays at a higher rate.

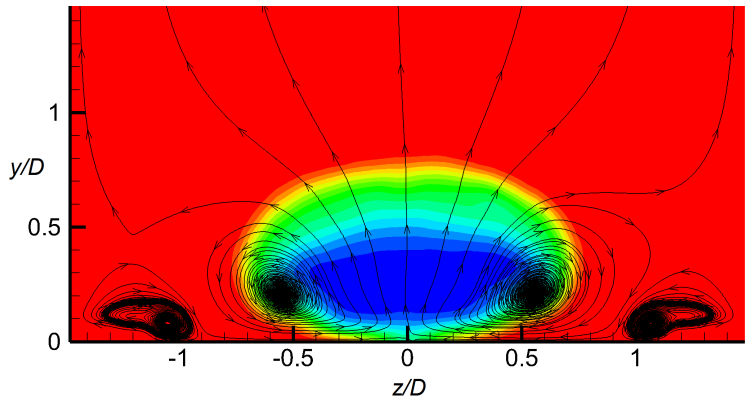


Figure 7.2: Entrainment due to CRVP at $x/D$=1.5

### 7.2.1 Scalar dissipation rate ($\chi$)

Figure 7.3a shows the instantaneous three dimensional flow structures (iso-surfaces of $\lambda_2$) with temperature contours. Characteristic to jet in crossflow configuration, coherent flow structures viz. Horseshoe, Kelvin-Helmholtz and hairpin structures are noticed. Mixing layer structures are apparent due temperature gradient. The uniform temperature of horse shoe vortices reveal that they do not directly contribute towards entrainment or mixing of jet and crossflow fluid. Figure 7.3b and 7.3c show instantaneous isosurfaces of resolved and subgrid scale scalar dissipation rates. A distinct feature of resolved and subgrid scale SDR iso-surface is noticed. Resolved scale SDR has a direct correlation with thermal gradient field

and therefore envelopes entire jet region while subgrid scale SDR has a strong dependency on the underlying coherent structures apparent from its topology shown in Figure 7.4.

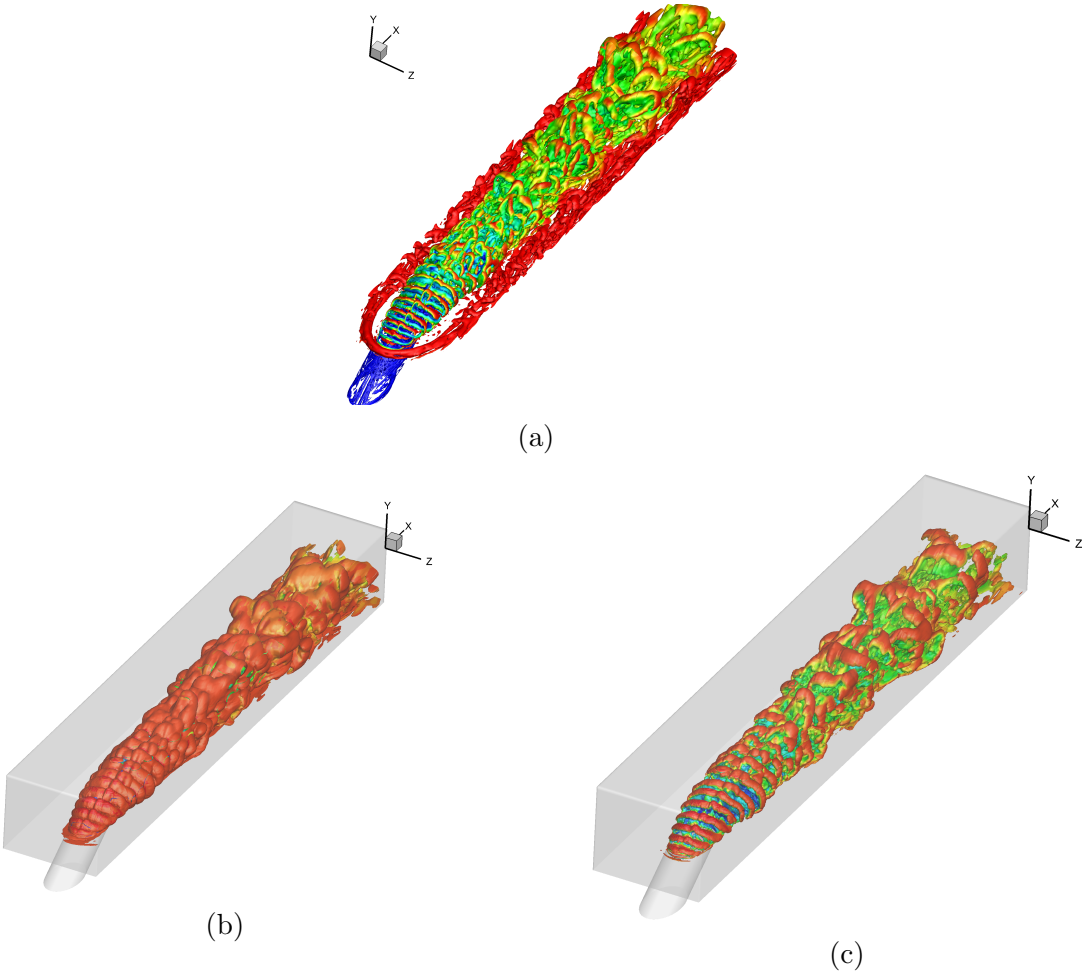


Figure 7.3: Instantaneous flow and SDR features

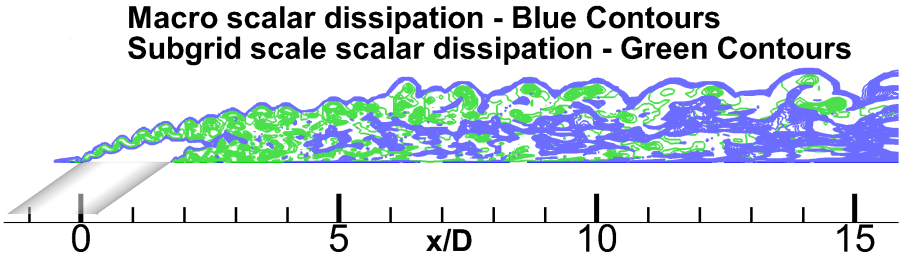


Figure 7.4: SDR contours on spanwise mid section

It is worth to discuss in brief the dependency of subgrid scale SDR on the underlying coherent structures. In a typical turbulent flow field the production of turbulent is associated

with mean strain rate $S_{ij}$ and dissipation with local or fluctuating strain rate $s_{ij}$. Coherent structures initiated due to some kind of flow instability induce large fluctuating strain rates $s_{ij}$ leading to higher dissipation of turbulent kinetic energy. Typically realized through vortex stretching and tilting, large scale structures transfer energy to the smaller scales. A subgrid eddy viscosity model such as, $\mu_t = C_s^2 \bar{\rho} \Delta^2 \left( |\widetilde{S}| \right)^2$ tends to model such subgrid scale eddies through eddy diffusivity. Given scalar gradient setup due to entrainment of large coherent structures, subgrid scale SDR follow the topology of underlying flow structures.

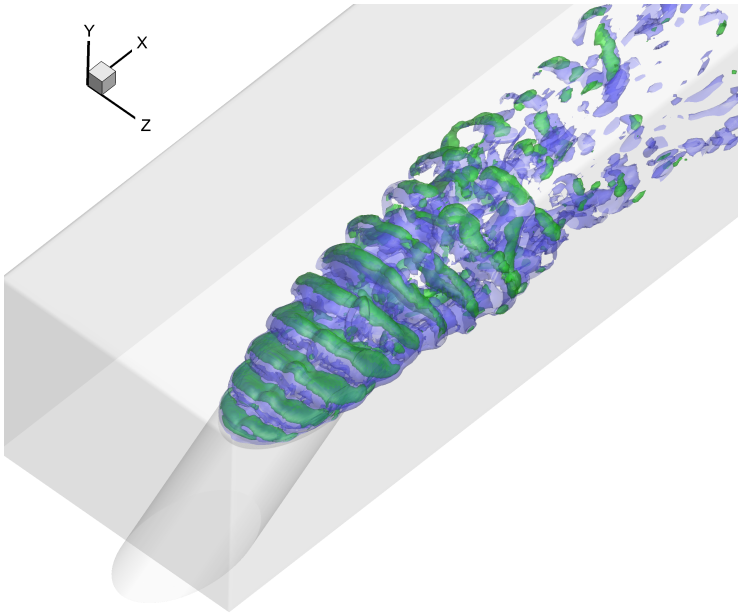


Figure 7.5: Isosurfaces of higher SDR (Blue contours - Resolved SDR, Green contours-modeled SDR)

SDR iso-surfaces with higher iso-values for resolved and subgrid SDR visualized in Figure 7.5 shows that highest SDR is associated with shear layer structures. In order to evaluate the spatial variation of resolved and subgrid scale SDR in the bulk of jet region, $2^{\text{nd}}norm$ of cell volume weighted SDR is evaluated on discrete streamwise volumes of uniform streamwise dimension of $0.5D$. We choose to plot $2^{\text{nd}}$ of SDR as it is synonymous to 'SDR energy' indicating the mixing rate strength over a finite region.

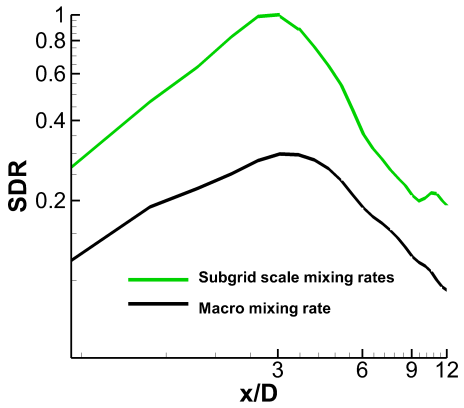


Figure 7.6: Spatial variation of volume weighted $2^{\text{nd}}norm$ of resolved and subgrid scale SDR

Figure 7.6 shows the spatial variation of resolved and subgrid scale SDR. The scales are normalized with highest subgrid scale SDR. As expected, subgrid scale SDR has higher strength throughout the bulk of jet region. The maximum strength for both resolved and subgrid scale SDR is observed at $x \approx 3D$. At the same spatial location the potential core of the jet cease to exist observed in Figure 7.1a. A transition of shear layer structures to rather a chaotic pattern is observed approximately at the same spatial location predominantly due to interaction of wake and evolution of hairpin type structures (Figure 7.3a and 7.3c), resulting in increased mixing fronts. Although highest SDR is due to mixing layer vortices, initial ($0 < x/D < 3$) low volume weighted SDR in Figure 7.6 is due to fewer mixing fronts apparent in Figure 7.5. With general mixing characteristics discussed, we proceed to spatio-temporal analysis of SDR to obtain spectral and spatial characteristics of SDR modes

## 7.3 Modal analysis of mixing processes

Present case of flow field is a convectively dominated flow with high Peclet number $Pe = RePr = 14400$ therefore the transport of scalar is realized through the role of underlying hydrodynamic structures in inducing large scalar gradients. Therefore, mixing process is governed by hydrodynamic flow structure as established in previous section. In this section,

underlying hydrodynamic flow responsible for mixing is spectrally decomposed into various modes to quantify individual modal contribution. Spatio-temporal fluctuations of SDR contains information of only those coherent structures relevant to mixing. Therefore, modal analysis of the scalar dissipation rates is a natural choice that enables to focus on dominant mixing modes and related hydrodynamic modes. Dynamic mode decomposition is preferred for modal analysis of SDR for following reasons. DMD allows to rank extracted modes based based on multiple criterion $(i)$ Growth rate - suggesting dynamically significant modes, $(ii)$ Modal energy $||DM||_2 \forall Domain$, $(iii)$ Modal energy $||DM||_2 \forall R$ where $R$ is the region of interest and $(iv)$ frequency content. Such an approach was demonstrated by Kalghatgi and Acharya (2013) to identify modal contribution of thermal modes on film cooled wall.

Overview of algorithm and parameters used in for the analysis is identical to reported in previous study (Kalghatgi and Acharya, 2013). A snapshot matrix is arranged as,

$$V_1^N = \{v_1, v_2, v_3, , v_N\} \tag{7.1}$$

Individual snapshots $v_i$ in the present study includes vector of subgrid scale and macro scale scalar dissipation rates over the entire region of cross-flow and jet interaction. A field evolution (linear) operator A is assumed such that,

$$AV_1^{(N-1)} = \{Av_1, A^2v_1, , A^{(N-1)}v_1\} = V_2^N \tag{7.2}$$

Eigen modes and Eigen values of Aare estimated by formulating a companion matrix,

$$C = \begin{bmatrix} 0 & & \dots & 0 & c_1 \\ 1 & \ddots & & \vdots & c_2 \\ 0 & \ddots & \ddots & & \vdots \\ \vdots & & 1 & 0 & c_{N-2} \\ 0 & \dots & 0 & 1 & c_{N-1} \end{bmatrix} \tag{7.3}$$

where, the $c_i$s are the coefficients of linear combination in a least square problem of expressing $v_N^{th}$ snapshot in terms of preceding $N-1$ snapshots. Total of $N = 100$ snapshots were used for DMD analysis, spanning uniformly over $(N\Delta t U_\infty)/D = 6.3$. Temporal separation of $\Delta t = 4.0 \times 10^{-5} s$ is used between consecutive snapshots that satisfies the Nyquist criterion (Schmidt, 2010). Estimation of highest dominant frequency ($3180 Hz$) was done based on FFT of streamwise velocity signal at the leading edge of film cooling hole (Kalghatgi and Acharya, 2013). Convergence criterion for Ritz values were set to $e_R \leq 1.0 \times 10^{-5}$.

### 7.3.1 Results of modal analysis

Growth and energy spectra for macro and subgrid scale mixing are shown in Figure 7.7 *a* through *d*. Modes ranked based on the criterion of higher growth and higher energy ($||DM||_2 \forall Domain$) are marked. Only a selected few modes and the frequency contents are listed in table 7.1 below,

Table 7.1: Mode tag and frequency

| Mode Tag | Frequency ($Hz$) |
|---|---|
| A($2^{nd}$ Harmonic) Red arrow | 9770 |
| B($1^{nd}$ Harmonic) Green arrow | 6493 |
| C(K-H Fundamental) Blue arrow | 3250 |
| D Hairpin mode Orange | 1119 |
| E CVP mode | 550 |
| F CVP mode | 253 |

Fundamental shear layer (kelvin-Helmholtz) mode ($3250 Hz$) and it's 2nd and 3rd harmonic at $6493 Hz$ and $9770 Hz$ are found to have distinctive growth rates indicating their dynamic significance for both resolved scale and subgrid scale mixing processes (Figure 7.7a and Figure 7.7b).

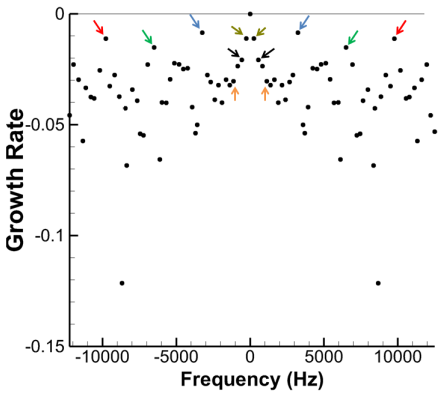


(a) Resolved SDR growth spectra

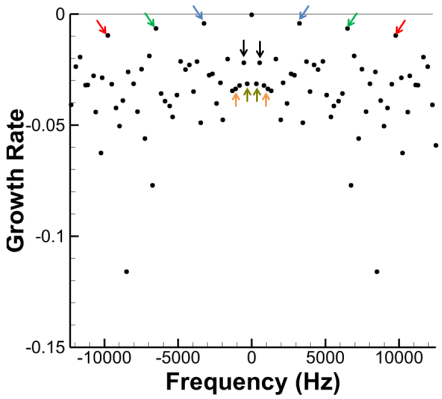


(b) Subgrid SDR growth spectra

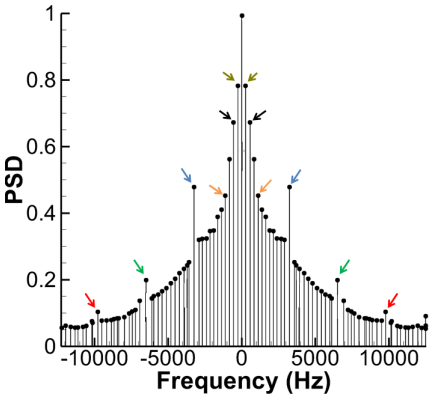


(c) Resolved SDR global energy spectra

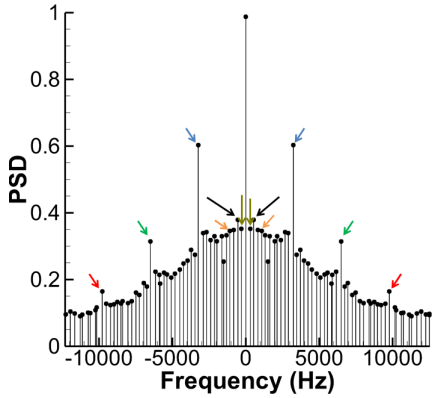


(d) Subgrid SDR global energy spectra

Figure 7.7: Growth and energy spectra of DMD modes

Ranking of both resolved and subgrid scale SDR modes based on global energy spectrum ($||DM_i||_2 \forall Domain$) is shown in Figure 7.7c and 7.7d. Low frequency modes (such as D, E, F) are found to have largest contribution in resolved SDR while fundamental mode C carry highest subgrid scale SDR. Higher harmonics of fundamental shear layer modes (A and B) have only marginal contribution in resolved SDR however, for SDR higher harmonics show higher global energy content.

At this stage a comment on nature of subgrid scale SDR is necessary in order to clarify the meaning of frequency content of subgrid scale SDR. It is noted that dominant modes of resolved scale and subgrid scale SDR have identical time scales. Following Richardson's law of decay of turbulent energy, smaller length scale structures are associated with smaller time scales. However, eddy viscosity model attempts to 'bunch' all subgrid scale structures within

a typical grid control volume. In the process all the dynamic information of the subgrid scale eddies is lost and only dissipation effect is captured. Therefore, subgrid scale SDR frequency content may be interpreted as the time scale of bunched structures in terms of eddy viscosity and should not be confused with smaller time scales associated with smaller flow structures. Due to similar reasons similarity in topological structures of resolved and subgrid scale SDR modes is observed. Figure 7.8 *a* through *d* show topological nature of modes listed in Table 7.1. It should be noted that smallest iso-value is chosen so that modal topology over entire jet region is visualized and mere presence of mode is not an indication of modal strength. Only resolved scale modes are shown, subgrid scale modes have similar topology.

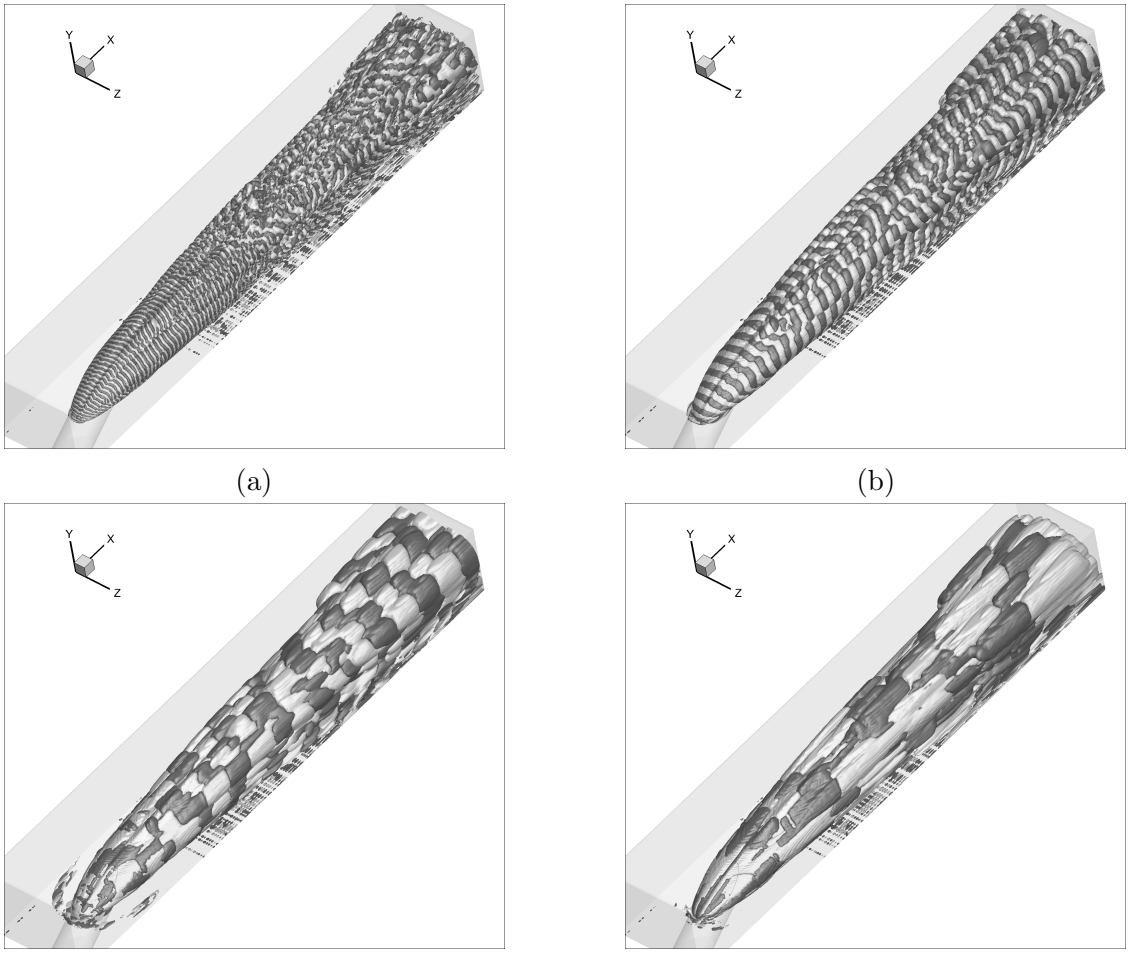


Figure 7.8: Topology of selected modes

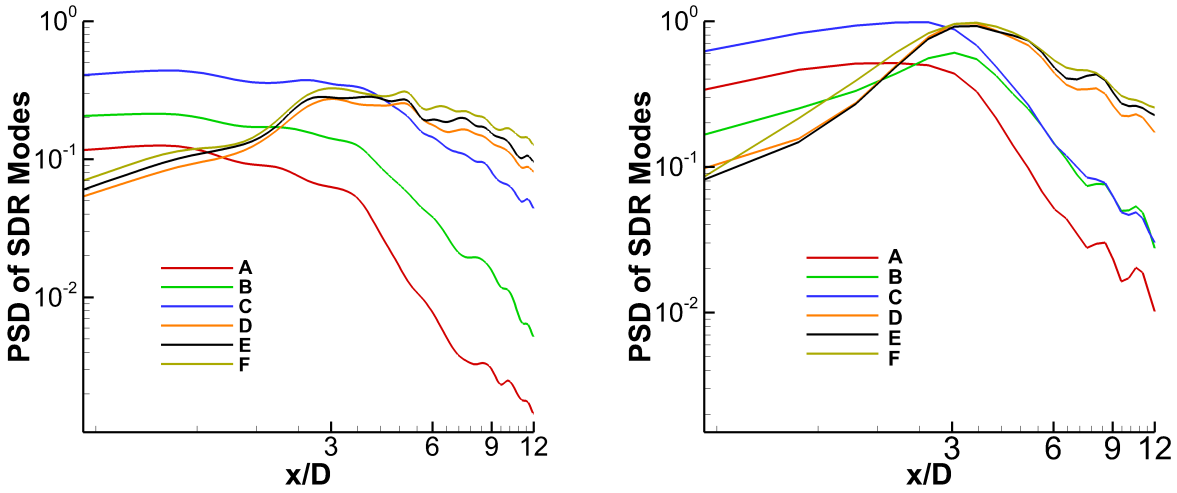


(a) Resolved SDR modes (b) Subgrid scale SDR modes

Figure 7.9: Spatial energy distribution of DMD modes

Figure 7.9 shows the spatial variation of modal energy in streamwise direction. Spatial variation of modal energy was determined by evaluating $||DM||_2$ from $x/D = 0$ to $x/D = 12$ progressively over a domain size of $0.5D$. Although modal energy is discretely evaluated, a smooth variation is showed to provide a perspective. Figure 7.9a and Figure 7.9b show resolved scale and subgrid scale SDR modes energy peaks at $x/D \approx 3.0$. Before $x/D = 3.0$ shear layer modes (fundamental and higher harmonics) contribute maximum for SDR and decay sharply after that. Topological structures of these modes are shown in Figure 7.8a and Figure 7.8b. Low frequency modes D, E and F dominate beyond $x/D = 3.0$. Topological nature shown in Figure 7.8c and 7.8d reveal hairpin and CVP type flow structures for lower frequency modes.

These findings are corroborated by previous work of (Yuan and Street, 1998) suggesting CRVP is largely responsible for entrainment of crossflow fluid thus increasing the mixing in downstream region and (Smith and Mungal, 1998) indicating the formation of CRVP leads to higher mixing rates in near hole region. In addition, high SDR related to formation of shear layer vortices is also revealed. Higher SDR modal energy contribution of low frequency modes in downstream region is attributed to their role in entrainment of crossflow fluid in

jet region and creating mixing fronts with large surface area.

## 7.4 Conclusion

Mixing of jet and crossflow fluids is characterized for an inclined jet in crossflow. Jet centerline scalar concentration decay is found to follow $x^{-2/3}$ that is smaller than free jets. Entrainment quantification by scalar carrying fluid flux revealed higher initial entrainment compared to vertical jets and over all high entrainment compared to free jets estimated by Ricou-Spalding correlation, attributed to CRVP and shear layer vortices. Mixing processes are analyzed by spatial variation of scalar dissipation rate revealed bulk mixing rate peaking at $x \approx 3D$ for both resolved and subgrid scale mixing. Further, spatio-temporal analysis of SDR showed highest modal energy is associated with fundamental shear layer mode and higher harmonics. Low frequency CRVP and hairpin vortex structures contribute mixing downstream of the hole beyond $x \approx 3D$ through entrainment. Finally, the modal analysis enables to determine the spectral and spatial characteristics of scalar dissipation rates that has value in LES of mixing and combustion studies.

# Chapter 8
# Improved Film Cooling Effectiveness with a Round Film Cooling Hole Embedded in Contoured Crater

**Abstract**

Studies of film cooling holes embedded in craters and trenches have shown significant improvements in the film cooling performance. In this paper a new design of a round film cooling hole embedded in a contoured crater is proposed for improved film cooling effectiveness over existing crater designs. The proposed design of the contour aims to generate a pair of vortices that counter and diminish the near-field development of the main kidney-pair vortex generated by the flm cooling jet. With a weakened kidney-pair vortex, the coolant jet is expected to stay closer to the wall, reduce mixing, and therefore increase cooling effectiveness. In the present study, the performance of the proposed contoured crater design is evaluated for depth between $0.2D$ and $0.75D$. A round film cooling hole with a $35^0$ inclined short delivery tube ($l/D = 1.75$), free stream Reynolds number $Re_D = 16000$ and density ratio of coolant to free stream fluid $\rho_j/\rho_\infty = 2.0$ is used as the baseline case. Hydrodynamic and thermal fields for all cases are investigated numerically using large eddy simulation technique. The baseline case results are validated with published experimental data. The performance of the new crater design for various crater depths are compared with the baseline case. Results are also compared with other reported crater designs with similar flow conditions and crater depth. Performance improvement in cooling effectiveness of over

100% of the corresponding baseline case is observed for the contoured crater.

## 8.1 Introduction

The first study on the effect of hole shape on film cooling performance was reported by Goldstein et al. (1974). They used a laterally diffused fan shaped film cooling hole with $10^0$ diffusion angle. Widening of the jet exit lead to deceleration of the cooling fluid effectively reducing blowing ratio and increased lateral spreading of the coolant fluid due to laterally diffused geometry, resulting in higher cooling area coverage and film cooling effectiveness. A remarkable feature of the shaped hole is their ability to maintain higher film cooling effectiveness at higher blowing ratios ($M > 0.5$) where cylindrical jets detach resulting in degradation in cooling performance. Since then, a variety of film cooling hole shapes were developed; conical diffuser shaped (Haven et al., 1997; Chen et al., 1998), fan shaped holes with laterally expanded exit, laid back fan shaped holes (Thole et al., 1998; Gritsch et al., 1998a,b) and console holes (Sargison et al., 2002). In recent years more complex shapes such as crescent (Lu, 2007), dumbell shaped (Liu et al., 2010), heart shaped (Yusop et al., 2013) have been reported. Shaped holes are found to provide significant improvements in adiabatic film cooling effectiveness, with the fan shaped (laid back and laterally diffused) observed to perform over other shapes; they have a further advantage of being easier to manufacture. An extensive review of shaped holes may be found in (Bunker, 2005; Kim et al., 2012).

Round film cooling holes with triangular tabs have also been investigated (Nasir et al., 2003). Using an upstream triangular notch an anti-kidney pair vortex was generated on top of the film cooling jet reducing the jet penetration in the crossflow. About 200-300% increase in local adiabatic film cooling effectiveness was observed over a range of blowing ratios ($0.56 \leq M \leq 1.7$). Using a similar idea, a triangular ridge was constructed along the windward edge inside the delivery tubeYang and Zhang (2012) and improvements similar to Nasir et al. (2003) were observed.

Although shaped holes and triangular tabs provide a marked increase in the adiabatic film

cooling effectiveness over round holes, there has been continued interest in exploring other hole shapes or configurations that provide greater lateral coverage and higher effectiveness values. As an example in recent years round holes embedded in crater depressions (Fric and Campbell, 2002) and trenches (Bunker, 2002) have been shown to provide significant benefits in film cooling effectiveness. The idea behind this approach is to provide a secondary expansion chamber at the end of delivery tube potentially reducing the momentum flux of the coolant jet and increasing the coolant spreading before the film emerges on to the airfoil surface providing a simple and effective approach towards increasing cooling effectiveness.

A trench of $0.5D$ depth on the suction side of the turbine vane was investigated by Waye and Bogard (2007) who studied the effect of various lip configurations. Their findings showed in excess of 100% improvements in adiabatic film cooling effectiveness in the near hole region with nearly 40% increase at down stream locations. Narrow trenches performed better over wide trenches and trenches with a downstream rectangular lip showed higher cooling effectiveness over trenches with other lip configurations and the base line no-lip trench. They also found no effect of turbulence intensity and density ratio on the cooling performance of the trenches.

A study of the effect of different craters and trench configurations on the film cooling performance (Dorrington et al., 2007) showed that craters with the walls flush to the embedded film cooling hole performed better than other configurations with annular gap between crater wall and film cooling hole edge. In their study narrow trenches performed better than wide trenches and the optimal value of trench depth was found to be $0.75D$. Little to no effect of trench width on film cooling performance of trenches with depth grater than $0.75D$ was observed. Similar observations for round film cooling hole embedded in craters and trenches were reported for a flat plate film cooling (Lu, 2007).

One advantage of cratered or trenched holes, particularly those with shallow depths, is that they can be generated using thermal barrier coatings (TBC) that are common place today as part of the thermal management system of the gas turbine airfoil. This approach

substantially reduces the manufacturing difficulty associated with the reshaping of the hole in the metal surface itself. An experimental investigation of trench and crater configurations formed in simulated TBCs was studied to understand the thermal behavior at the metal-TBC interface under different surface cooling effectiveness and internal cooling (Davidson et al., 2012). The crater and trench configuration under consideration were formed of uniform depth of $1.2D$. Although in this study, film cooling did not play a significant role in directly protecting the blade material due to the dominant role of TBC, it was noted that the use of film cooling may substantially delay TBC spallation enhancing the life of the turbine airfoil.

In the present study a modified contoured crater design is proposed and numerically investigated for cooling performance. The results are compared with conventional crater designs from published experimental work. The baseline case used for this study is described in Chapter 5

### 8.1.1 Proposed contoured crater

As noted earlier, various shapes and configurations of craters and trenches have been studied. They have mostly relied on a common principle of providing a secondary expansion chamber or cavity to reduce the local momentum flux. The coolant jet impinges on the crater or trench wall and also contributes to lateral spreading of the coolant fluid in the cavity leading to greater lateral coverage by the coolant. Further, craters and trenches interfere with the formation of counter rotating vortex pair from the boundary layer vorticity within the delivery tube (Haven and Kurosaka, 1997), hindering the crossflow entrainment as well as the jet liftoff at higher blowing ratios.

Figure 8.1 shows the schematic of the proposed V-crater design. The key feature of the design is a blunt v-shaped protrusion towards the downstream end of the embedded film cooling hole. The objective of this protrusion is two fold, ($i$) jet impingement on the tip of v-shaped protrusion that is expected to partially divert the coolant fluid in the lateral direction, ($ii$) the v-shaped protrusion creates a partial obstruction on the leeward region

of the jet and results in formation of an anti-CVP pair below the jet creating downdraft of coolant fluid on the film cooling wall in the near-hole region.

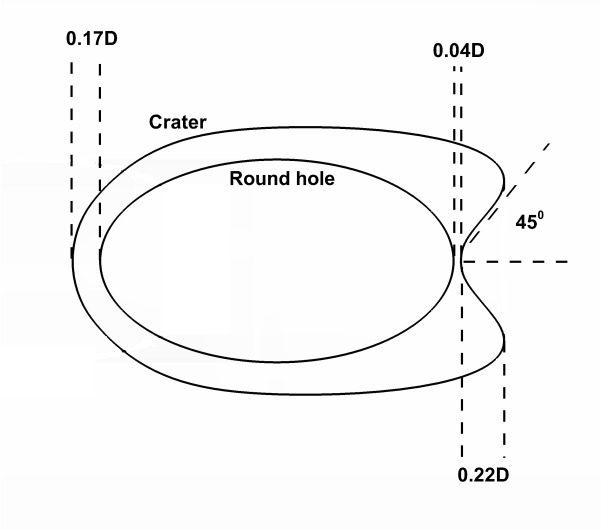


Figure 8.1: Schematic of the contoured crater

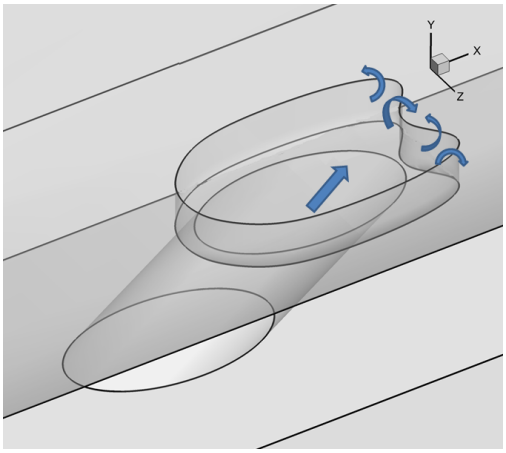


Figure 8.2: CAD model of the contoured crater

The crater dimensions are chosen based on trial-and-error and engineering intuition such that the side wall of the crater would interfere with the CVP formation. Therefore a minimum annular gap of $0.17D$ was chosen on the upstream side based on the length scale of the time averaged recirculation region in the baseline case. The lip of the protrusion should ideally be flush to the film cooling hole edge; however, to avoid modeling difficulties a small gap of $0.04D$ is chosen arbitrarily (see Figure 8.1). The angle between the side edges of the

protrusion was set to $90^0$. The lip radius of curvature of the protrusion was matched with the tip radius of curvature of the leeward end of the film cooling hole. The protrusion length of the V-arms was selected to be $0.22D$ and the radius of curvature of two the symmetric concave regions is close to the radius of curvature of the film cooling hole at the leeward end. The idea is to avoid a tight radius of curvature that may result in potential stress concentration sites and manufacturing difficulties. Total of three crater depths $0.2D$, $0.4D$ and $0.75D$ are studied.

## 8.2 Film cooling effectiveness

Figure 8.3 and 8.4 show centerline and laterally averaged adiabatic film cooling effectiveness for all the cases under consideration. In this plot $x/D = 0$ is set at at the downstream edge of the film cooling hole for the baseline case and at the lip of the V-shaped protrusion for the crater cases (the two zero-locations are offset by 0.04D, and represent the first y/D=0 location on the surface downstream of the hole). For all crater depths, a marked improvement in both centerline and adiabatic film cooling effectiveness is witnessed over the baseline case. In particular, the near hole regions show the maximum gains in the film cooling effectiveness with a near doubling of the centerline values for $x/D$ in the range of 1-2. The centerline profile of cooling effectiveness for the crater designs do not show the rapid decline that was observed in the baseline case, indicating an attached jet to the film cooled wall.

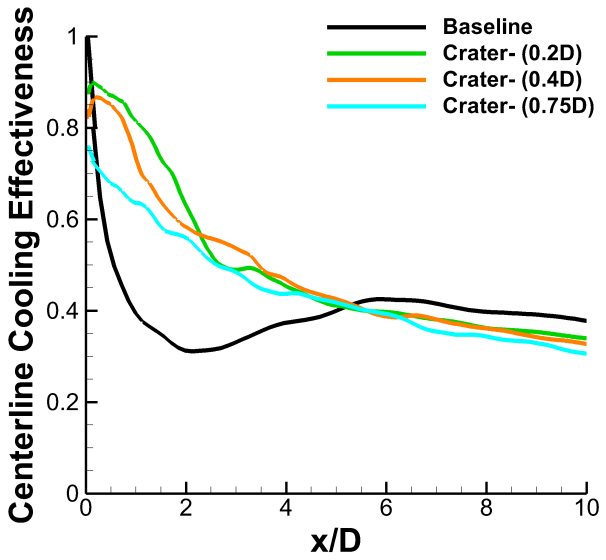


Figure 8.3: Centerline film cooling effectiveness for the baseline case and the various contoured craters

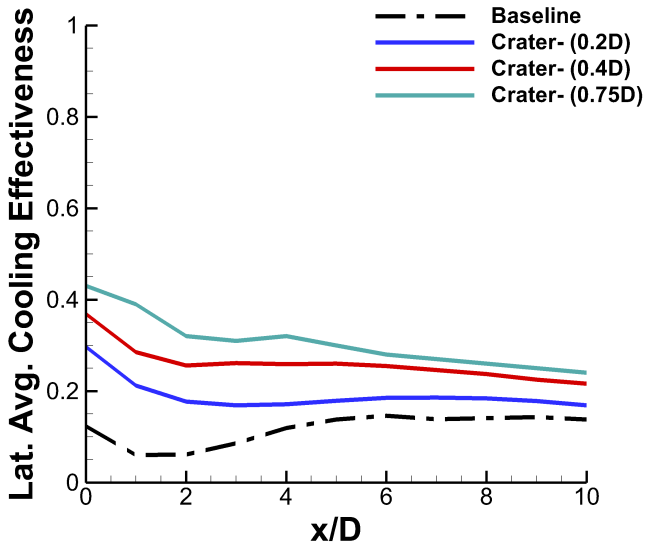


Figure 8.4: Laterally averaged film cooling effectiveness for the baseline case and the various contoured craters

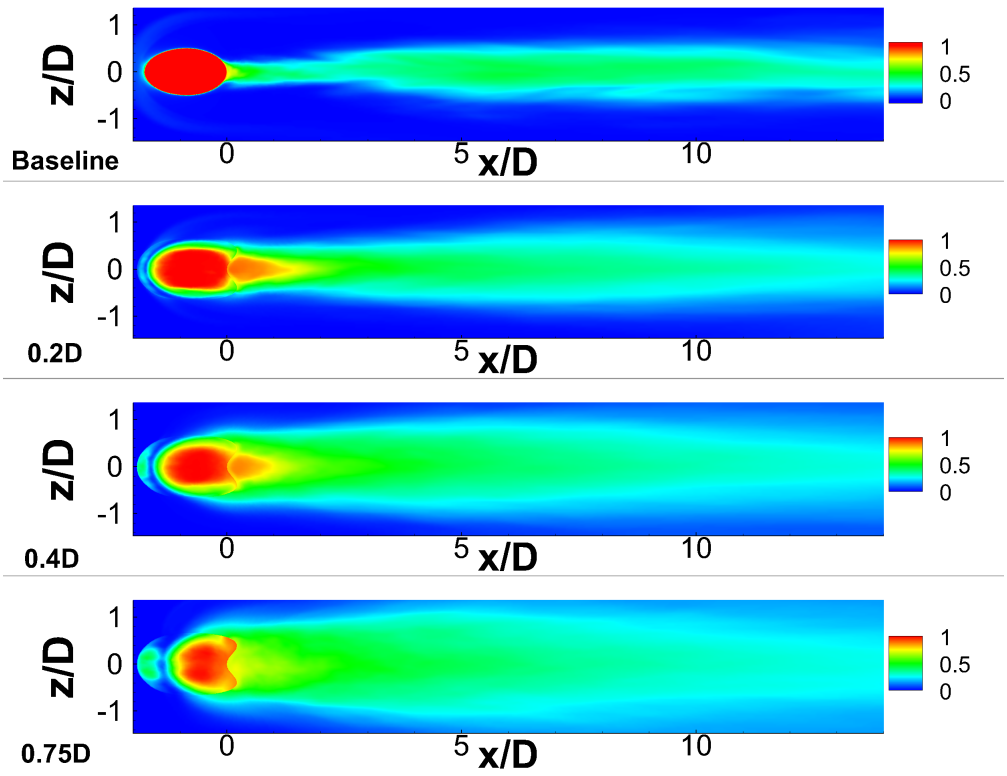


Figure 8.5: Adiabatic film cooling effectiveness on the film cooled wall for the baseline case and V-contoured craters of different depths

The crater depth also has a measurable role that is particularly evident in the near-hole region and in spanwise effectiveness. It is interesting to note that the laterally averaged film cooling effectiveness consistently increases as the crater depth is increased. However, centerline profile shows decline in cooling effectiveness in the near hole region ($x < 2D$) as crater depth is increased. Beyond $x = 2D$ the effect of crater depth did not play any role in the centerline cooling effectiveness while for laterally-averaged effectiveness, the crater-related enhancement persist beyond $x/D$ of 10, with significant near-eight-fold increase in near field around $x/D$ of 1.

Contours of film cooling effectiveness on the cooled wall for all cases are shown in Figure 8.5. A region of high cooling effectiveness is observed immediately downstream of the V-shaped protrusion. As crater depth is increased this region progressively shrinks (also seen in Figure 8.3) and lateral spreading of the coolant fluid increases leading to the higher

laterally-averaged effectiveness values seen in Figure 8.4. It is clear that the deeper craters are quite effective in the lateral dispersion of the coolant which near full-lateral-coverage for the deepest crater. This behavior is clearly responsible for the very significant increase in the laterally-averaged effectiveness for the deepest crater.

### 8.2.1 Comparison with conventional crater and trench design

Performance of the proposed crater design is compared with the performance of conventional craters and trenches reported in literature (Lu, 2007; Waye and Bogard, 2007) and with comparable flow parameters. The best performing crater configuration reported in experimental findings from (Lu, 2007) has crater walls flush to the leeward and windward ends of the embedded film cooling hole with a depth of $0.5D$. In the same study they reported best performing trench with a depth of $0.75D$ and width $3D$. In their baseline case, the delivery tube aspect ratio $l/D$ was 2. A film coolant jet Reynolds number of $Re_D = 11k$ with jet inclination angle $\Theta = 30^0$ and density ratio $D.R. = 1.0$ was used in this study. In a separate study (Waye and Bogard, 2007), the effect of trenches was investigated using an accelerated free stream flow over a turbine vane, with effective coolant jet Reynolds number $Re_D = 7.3k$. The baseline hole aspect ratio $l/D = 6.7$ and density ratio ($D.R.$) in the range 1.3 to 1.5 was used. The best performing trench was a narrow trench with trench walls flush to the leeward and windward ends of the embedded film cooling hole. For the purpose of comparison, results of blowing ratio $M = 1.0$ was chosen for all the above mentioned configurations. Owing to differences in the cooling performance among the baseline cases a direct comparison in the cooling performances of the craters was not be made. Instead, the gain in laterally-averaged cooling performance due to the crater over the corresponding baseline case in each study is compared to assess relative performance.

Figure 8.6 shows the percentage increase in the laterally averaged film cooling effectiveness due to selected crater and trench designs over their respective baseline cases. Compared to the conventional crater/trenches of similar depth, the present contoured crater design

shows greater than 200% increase in the performance gain in the peak value near hole region and consistently remains higher in the far downstream region.

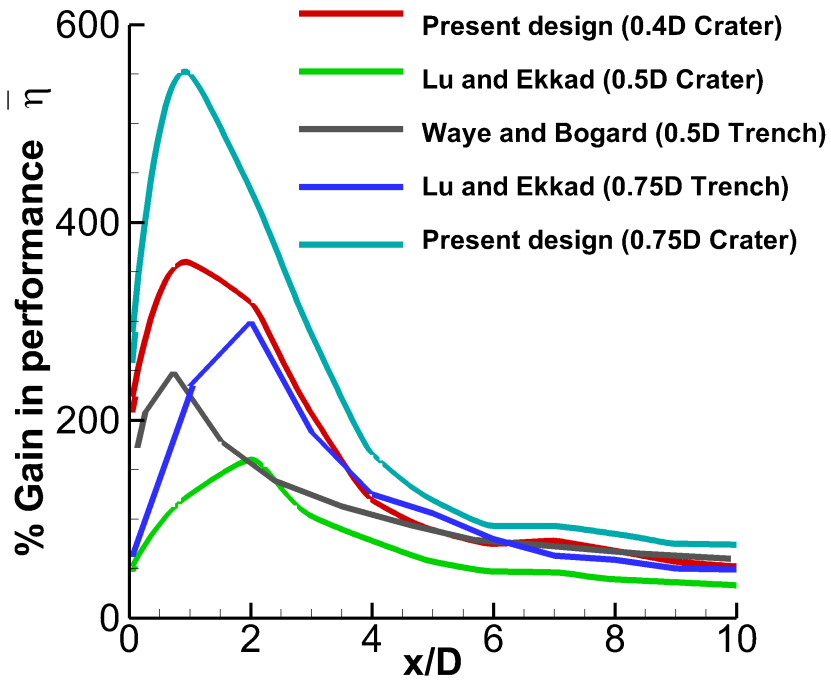


Figure 8.6: Comparison of laterally-averaged effectiveness improvements over baseline case for conventional crater, trenches and contoured crater designs

Compared to the best performing trench cases ($0.75D$ depth), the present contoured crater design ($0.75D$) has higher than a 300% gain while the comparable depth ($0.4D$) contoured crater design has a 100% gain in the peak film cooling effectiveness increase over the baseline case in the near hole region and this gain persists up to $x = 4D$. Clearly, the contoured crater design shows exceptional performance in the near field over available crater/trench designs.

### 8.2.2 CVP and Anti-CVP vortex

To explain the above results, attention is focused on the region of high film cooling effectiveness immediately downstream of the film cooling hole. Figure 8.8 to 8.10 show the time

averaged flow and temperature field on streamwise-normal cross sections at $x = 0.5D$ for the baseline case and all three contoured crater depths. The baseline case clearly shows the CVP as the dominant streamwise-oriented structure. Due to self-induction, and the upward directed flow in the middle, the CVP tends to lift the coolant jet. It also entrains hot gases form the upper and lateral edges that increase the thermal loading on the wall. In case of the contoured crater design for $0.2D$ and $0.4D$ depth, an additional pair of vortices between the classical counter rotating pair of vortices are observed. As indicated by the streamlines, orientation of these counter-rotating vortices are aligned but opposite in sign with the classical counter rotating vortex pair, thereby generating a central downward draft and bringing the coolant fluid from jet core directly onto the cooling wall and attenuating the jet liftoff. The potential core of the coolant jet is shown in Figure 8.11 using temperature contours on spanwise mid section. The baseline case shows a jet liftoff (with the blue core displaced from the surface) while the cratered cases have the jet core attached to the film cooling wall. The region of attached jet core correspond to the region of high film cooling effectiveness observed in Figure 8.5. We term the new vortex pair as anti-CVP vortices; however, it should be noted that despite of identical terminology used here there is no commonality between the present vortex system and anti-kidney/anti-CVP vortex reported in (Heidmann and Ekkad, 2008; Haven et al., 1997).

The interaction of CVP and anti-CVP leads to rapid decay of the later limiting its streamwise length in the range of $1D$ to $2D$ downstream of the film cooling hole. The magnitude of streamwise vorticity in the CVP and anti-CVP vortex differ only by 10%-20% however, the anti-CVP vortex being smaller of the two, has less energy than CVP vortex and hence decays. The development and decay of the anti-CVP is different for the different depths with a faster decay for the deeper crater as seen by observing Figures 8.7-8.10. Although the anti-CVP is active over a short streamwise distance, it significantly improves the near hole cooling performance.

The topology of the anti-CVP in three dimensional space contoured with the streamwise

vorticity component is shown in Figures 8.12 to 8.14 for all crater depths. A second effect of craters on the film cooling performance is seen in the from of the interaction of the nascent CVP with the side walls of the crater. Shallow craters are found to have minimal impact on the development of the CVP as it forms from the side wall vorticity of the delivery tube (Figure 8.12). For deeper dimples this interaction is found to disrupt the streamwise development of the CVP that is clearly evident for the deepest crater in Figure 8.14. Thus, for deeper craters, the in-hole vorticity as it exits the delivery tube impinges on the carter walls (Figure 8.14) leading to the disruption of the boundary layer, greater lateral spreading of the coolant fluid, and smaller vertical extents of the CVP. As can be seen in Figures 8.7-8.10, as the crater depth is increased, the vertical penetration of the CVP is reduced; therefore, with increasing crater depth, the CVP is increasingly located within the low temperature region of the jet and therefore entrains less of the high temperature crossflow gases leading to greater effectiveness.

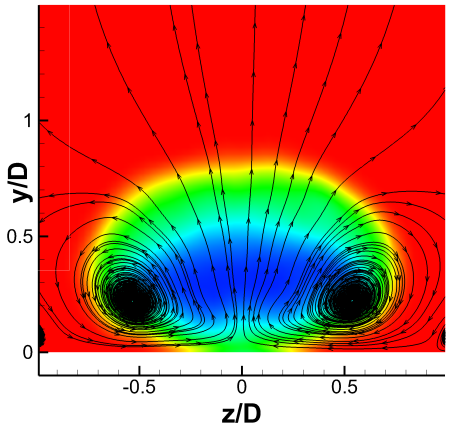


Figure 8.7: Streamlines and temp contours on section $x = 0.5D$ for baseline case

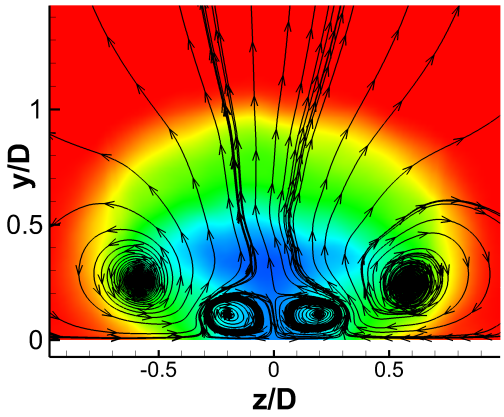


Figure 8.8: Streamlines and temp contours on section $x = 0.5D$ for $0.2D$ crater case

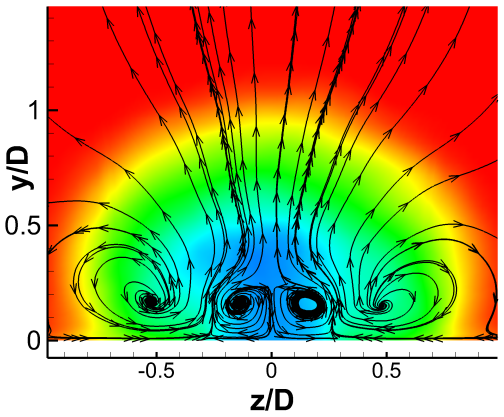


Figure 8.9: Streamlines and temp contours on section $x = 0.5D$ for $0.4D$ crater case

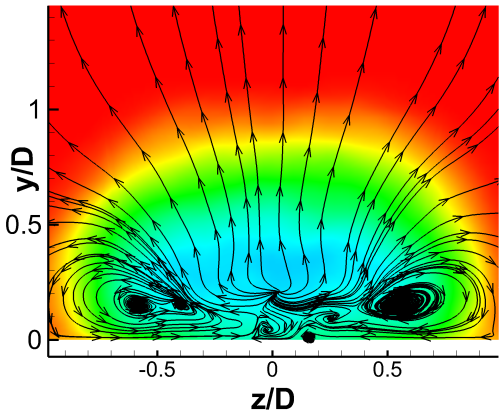


Figure 8.10: Streamlines and temp contours on section $x = 0.5D$ for $0.75D$ crater case

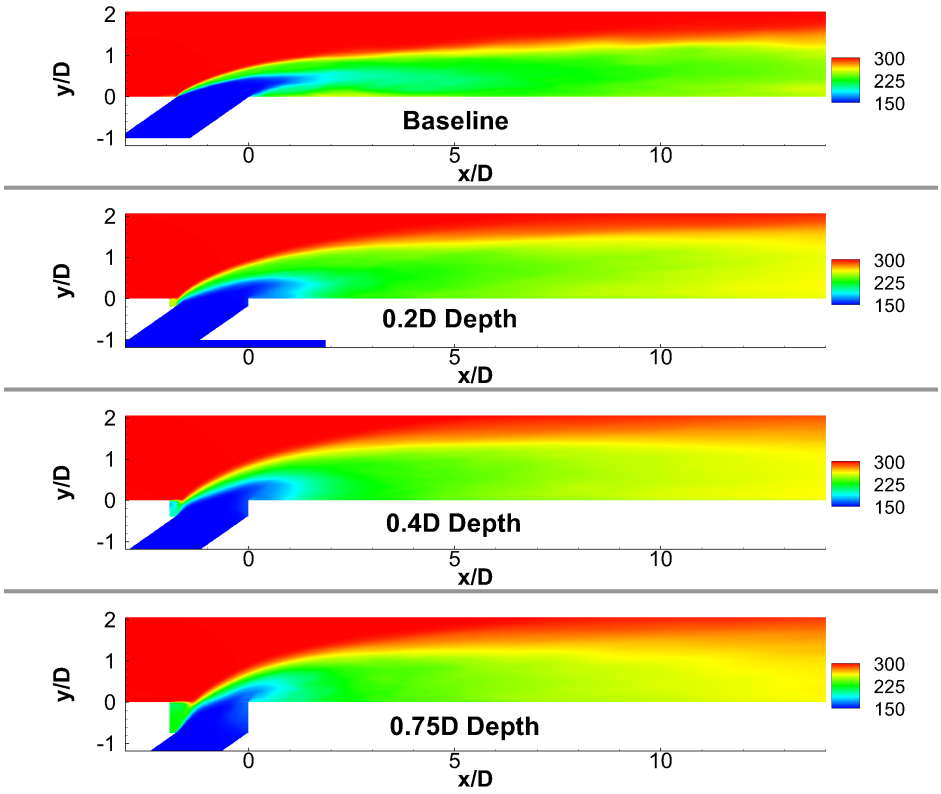


Figure 8.11: Temperature contours on spanwise midsection

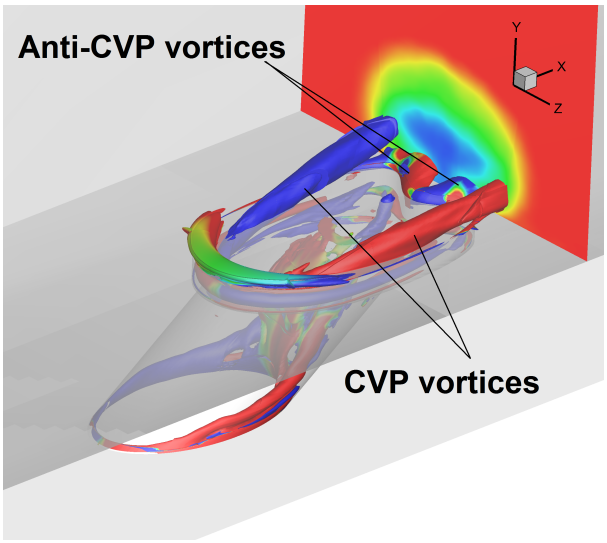


Figure 8.12: Time averaged flow structures $0.2D$ case

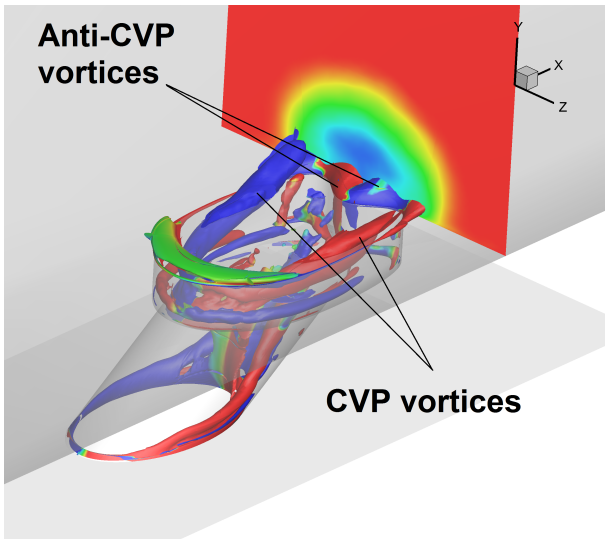


Figure 8.13: Time averaged flow structures $0.4D$ case

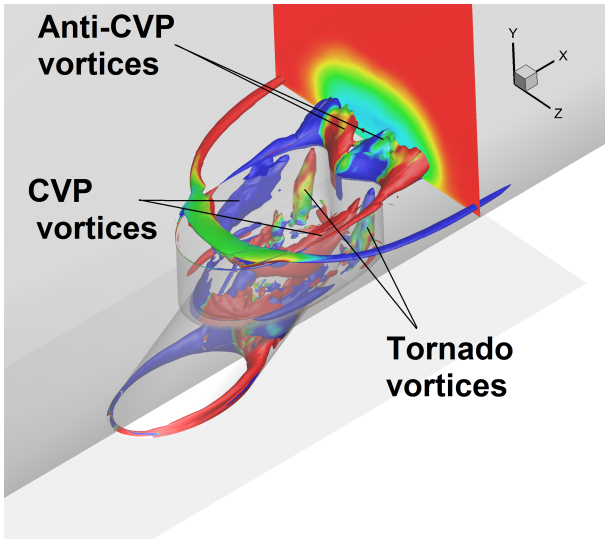


Figure 8.14: Time averaged flow structures $0.75D$ case

### 8.2.3 Tornado vortex pair

The secondary flow generated within the deep crater ($0.75D$ depth) leads to formation of a pair of tornado like vortex structures on either side of the V-protrusion due to lateral deflection of the delivery tube jet as it impacts on the lip of the V-protrusion (shown in Figure 8.15). The temperature contours are shown at the bottom of the crater in Figure 8.15, and at a streamwise section downstream. The streamlines are coloured with the wall-normal

($y$) vorticity component reflecting the vertically-rotating flow structure. The temperature at the base of the tornado vortices is closer to the coolant temperature, and these vortices dispense the coolant towards the lateral boundary of the jet resulting in increased spreading.

The vorticity of tornado structures as it turns in the streamwise direction upon exiting the crater are aligned anti-parallel to the primary CVP. This contributes to weakening the primary CVP reducing vertical penetration (Figure 8.10), while the lateral deflection of the CVP increases the lateral spreading of the coolant (Figure 8.10 and 8.5).

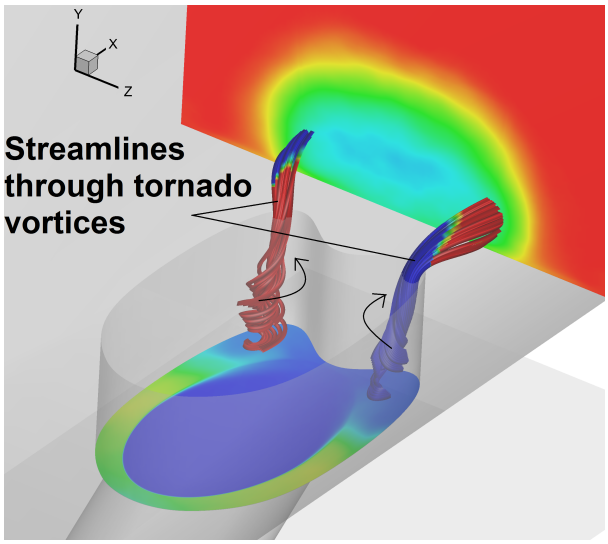


Figure 8.15: Tornado structures $0.75D$ case

## 8.3 Conclusion

A proposed contoured crater design with a V-shaped protrusion is numerically investigated for film cooling performance using large eddy simulation and compared with a baseline no-crater configuration. The validity of the numerical simulations is established through the excellent agreement between the baseline case simulations and the published experimental data. Three crater depths, $0.2D$, $0.4D$ and $0.75D$ are studied. Craters for all the depth under consideration in this paper showed significant improvements in cooling performance. The laterally-averaged cooling performance increased with crater depth with a near-eight fold improvement in the laterally averaged cooling effectiveness immediately downstream of

the hole. Two distinct mechanisms responsible for increase in cooling performance at shallow and deeper depths are identified as: ($i$) formation of anti-CVP pair of vortices below the film cooling jet causing down draft of coolant from jet core and ($ii$) direct impingement of coolant jet on the lip of the V-protrusion leading to secondary flow and tornado vortex that causes significant lateral spreading of coolant fluid for the deeper craters. At intermediate depth $0.4D$ evidence of both aforementioned mechanisms are observed. A comparison with reported best performing crater design for similar conditions show in-excess of 200% increase in the peak performance gain over the respective baseline cases. The gain in cooling effectiveness is the greatest in the near hole region ($x/D < 4$) and diminishes downstream. The corresponding performance gains are even greater when compared to the reported gains for trenched holes.

# Chapter 9
# Conclusion

## 9.1 Conclusions

The flow physics of momentum driven countercurrent shear flow in dump geometry and film cooling flow is investigated using large eddy simulation. The validity of dynamic subgrid scale eddy viscosity model was established through comparison with measurements. Computations of countercurrent shear flows were verified by comparing mean flow and velocity power spectrum with data of Anderson (2011). The predictions of film cooling flows compared satisfactorily with heat transfer and flow statistics measurements of Sinha et al. (1991).

The stability of the counter current shear flows is studied by analysing the time series data set obtained by large eddy simulation using dynamic mode decomposition for three different mass ratios 7.5%, 23% and 36%. Onset of Kelvin-Helmholtz instability at the splitter plate tip is regarded as primary instability mechanism whose time scales remained similar for all parameters mentioned. The origin of primary instability is confirmed though Orr-Sommerfeld analysis of counter shearing velocity profile leading time scales of the most unstable mode similar to the time scales found in simulations. The secondary jet behavior is quantified using spectral content of velocity signal and flow visualization. Large scale flow oscillations developed during the interaction of primary and secondary jet cause significant increase in turbulence in the primary channel for higher mass ratio case. Visualization of coherent flow structures revealed streamwise oriented counter rotating pair of vortices contributing to three dimensionality of the flow. Global instability is established for 36% case

and synchronized flow oscillations are observed throughout the primary channel region. The global mode is realized through the temporal sustenance of the recirculation bubble and found to be the distinction between 23% case where large scale flow oscillations are observed however, no global mode is established. Further, the mechanism of global mode synchronization is studied by analysing spectral information and flow visualization. The effect of discrete secondary jet is proposed and investigated. Substantial effect of secondary jet width on shear layer dynamics is observed. For $8mm$ jet width in excess of 50% turbulence levels were achieved with substantial elimination of secondary jet rollup and related unsteadiness. The entrainment of fluid through the gap between the discrete jets is attributed for alleviating cross stream pressure difference driving secondary jet oscillations.

Secondly, flow physics of film cooling flow is studied in combination of flow visualization and modal analysis. Origin and evolution of shear layer vortices, counter rotating vortex pair (CRVP), hairpin vortices and flow structures within delivery tube and their role in film cooling heat transfer and mixing is studied. The contribution of coherent flow structures to film cooling heat transfer and mixing is quantified using dynamic mode decomposition. CRVP and hairpin modes are found dominant in entrainment of hot gases near wall contributing to 16% fluctuation in adiabatic film cooling effectiveness on cooling wall. Mixing of jet and crossflow fluid is characterized. Jet centerline scalar concentration decay is found to follow $x^{-2/3}$ that is smaller than free jets however, present inclined jet has higher initial entrainment than vertical jets. Maximum scalar dissipation rate is associated with evolution of CRVP and shear layer vortices near film cooling hole.

Thirdly, a new crater design for film cooling application is developed and tested. An anti-kidney pair of vortices developed under the film cooling jet and increased coolant spreading are found to improve the film cooling performance of shallow craters at par with trenches with optimal depth at similar conditions. The film cooling effectiveness surpasses % gain in cooling effectiveness of conventional best performing crater designs by about 200% at similar conditions. The proposed new design may potentially result in longer life/maintenance cycle

for thermal barrier coatings.

# Bibliography


S. Acharya and D. Leedom. Large eddy simulations of discrete hole film cooling with plenum inflow orientation effects. *Journal of Heat Transfer*, 135(1):011010–1, 2013.

M. J. Anderson and P. J. Strykowski. Exploiting global instabilities for efficient flame anchoring and compact combustion. *21st ONR Propulsion Meeting, Monterey, CA*, 2009.

M.J. Anderson. *Global dynamics of a dump combustor using momentum driven countercurrent shear control*. PhD thesis, University of Minnesota, 2011.

J. Andreopoulos and W. Rodi. Experimental investigation of jets in cross-flow. *J. Fluid Mech.*, 138:93–127, 1984.

S. Bagheri. *Analysis and control of transitional shear flows using global modes*. Phd dissertation, 2010.

S. Bagheri, P. Schlatter, P. J. Schmid, and D. S. Henningson. Global stability of a jet in crossflow. *J. Fluid Mech.*, 624:33–44, 2009.

S. Baldauf, M. Scheurlen, A. Schulz, and S. Witting. Correlation of film-cooling effectiveness from thermographic measurements at enginelike conditions. *Journal of Turbomachinery*, 124:686–698, 2002.

G. Berkooz, P. Holmes, and J. L. Lumley. The proper orthogonal decomposition in the analysis of turbulent flows. *Annu. Rev. Fluid Mech.*, 25:539–537, 1993.

L. P. Bernal and A. Roshko. Streamwise zvortex structures in plane mixing layers. *Journal of Fluid Mechanics*, 170:499–525, 1986.

C.H. Bosanquet and J.L. Pearson. The spread of smoke and gases from chimneys. *Trans. Faraday Soc.*, 32:1249–1263, 1936.

P. Bradshaw. The effect of initial conditions on the development of a free shear layer. *Journal of Fluid Mechanics*, 26-02:225–236, 1966.

A. Bradstater and L. H. Swinney. Strange attractors in weakly turbulent couette-taylor flow. *Physical Review*, 35-5:2207–2220, 1987.

L. Brown, G. and A. Roshko. On density effects and large structure in turbulent mixing layers. *Journal of Fluid Mechanics*, 64:775–816, 1974.

R. Bunker. Film cooling effectiveness due to discrete holes within a transverse surface slot. *Paper No. GT-2002-30178, IGTI Turbo Expo, Amsterdam, Netherlands*, 2002.

R. S. Bunker. A method for improving the cooling effecgtiveness of gaseous coolant stream. *US Patent No. 6,234,755*, 2001.

Ron Bunker. A review of turbine shaped film cooling technology. *Journal of Heat Transfer*, 127:441–453, 2005.

K. K. Chen, H. Tu. Jonathan, and C. W. Rowley. Varients of dynamic mode decomposition: boundary conditions, koopman, and fourier analyses. *Journal of Nonlinear Science*, 22(6): 887–915, 2012.

P.H. Chen, D. Ai, and S. H. Lee. Effects of compound angle injection on flat plate film cooling through a row of conical holes. *ASME Paper 98-GT-429*, 1998.

SLV. Coelho and JCR. Hunt. The dynamics of the near field of strong jets in cross-flow. *J. Fluid Mech.*, 200:95–120, 1989.

S. Corrsin. Investigations of flow in an axially symmetric heated jet of air. *NACA Adv. Conf. Rep.3123*, 1943.

L. Cortelezzi and A.R. Karagozian. On the evolution of vorticity in pulsating jets in crossflow. *Bulletin of the Amer. Phys. Soc.*, 44(8), 1999.

F. T. Davidson, Kistenmacher D. A., and D. G. Bogard. Film cooling with a thermal barrier coating: Round holes, craters and trenches. *Proceedings of ASME Turbo Expo 2012-GT2012*, 2012.

J. Davitian, D. Getsinger, C. Hendrickson, and A. R. Karagozian. Transition to global instability in transverse-jet shear layers." j. fluid mech 661: 294-315. *Journal of Fluid Mechanics*, 661:294–315, 2010.

J. R. Dorrington, D.G. Bogard, and R.S. Bunker. Film effectiveness performance for coolant holes embedded in various shallow trench and crater depressions. *IGTI Turbo Expo, Montreal, Canada*, Paper No. GT-2007:749–758, 2007.

P. G. Drazin and Reid W. H. Hydrodynamic instability. *Cambridge University Press*, 1981.

J.R. Edwards. A low-diffusion flux splitting scheme for navier-stokes calculations. *Computers and Fluids*, 26:635–659, 1997.

W. S. Edwards, L. S. Tuckerman, R. A. Friesner, and D.C. Sorensen. Kreylov methods for the incompressible navier-stokes equations." j. comput. phys. 110: 82-102. *Journal of Computational Physics*, 110-1:82–102, 1994.

D. J. Forliti and P.J. Strykowski. Controlling turbulence in a rearward-facing step combustor using countercurrent shear. *Journal of Fluids Engineering*, 127:438–448, 2005.

D. J. Forliti, B. A. Tang, and P. Strykowski. An experimental investigation of planar countercurrent turbulent shear layers. *Journal of Fluid Mechanics*, 530:241–264, 2005.

T. F. Fric and A. Roshko. Vortical structure in the wake of a transverse jet. *J. Fluid Mech.*, 279:1–47, 1994.

T.F. Fric and R.P. Campbell. Method for improving the cooling effectiveness of a gaseous coolant stream which flows through a substrate, and related articles of manufacture. *U.S. patent No. 6,383,602*, 2002.

M. Germano, U. Piomelli, P. Moin, and W.H. Cabot. A dynamic subgrid scale eddy viscosity model. *Physics of Fluids*, 3:1760–1765, 1991.

S. S. Girimaji and Y. Zhou. Analysis and modeling of subgrid scale scalar mixing using numerical data. *Physics of Fluids*, 8:1224–1236, 1996.

R. J. Goldstein. Film cooling. *Advances in heat Transfer*, 7:321–379, 1971.

R. J. Goldstein, E.R.G. Eckert, V. L. Eriksen, and J. W. Ramsey. Film cooling following injection through inclined circular tubes. *Israel Journal of Technology*, 8:145–154, 1970.

R. J. Goldstein, E.R.G. Eckert, and E. Burgraf. Effects of hole geometry and density on three dimensional film cooling. *International Journal of Heat and Mass Transfer*, 17:595–605, 1974.

M. Gritsch, A. Schulz, and S. Wittig. Heat transfer coefficient measurements of film cooling holes with expanded exits. *ASME Paper 98-GT-28*, 1998a.

M. Gritsch, A. Schulz, and S. Wittig. Adiabatic wall effectiveness measurements of film cooling holes with expanded exits,. *ASME Journal of Turbomachinery*, 120:549–556, 1998b.

W. Gropp and E. Lusk. Using mpi: Portable parallel programming with the messsage-passing interface. *The MIT Press*, 1999.

D. A. Hammond and L. G. Redekopp. Local and global instability properties of seperation bubbles. *Euro. J. Mech. B./Fluids*, 17 No.2:145–164, 1998.

B. A. Haven, D. K. Yamagata, M. Kurosaka, S. Yamawaki, and T. Maya. Anti-kidney pair of vortices in shaped holes and their influence on film cooling effectiveness. *IGTI Turbo Expo, Orlando, Paper GT-1997-45*, pages 441–453, 1997.

K. Haven and M. Kurosaka. Kidney and anti-kidney vortices in crossflow jets. *J. Fluid Mech.*, 352:27–64, 1997.

J. D. Heidmann and S. V. Ekkad. A novel anti-vortex turbine film cooling hole concept. *Journal of Turbomachinery*, 130:031020–1–9, 2008.

C. M. Ho and P. Huerre. Perturbed free shear layers. *Annu. Rev. Fluid Mech.*, 16:365–424, 1984.

P. Huerre and P. A. Monkewitz. Absolute and convective instabilities in free shear layers. *Journal of Fluid Mechanics*, 159:151–168, 1985.

P. Huerre and P. A. Monkewitz. Local and global instabilities in spatially develped flows. *Annu. Rev. Fluid Mech.*, 22:473–537, 1990.

A. C. Humphrey, J. and S. Li. Tilting, stretching. pairing and collapse of vortex structures in confined counter-current flow. *Journal of Fluids Engineering*, 103:466–470, 1981.

M. Ilak and C. Rowley. Modeling of transitional channel flow using balanced proper orthogonal decomposition. *Physcs of Fluids*, 20(3):034103, 2008.

Milos Ilak, Philipp Schlatter, Shervin Bagheri, and Dan S. Henningson. Bifurcation and stability analysis of a jet in cross-flow:onset of global instability at a low velocity ratio. *J. Fluid Mech.*, 696:94–121, 2012.

I. V. Iourokina and S. K. Lele. Towards large eddy simulation of film cooling flows on model turbine blade leading edge, 2005.

I. V. Iourokina and S. K. Lele. Large eddy simulation of film cooling flow above a flat plate from inclined cylindrical holes. ASME Paper No. FEDSM2006-98282, 2006a.

I. V. Iourokina and S. K. Lele. Large eddy simulation of film-cooling above the flat surface with a large plenum and short exit holes. In *44th Aerospace Sciences Meeting and Exhibit, Reno, NV,*, volume AIAA Paper No. 2006-1102, 2006b.

J. Jeong and F. Hussain. On identification of a vortex. *J. Fluid Mech.*, 285:69–94, 1995.

J. Jimenez. A spanwise structures in the plane shear layer. *Journal of Fluid Mechanics*, 132: 319–336, 1983.

S. Jordan. Dynamic subgrid-scale modeling for large-eddy simulations in complex topologies. *Journal of Fluids Engineering*, 123:619–627, 2001.

S. Jovic and D. Driver. Backward-facing step measurement at low reynolds number, reh=5000. *NASA Technical Memorandum 108807*.

In Sung Jung and Joon Sik Lee. Effects of orientation angles on film cooling over a flat plate: Boundary layer temperature distributions and adiabatic film cooling effectiveness. *Journal of Turbomachinery*, 122:153–160, 2000.

P. Kalghatgi and S. Acharya. Modal analysis of inclined jet film cooling flows with density variation. In *Proceedings of the 2013 ASME Summer Heat Transfer Conference*, 2013.

G. Karypis and V. Kumar. Metis, a software package for partitioning unstructured graphs, partitioning meshes, and computing fill-reducing ordering of sparse matrices. *University of Minnesota*, 1998.

R. M. Kelso and A.J. Smits. Horseshoe vortex systems resulting from the interaction between laminar boundary layer and a transverse jet. *Physics of Fluids*, 7(1):153–158, 1995.

R. M. Kelso, T. T. Lim, and A. E. Perry. An experimental study of round jets in cross-flow. *J. Fluid Mech.*, 306:111–144, 1996.

A. S. Khemakhem. *An experimental study of turbulent countercurrent shear layers.* PhD thesis, University of Minnesota - Twin Cities, Minneapolis, MN, 1997.

Sun-Min Kim, Ki-Don Lee, and Kwang-Yong Kim. A comparative analysis of various shaped film-cooling holes. *Heat Mass Transfer. DOI 10.1007/s00231-012-1043-5*, 2012.

A. Krothapalli, L. Lourenco, and JM. Buchlin. Separated flow upstream of a jet in cross-flow. *AIAA Journal*, 28:414–420, 1990.

J. C. Lasheras and H. Choi. Three-dimansional instability of a plane free shear layer: an experimental study of the formation and evolution of streamwise vortices. *Journal of Fluid Mechanics*, 189:53–86, 1988.

H. Le, P. Moin, and J. Kim. Direct nuymerical simulation of turbulent flow over a backward-facing step. *J. Fluid Mech.*, 330:349–374, 1997.

S. W. Lee, Y. B. Kim, and J. S. Lee. Flow characteristics and aerodynamic losses of film-cooling jets with compound angle orientations. *Journal of Turbomachinery*, 119:310319, 1997.

A. Leonard. Energy cascade in large eddy simulations of turbulent folow. *Adv. Geophys*, 18A:237–248, 1974.

H. W. Liepmann and J. Laufer. Investigations of free turbulent mixing. *NACA tech. Note 1257. Natl. Advis. Comm. Aeronaut. Washington, DC.*, 1947.

P. M. Ligrani, S. Ciriello, and D. T. Bishop. Heat transfer, adiabatic effectiveness, and injectant distributions downstream of a single row and two staggered rows of compound angle film-cooling holes. *Journal of Turbomachinery*, 114:687700, 1992.

T.T. Lim, H. T. New, and S. C. Luo. On the development of large-scale structures of jet normal to cross flow. *Physics of Fluids*, 13(3):770–775, 2001.

J.S. Liu, M.F. Malak, L.A. Tapia, D. C. Crites, D. Ramachandran, B. Srinivasan, and J. Venkataraman. Enhanced film cooling effectiveness with new shaped holes. *IGTI Turbo Expo,Glasgow, Paper GT-2010-22774*, 2010.

Y. Lu. *Effect of hole configurations on film cooling on cylindrical inclined holes for the application to gas turbine blades.* PhD thesis, Louisiana State University, 2007.

J. L. Lumley. *Stochastic tools in turbulence.* Academic Press, 1970.

R. J. Margason. Fifty years of jet in crossflow research. In *Proceedings of the AGARD symposium on computational and experimental assessment of jets in crossflow. AGARD-CP-534*, 1993.

A. B. Mehendale and J. C. Han. Influence of high mainstream turbulence on leading edge film cooling heat transfer. *Journal of Turbomachinery*, 114:707–715, 1992.

K. E. Meyer, J. M. Pedersen, and O. Ozcan. A turbulent jet in crossflow analysed with proper orthogonal decomposition. *J. Fluid Mech.*, 583:199–227, 2007.

I. Mezic. Spectral properties of dynamical systems, model reduction and decompositions. *Nonlinear Dynamics*, 41(1-3):309–325, 2005.

P. Moin and C. C. Pierce. Large eddy simulation of a coaxial jet combustor. Technical report, AFOSR F49620-95-1-0185 Final Report, 1999.

P. Moin, K. Squires, W. Cabot, and S. Lee. A dynamic subgridscale model for compressible turbulence and scalar transport. *Physics of Fluids*, A3:2746–2757, 1991.

P. A. Monkewitz, D. W. Bechert, B. Barsikow, and B. Lehmann. Self-ecited oscillations and mixing in a heated round jet. *Journal of Fluid Mechanics*, 213:611–639, 1990.

S. Muppidi and K. Mahesh. Passive scalar mixing in jets in crossflow. In *44th AIAA Aerospace Sciences Meeting and Exhibit*, Reno, Nevada, 2006.

S. Muppidi and K. Mahesh. Direct numerical simulation of passive scalar transport in transverse jets. *Journal of Fluid Mechanics*, 598:335–360, 2008.

Hasan Nasir, Sumanta Acharya, and Srinath Ekkad. Improved film cooling from cylindrical angled holes with triangular tabs: effect of tab orientations. *International Journal of Heat and Fluid Flow*, 24(5):657–668, 2003.

B.R. Noack, M. Schlegel, M. Ahlborn, B. Mutschke, M. Morzynski, P. Comte, and G. Tadmor. A finite-time thermodynamics formalism for unsteady flows. *J. Non-Equilib. Thermodyn*, 33:103–148, 2008.

D. R. Pedersen, E.R.G. Eckert, and Goldstein R.J. Film cooling with large density differences between the mainstream and the secondary fluid measured by heat transfer analogy. *ASME Journal of Heat Transfer*, 99:620–627, 1977.

Y. V. Pete and S. K. Lele. Near field of film cooling jet issued into a flate plate boundary layer: Les study, 2008.

U. Piomelli, A. Scotti, and E. Balaras. Large-eddy simulations of turbulent flows, from desktop to supercomputer.

l. Prandtl. Z. angew. *Math. Mech.*, 8:249–251, 1928.

P. Renze, M. Meinke, and W. Schroder. Les of turbulent mixing in film cooling flows. *Conference on Turbulence and Interactions TI2006m May29-June2, Porquerolles, France*, 2006.

P. Renze, W. Schroder, and M. Meinke. Large eddy simulation of film cooling flows with variable density jets. *Flow, Turb, Comb.*, 80(1):119–132, 2008a.

P. Renze, W. Schroder, and M. Meinke. Large-eddy simulation of film cooling flows at density gradients. *International Journal of Heat and Fluid Flow*, 29:18–34, 2008b.

A. Rozati and D. K. Tafti. Effect of coolant-mainstream blowing rati on leading edge film cooling flow and heat transfer - les investigation. *International Journal of Heat and Fluid Flow*, 29:857–873, 2008a.

A. Rozati and D. K. Tafti. Large eddy simulation of leading edge film cooling-part-ii: Heat transfer and effect of blowing ratio. *ASME J. Turbomachinery*, 130:041015, 2008b.

D. Ruelle and F. Takens. On the nature of turbulence. *Comm. Math. Phys.*, 20:167–192, 1971.

P. Sagaut. *Larger Eddy Simulation for Incompressible Flows.* Springer, Berlin, Germany, 2001.

J. E. Sargison, S. M. Guo, M. L. G. Oldfield, G. D. Lock, and A. J. Rawlinson. A converging slot-hole film-cooling geometrypart 1: Low-speed flat-plate heat transfer and loss. *ASME Journal of Turbomachinery*, 124:453–460, 2002.

R. Sau and K. Mahesh. Dynamics and mixing of vortex rings in crossflow. *J. Fluid Mech.*, 604:389–409, 2008.

C. Saumweber, A. Schulz, and S. Wittig. Free-stream turbulence effects on film cooling with shaped holes. *IGTI Turbo Expo, Amsterdam, Paper GT-2002-30170*, 2002.

P.J. Schmid and J.L. Sesterhenn. Decomposition mode decomposition of numerical and experimental data. In *Bull. Amer. Phys. Soc.*, 2009.

D. L. Schmidt, B. Sen, and D. G. Bogard. Film cooling with compound angle holes: Adiabatic effectiveness. *Journal of Turbomachinery*, 118:807–813, 1996.

P. J. Schmidt. Dynamic mode decomposition of numerical and experimental data. *J. Fluid Mech.*, 656:5–28, 2010.

R. S. Scorer. *Natural Aerodynamics*. Pergamon, 1958.

A. Seena and H.J. Sung. Dynamic mode decomposition of turbulent cavity flows for self-sustained oscillations. *International Journal of Heat and Fluid Flow*, 32(6):1098–1110, 2011.

J.W. Shan and P.E. Dimotakis. Reynolds-number effects and anisotropy in transverse-jet mixing. *J. Fluid Mech.*, 566:47–96, 2006.

A. K. Sinha, D.G. Bogard, and M. E. Crawford. Film-cooling effectiveness downstream of a single row of holes with variable density ratio. *Journal of Turbomachinery*, 113:442–449, 1991.

S.H. Smith and M.G. Mungal. Mixing, structures and scaling of the jet in crossflow. *J. Fluid Mech.*, 357, 1998.

P. Strykowski and D. L. Niccum. The influence of velocity and density ratio on the dynamics of spatially developing mixing layers. *Physics of Fluids*, A4:770–781, 1992.

P. Strykowski, A. Krothapalli, and D. Wishart. The enhancement of mixing in high speed heated jets using a coucounterflow nozzle. *AIAA Journal*, 31:2033–2038, 1993.

P. J. Strykowski and D. J. Forliti. Flow control applications using countercurrent shear. international symposium on recent advances in experimental fluid mechanics. *Indian Institute of Technology, Kanpur, India*, 2000.

P. J. Strykowski and D. L. Niccum. The stability of countercurrent mixing layers in circular jets. *Journal of Fluid Mechanics*, 227:309–343, 1991.

P. J. Strykowski and R. K. Wilcoxon. Mixing enhancement due to global oscillations in jets with annular counterflow. *AIAA Journal*, 31(3):564–570, 1993.

A. Suslov S. Numerical aspects of searching convective/absolute instability transition. *Journal of Computational Physics*, 212:188–217, 2006.

O. G. Sutton. A theory of eddy diffusion in the atmosphere. *Proc. R. Soc.*, A 135:143–65, 1932.

R. I. Sykes, W. S. Lewellen, and S. F Parker. On the vorticity dynamics of a turbulent jet in a crossflow. *J. Fluid Mech.*, 168:393–413, 1986.

D. K. Tafti. Evaluating the role of subgrid stress modeling in a ribbed duct for the internal cooling of turbine blades. *International Journal of Heat and Fluid Flow*, 26:92–104, 2005.

H. Tennekes and J. L. Lumley. A first course in turbulence. *MIT Press*, 1983.

K. Thole, M. Gritsch, A. Schulz, and S. Witting. Flow field measurements for film cooling holes with expanded exits. *ASME Journal of Turbomachinery*, 120:327–336, 1998.

A. A. Townsend. Measurements in the turbulent wake of a cylinder. *Proc. R. Soc. London Ser.*, A 190:551–561, 1947.

M. Tyagi and S. Acharya. Large eddy simulation of film cooling flow from and inclined cylindrical jet. *ASME Journal of Turbomachinery*, 125:734–742, 2003.

M. Tyagi and S. Acharya. Large eddy simulation in complex geometries using the immersed boundary method. *Intl. J. of Numerical Methods in Fluids*, Vol.48:691–722, 2005.

S.K. Waye and D.G. Bogard. High resolution film cooling effectiveness measurements of axial holes embedded in transverse trench with various trench configurations. *ASME Journal ofTurbomachinery*, 129:294–302, 2007.

J.M. Weiss and W.A. Smith. Preconditioning applied to variable and constant density flows. *AIAA Journal*, 33:2050–2057, 1995.

C. D. Winant and F. K. Browand. Vortex pairing: the mechanism of turbulent mixing-layer growth at moderate rreynolds number. *Journal of Fluid Mechanics*, 63-02:237–255, 1974.

J. Wu, H. Ma, and M. Zhou. *Vorticity and Vortex Dynamics*. Springer, 2006.

X. Xie, M. Weiwei, and H. Zhou. Coherent structures in countercurrent axisymmetric shear flows. *Acta Mechanica Sinica(English Series)*, 19:11–32, 2003.

Cheng-Feng Yang and Jing-Zhou Zhang. Experimental investigation on film cooling characteristics from a row of holes with ridge-shaped tabs. *Experimental Thermal and Fluid Science*, 37:113–120, 2012.

L. L. Yuan, R. L. Street, and J. H. Ferziger. Large-eddy simulations of a round jet in crossflow. *J. Fluid Mech.*, 379:71–104, 1999.

L.L. Yuan and R. L. Street. Trajectory and entrainment of a round jet in crossflow. *Physics of Fluids*, 10:2323–2335, 1998.

N.M. Yusop, A.H. Ali, and M.Z. Abdullah. Computational study of a new scheme for a film-cooling hole on convex surface of turbine blades. *International Communications in Heat and Mass Transfer*, 43:90–99, 2013.

# Appendix: Dynamic Mode Decomposition

Nonlinearity and high dimensionality of complex dynamical operators such as the one encountered in turbulent flows pose significant challenge in the analysis. Snapshot based modal decomposition techniques provide a realistic method to represent an high dimensional dynamical operator with a low dimensional approximation. The deduction of the modes constituting the low dimensional representation is such that they represent the dynamically significant coherent structures of the underlying flow field.

One such method is proper orthogonal decomposition (POD) (Berkooz et al., 1993). POD captures spatially orthogonal modes that captures the energy of the underlying flow field optimally. The method is based on diagonalization of spatial correlation matrix generated by a time sequence of instantaneous snapshots of evolving flow field and used for reduced order modeling of complex flow fields to obtain reduced order dynamics, through Galerkin projection. Although POD is method of choice due to optimality in energy capture and orthogonality of captured modes it fails to capture low energy dynamically significant modes (Noack et al., 2008). This fact is emphasized in the difficulty of using POD modes as a basis of reduced order model (Ilak and Rowley, 2008).

Dynamic mode decomposition (DMD), an alternative decomposition method, was first developed by Schmid and Sesterhenn (2009); Schmidt (2010). Similar to POD, DMD also utilizes the empirical data obtained from simulations or experiments. However, unlike POD, DMD approximately captures the modes of Koopman operator which is linearization of nonlinear dynamical operator governing the spatio-temporal evolution of dynamical system

$$y_{n+1} = f(y_n) \tag{1}$$

The Koopman operator $U$ is defined as,

$$Ug(y) = g(f(y)) \tag{2}$$

The generalized eigen decomposition in case of a simplified equation $\dot{y} = \lambda y$ and $g(y) = y$ (a specific observable from the state space of dynamical system defined by equation 1),

$$U_t g(y) = e^{\lambda t} y \tag{3}$$

In case of a generic flow field $\phi(y, t)$ the localized linear behavior of a nonlinear system in terms of Koopman operator may be further written as,

$$U_t \phi(y_0) = e^{\lambda t} \phi(y_0) \tag{4}$$

where eigen function of Koopman operator $U_t$ are given by a function set $\phi$ and $\lambda$ are corresponding eigen values. For a generalized system $\dot{y} = Ay$ the associated Koopman eigen functions written as,

$$g(y) = \sum_{i=1}^{N} \phi_i(y) v_i \tag{5}$$

where $v_i$ are eigen vectors of A and Koopman operator becomes,

$$y(t) = U_t g(y_0) = \sum_{i=1}^{N} e^{\lambda_i t} \phi_i(y_0) v_i \tag{6}$$

where $y_0$ is the initial condition or a state of a system ar arbitrary time.

For a generic nonlinear process, the spectral decomposition (FollowingMezic (2005)) of

the Koopman operator yields,

$$Ug(y, \hat{x}) = U_p g(y, \hat{x}) + U_c g(y, \hat{x}) \tag{7}$$

where $U_p$ is the periodic part with discrete frequency and $U_c$ is chaotic part with continuous spectrum. The corresponding velocity field follows triple decomposition following spectral decomposition of Koopman operator,

$$u(y, \hat{x}, t) = u^*(y, \hat{x}) + u_p(y, \hat{x}, t) + u_c(y, \hat{x}, t) \tag{8}$$

where, $u^*(y, \hat{x})$ is time averaged field, $u_p$ is periodic and $u_c$ is aperiodic part. $\hat{x}$ is the spatial location in the flow field and $y$ is a specific state space. For a quasi periodic field similar to attractors,

$$u(y, \hat{x}, t) = u^*(y, \hat{x}) + u_p(y, \hat{x}, t) \tag{9}$$

where $u_p$ is given by expression similar to 6 .

**Estimation of Koopman modes - DMD**

Dynamic mode decomposition assumes a linear mapping operator $A$ for the flow field such that,

$$v_{i+1} = Av_i \tag{10}$$

where, $v_i$s are the instantaneous snapshots of the flow field and linear mapping operator $A$ is synonymous to equation 1. A sequence of N snapshots of flow field are collected with time interval $\Delta t$ and arranged in matrix form $V_1^N$,

$$V_1^N = \{v_1, v_2, ..., v_N\} \tag{11}$$

Assuming the validity linear mapping operator over total sampling time $N * \Delta t$, the sequence of snapshots may be expressed in terms of initial snapshot $i = 1$,

$$V_1^N = \{v_1, Av_1, A^2v_1, ..., A^Nv_1\} \tag{12}$$

Such a linear map $A$ governs the dynamical process embedded in the sequence of snapshots therefore, the eigenvalues and eigenvectors of linear map $A$ describe its dynamical characteristics. Owing to the underlying assumption of periodicity of the dynamical process, beyond sufficiently large $N$, the snapshots become linearly dependent. Therefore, for sufficiently large $N$ $n^{th}$ snapshot may be expressed as linear combination of previous $N-1$ snapshots,

$$v_N = c_1v_1 + \ + c_{N-1}v_{N-1} + r \tag{13}$$

Following the analogy,

$$AV_1^{N-1} = \{Av_1, A^2v_1, , A^{N-1}v_1\} = V_2^N \tag{14}$$

Since $V_1^{N-1}$ and $V_2^N$ differ by only $N^{\text{th}}$ snapshot, writing Eq. 14 in the following form,

$$V_2^N = AV_1^{N-1} = V_1^{N-1}C + I_r \tag{15}$$

leads to companion matrix $C$ with coefficient of linear combination $c_i$,

$$C = \begin{bmatrix} 0 & & \dots & 0 & c_1 \\ 1 & \ddots & & \vdots & c_2 \\ 0 & \ddots & \ddots & & \vdots \\ \vdots & & 1 & 0 & c_{N-2} \\ 0 & \dots & 0 & 1 & c_{N-1} \end{bmatrix} \tag{16}$$

The eigenvalue (Ritz values $\mu$) and eigenvectors (Ritz vectors $Y$) of $C$ can be directly evaluated to estimate the eigenvalues and eigenvectors of $A$. Estimation of Koopman modes (referred as dynamic modes in the context of present algorithm due to Schmidt (2010)) is given by projecting the data sequence onto the eigenvectors of $C$

$$\Phi = V_1^{N-1} Y \tag{17}$$

where $Y$ is eigenvector matrix of $C$. The amplitude of the $i^{th}$ mode given as, by the second norm $||\Phi_i||$, represents the energy content of the specific mode. The Ritz values $\mu$ are logarithmically mapped, $\lambda = log(\mu)/\Delta t$. The real part $\lambda_r$ represents the growth rate and imaginary $\lambda_i$ angular frequency of the corresponding modes. Thus, DMD modes may be ranked based on the growth rate (dynamic significance), energy ranking and frequency contents. Additionally, the energy ranking may be evaluated based on a selected region of interest to identify the local role/influence of various DMD modes.

**Reduced order representation and time stepping**

Instantaneous flow field at an arbitrary instant of time $t$ in terms for modal decomposition using dynamic modes can be written as,

$$u(\mathbf{x}, t) = \sum_{i=1}^{N} e^{(\lambda_i t)} \Phi_i(\mathbf{x}) \tag{18}$$

where $\lambda_i$ is logarithmically mapped Ritz value $\lambda = log(\mu)/\Delta t$. $N$ is total number of extracted modes and $\Phi_i$s are the dynamic modes.Equation 18 can be re-written as,

$$u(\mathbf{x}, t) = \sum_{i=1}^{N} \mu_i^{(t/\Delta t)} \Phi_i(\mathbf{x}) \tag{19}$$

Using an appropriate ranking criterion, the instantaneous flow field may be reconstructed using only a selected modes to obtain a criterion specific low-dimensional representation of the

instantaneous flow field. Since expression 18 is continuous in time there, the reconstructed flow field can be advanced for the $t > N\Delta t$ or flow field may be sampled with a lower time step $\Delta t$. Thus a time stepper is inherent to dynamic mode decomposition. However, over sampling of the flow field do not produce additional dynamic information that is not already captured in dynamic modes $\Phi_i$s.

# Vita

Prasad M. Kalghatgi was born in the city of Sangli, India, in 1981. He finished his undergraduate studies at Visvesvaraiah Technological University in Mechanical Engineering in May 2003. He worked as Research Engineer (CFD) at Fluidyn Software and Consultancy Pvt. Ltd. Bangalore, India until July 2006. In August 2006 he came to Louisiana State University to pursue graduate studies in Mechanical Engineering. He is currently a candidate for the degree of Doctor of Philosophy in Mechanical Engineering, which will be awarded in December 2013.